Stretcher and Amplifier Design for the LPA Drive Lasers ANGUS and KALDERA

by

Cora Sophia Lara Braun

A Thesis Submitted to the Faculty of

Mathematics, Informatics and Natural Sciences

Department of Physics

for the Degree of

DOCTOR RERUM NATURALIUM

Universität Hamburg

December 2024

Gutachter der Dissertation:	Dr. Andreas R. Maier
	Prof. Dr. Franz X. Kärtner
Zusammensetzung der Prüfungskommission:	Dr. Andreas R. Maier
	Prof. Dr. Franz X. Kärtner
	Prof. Dr. Daniela Pfannkuche
	Prof. Dr. Wim Leemans
	Prof. Dr. Michael Potthoff
Vorsitzende der Prüfungskommission:	Prof. Daniela Pfannkuche
Datum der Disputation:	05.03.2025
Vorsitzender des Fach-Promotionsausschusses Physik:	Prof. Dr. Wolfgang J. Parak
Leiter des Fachbereichs Physik:	Prof. Dr. Markus Drescher
Dekan der Fakultät MIN:	Prof. Dr.-Ing Norbert Ritter

Eidesstattliche Versicherung / Declaration on oath

Hiermit versichere ich an Eides statt, die vorliegende Dissertationsschrift selbst verfasst und keine anderen als die angegebenen Hilfsmittel und Quellen benutzt zu haben.

Sofern im Zuge der Erstellung der vorliegenden Dissertationsschrift generative Künstliche Intelligenz (gKI) basierte elektronische Hilfsmittel verwendet wurden, versichere ich, dass meine eigene Leistung im Vordergrund stand und dass eine vollständige Dokumentation aller verwendeten Hilfsmittel gemäß der Guten wissenschaftlichen Praxis vorliegt. Ich trage die Verantwortung für eventuell durch die gKI generierte fehlerhafte oder verzerrte Inhalte, fehlerhafte Referenzen, Verstöße gegen das Datenschutz- und Urheberrecht oder Plagiate.

Ich versichere, dass dieses gebundene Expemplar der Dissertation und das in elektronischer Form eingereichte Dissertationsexemplar (über den Docata-Upload) und das bei der Fakultät (Promotionsbüro Physik) zur Archivierung eingereichte gedruckte gebundene Exemplar der Dissertationschrift identisch sind.

Die Dissertation wurde in der vorgelegten oder einer ähnlichen Form nicht schon einmal in einem früheren Promotionsverfahren angenommen oder als ungenügend beurteilt.

Hamburg, den 20.12.2024 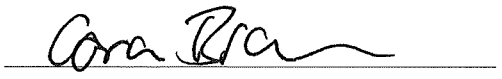

Cora Braun

Abstract

Laser-plasma accelerators (LPAs) are a promising technology to build compact and cost-efficient accelerators for a variety of applications. To realize this promise, the reliability and long-term stability of the accelerated electrons have to be improved. Much of this improvement relates to the stability of the drive laser. Apart from improving passive stability, increasing the repetition rate of the laser from a few Hz to >100 Hz, enables the use of active stabilizations, that can account for many lower frequency contributions from e.g. mechanical vibrations and air-fluctuations. The overarching goal of the thesis is to develop setups for the Ti:Sa CPA TW-class laser systems ANGUS and KALDERA, that allow for a stable laser performance and acceleration of high-quality electrons.

To improve the long-term stability of the ANGUS laser, a new, more stable front-end, based on optical-parametric chirped-pulse amplification (OPCPA) was built. This thesis reports on the design, alignment and characterization of the stretcher, that was required to integrate the OPCPA front-end into the laser system. The design goal was to achieve a stable and tunable stretcher and to minimize the angular chirp of the output beam by alignment with a three-color-laser. The characterization of the stretcher and its implementation into the laser system, which led to the compression of pulses to 31 fs with sub-percent pulse duration stability will be presented.

With KALDERA a >100Hz repetition rate LPA drive laser is currently being developed on DESY campus. To withstand the >100 W average power in the final pulse compressor, multi-layer dielectric (MLD) gratings need to be used. This thesis reports on the development, setup and characterization of a two-transmission grating, two-pass Oeffner stretcher, that matches such a MLD compressor. Using this stretcher, compression to sub-30 fs pulse lengths at Ti:Sa wavelength in an out-of-plane compressor with MLD gratings could be demonstrated for the first time. The characterization of the output pulses showed the viability of the stretcher and compressor concept for the KALDERA laser and other future high-average power, TW, fs laser systems.

To efficiently seed the final amplifiers, a Booster amplifier is required for the KALDERA laser. The designed three-pass Ti:Sa amplifier provides 0.5-1 mJ output energy and sub-percent energy stability. The stretcher and the Booster amplifier successfully seed the KALDERA multi-pass amplifiers to saturation, enabling sub-0.5 % energy stability in the final amplifier stage.

Zusammenfassung

Laser-Plasma Beschleunigung (LPA) ist eine vielversprechende Technologie, um zukünftig kompaktere und kosteneffizientere Beschleuniger für eine Vielzahl an Anwendungen zu bauen. Um diese Vision umzusetzen, ist eine Verbesserung der Langzeitstabilität der beschleunigten Elektronen notwendig. Ein großes Verbesserungspotenzial liegt in der Optimierung der Treiberlaserstabilität. Zusätzlich zur Verbesserung der passiven Stabilität bietet eine Erhöhung der Repetitionsrate die Möglichkeit aktive Stabilisierungen zu nutzen, um niederfrequente Störungen aus z. B. Luftfluktuationen und mechanischen Vibrationen zu stabilisieren. Das übergreifende Ziel dieser Arbeit war Lasersetups für die Terawatt (TW), Chirped-Pulse-Amplification (CPA), Ti:Sa Lasersysteme ANGUS und KALDERA zu entwickeln, die die Beschleunigung von hochqualitativen Elektronen ermöglichen.

Zur Verbesserung der Langzeitstabilität des ANGUS Lasers wurde ein neues, zuverlässigeres Front-End, basierend auf Optical-Parametric Chirped-Pulse Amplification (OPCPA), gebaut. Diese Arbeit beschreibt das Design, die Justage und die Charakterisierung eines Pulsstreckers, der zur Integration des Front-ends in den Gesamtlaser benötigt wurde. Das Ziel war der Bau eines stabilen und gut einstellbaren Streckers und die Minimierung der Winkeldispersion des Ausgangsstrahls mithilfe eines Drei-Farben-Lasers. Die Charakterisierung des Streckers und seine Implementierung in das Gesamtlasersystem, welche die Kompression von 31 fs Laserpulsen ermöglichte, wird beschrieben.

Der KALDERA Laser, ein Laser-plasma Beschleuniger (LPA) Treiberlaser mit >100 Hz Pulsrepetitionsrate, wird zur Zeit auf dem DESY Campus entwickelt. Um den >100 W Durchschnittsleistung im finalen Pulskompressor standzuhalten, werden Vielschicht-dielektrische (MLD) Gitter für den Pulskompressor benötigt. In dieser Arbeit wird die Entwicklung, der Aufbau und die Charakterisierung eines Zwei-Transmissionsgitter Öffner Streckers beschrieben, dessen Dispersion zu der des Kompressors passt. Der Strecker ermöglichte die erste Demonstration von Kompression von <30 fs Pulsen bei Ti:Sa Wellenlängen in einem Kompressor mit MLD Gittern. Die Charakterisierung der komprimierten Pulse zeigte, dass sich die verwendeten Konzepte für den KALDERA Laser und weitere zukünftige TW fs Lasersysteme mit hohen Durschnittsleistungen verwenden lassen.

Um die finalen Laserverstärker in KALDERA effizient zu betreiben, wird ein Boosterverstärker benötigt. Der designte Ti:Sa Verstärker erreichte in drei Durchgängen

Energien von 0.5-1 mJ mit <1 % Energiestabilität. Der entwickelte Strecker und Verstärker werden erfolgreich zum Betreiben des KALDERA Lasersystems eingesetzt und ermöglichen <0.5 % Energiestabilität im finalen Laserverstärker.

Contents

List of Figures

List of Tables

1 Introduction

Since their invention in the 1960s [1, 2] lasers have become a key component of many technological developments and an indispensable tool in innumerable fields, enabling scientific [3–5] and technological progress [6–9]. Their versatility in parameters such as frequency, energy, pulse duration, repetition rate and polarization allows the usage in ever new fields:

Terawatt and Petawatt peak power lasers can create previously non-accessible energy densities, that enable new technological approaches to e.g. fusion [10] and particle acceleration [11–14]. Their development was enabled by the concept of Chirped-Pulse Amplification (CPA) by D. Strickland and G. Mourou in 1985 [15]. Its key is to temporally stretch the laser pulses, to reduce their intensity during amplification and compress them again to short pulse lengths after. This way, intensity-induced effects such as self-focusing and damages can be avoided, enabling amplification to much higher pulse energies.

One technology, that profited greatly from the development of high-peak power lasers is Laser-Plasma-Acceleration (LPA) [11, 16–18]. The biggest advantage being its compactness. The acceleration happens when a high-intensity laser pulse generates a plasma and drives an oscillating (so-called) wakefield, that trails the laser pulse. Electrons, that are trapped in the correct phase of the field, are accelerated by high gradients, that originate in the charge separation between the electrons and their ions. These gradients can be several orders of magnitude higher, (up to GeV/m), than in conventional accelerators (tens of MeV/m) [19]. Thus, the acceleration length that is required to achieve comparable electron energies is reduced by orders of magnitude. This makes them a promising candidate for next-generation accelerators, promising compact, cost effective and more available high-quality electron sources, e.g. for the generation of high-brightness x-ray beams [20–23].

On the road to establishing LPAs as an alternative to conventional accelerators, many steps have been made already: The acceleration to electron energies of up to 8 GeV [24], bunch charges up to nC [25], transverse emittance of sub-1 mm mrad [26, 27] and fs-bunch duration [28] have been demonstrated. The applicability of plasma-accelerated electrons has been shown by generating undulator radiation and lasing in a free-electron laser [23]. However, for a performance, that is comparable to conventional accelerators, LPAs have to be further developed in many aspects: the stability of the generated electrons, especially over long operation times, has to be improved;

the repetition rate has to be increased from a few-Hz operation to the kHz or MHz repetition rates of conventional accelerators [29]. A higher repetition rate would also enable the possibility of active stabilizations that could compensate drifts in the tens of Hz range, which are often caused by air fluctuations or mechanical vibrations. In addition, higher repetition rates would allow for larger parameter studies of plasma accelerators. Those cannot be performed yet, due to a limit in operation time of most drive laser systems. Maier et al. have demonstrated, that a 24 h operation of a plasma accelerator is possible and such larger data sets can be used to study the sensitive correlations between laser and electron parameters [30]. Insights from such studies also enables tailoring the electron parameters to the needs of possible applications [18, 31, 32].

To achieve these next steps, especially the laser technology has to be advanced, to provide TW-level drive lasers, that operate at kHz repetition rate with great stability in all relevant parameters. Titanium-doped Sapphire (Ti:Sa) laser systems routinely demonstrate the required laser parameters for laser-plasma acceleration, e.g. <30 fs pulse duration, J-level energies with great temporal and spatial laser quality. However, the repetition rate of such systems is usually <10 Hz. Three key challenges can be identified for scaling a TW-level Ti:Sa CPA system to 1 kHz repetition rate:
First, the design of high-energy amplifiers operating at kW-average power. With a quantum defect of 36 %, Ti:Sa is prone to significant heat development inside the amplifier crystals, which increases with average power. Thermal effects such as thermal lensing, depolarization or heat-induced damage need to be tackled.
Second, the development of suitable pump lasers for these amplifiers that can operate at 1 kHz repetition rate. The fluorescence lifetime of the upper energy level in Ti:Sa is 3.2 µs[97]. To efficiently pump Ti:Sa crystals, pump lasers need to deliver the pump energy within a shorter time scale. This requires high peak powers, that cannot be reached by laser diodes. Currently, the last amplifier stages of TW-Ti:Sa systems are pumped by flash-lamp pumped, frequency doubled Nd:YAG lasers. Operation of these flash-lamps at 1 kHz is not possible, thus, new pump lasers have to be developed for the last amplifier stages.
Third, the design of the final pulse compressor. Compressor gratings in Ti:Sa amplifier systems are usually gold-coated, as the spectral efficiency supports a broad bandwidth, which is important for sub-30 fs pulse durations. But gold absorbs 3-4 % cite of the pulse energy, which reduces the efficiency, but more importantly leads to heating of the gratings. For high average power laser beams this heating can lead to deformation and or damage of the grating. Non-expanding substrates and cooling of the grating can prevent both effects for <1 kW average powers [36], but for further scaling a different grating technology is required. Multi-Layer Dielectric (MLD) gratings show a higher efficiency, much lower absorption and higher damage threshold. However, their coating only supports a limited bandwidth compared to gold gratings and has a

reduced acceptance angle. Thus, those gratings have been realized for the use with Ti:Sa lasers only recently.

Addressing these challenges and demonstrating kHz laser plasma-acceleration is the goal of the KALDERA project [33], which is currently under construction at DESY in Hamburg. The target output parameters of the final development stage are pulses with 3-4 J pulse energy, sub-30 fs pulse duration at 1 kHz repetition rate. This goal will be reached in three development phases, the first one aiming for 0.5 J pulses at 100 Hz repetition rate, the second increasing the energy to 3-4 J and the last one upgrading the repetition rate to 1 kHz.

This thesis was carried out in the context of the development and construction of the first development stage of the KALDERA laser system and the improvement of the operational ANGUS laser system [34], that drives the LUX laser-plasma accelerator [35]. Both laser systems have a chirped-pulse amplification (CPA) architecture, based on Ti:Sa amplifiers. The main topic is the development of two pulse stretchers. The first one is designed for the newly developed ANGUS front-end [36, 37], that provides a more stable seed energy and spectrum to the ANGUS laser. The stretcher enables its integration into the main laser system and is designed to match the compressor dispersion. It also provides good tunability and mechanical stability, enabling the improvement of the pulse duration stability at the plasma target to the sub-percent level.

The second stretcher is designed for the KALDERA laser system. It was developed to match a new compressor concept, which is based on MLD gratings. The first compression to sub-30 fs pulses at 800 nm with a compressor using MLD gratings could be achieved with the developed stretcher and a test compressor [38]. Afterwards the stretcher was integrated into the KALDERA laser system.
To enable an energy stable operation of the KALDERA Ti:Sa amplifier stages, the energy had to be increased after the stretcher. For this purpose, a Booster amplifier was developed. It provides an energy of >0.5 mJ with an energy stability of <1 % and a spectrum, that allows for compression to sub-30 fs. The operation of both subsystems enables amplification to >500 mJ at 100 Hz repetition rate in the final laser amplifier [39], which will, in the near future, drive laser plasma acceleration at 100 Hz.

In *chapter 1*, the phenomenon of laser-plasma acceleration will be described. The motivation behind the laser parameters of the KALDERA laser system will be given, by the laser requirements for efficient laser plasma acceleration. The basic architecture of CPA laser systems will be explained as well as the description of laser pulses and the mechanisms of laser amplification, especially in Ti:Sa. Finally, general challenges that arise in high-average, high peak-power systems will be discussed.

Chapter 2 focuses on the development of a pulse stretcher for the ANGUS laser system. The ANGUS laser system drives the laser-plasma accelerator LUX. During beam times,

parameter drifts in the commercial Ti:Sa front-end have been observed, which led to changes in the electron parameters. Thus, a new front-end, based on a white-light seeded OPCPA system was developed. The developed stretcher is an integral part of the new OPCPA front-end. The calculation of the spectral phase, combined with the planing of the optical layout will be presented. The mechanical setup and the alignment will be discussed. The characterization of the stretcher individually and the performance in combination with the rest of the system will be presented.

In *chapter 3* the development of a pulse stretcher for the KALDERA laser is presented. To achieve compressed pulses at the plasma target, stretcher and compressor dispersion have to be matched to each other. The increase in average power requires a change of the gold-coated compressor gratings to MLD gratings. They can be used most efficiently in the so-called Littrow-configuration, which has consequences on the spectral phase of the compressor. The design of a matching stretcher to this new type of compressor will be described. Its alignment and characterization will be reported, analogous to the characterization of the previously described stretcher. Finally, demonstration of compression to sub-30 fs pulses, using the stretcher in combination with a MLD grating based compressor and the characterization of the compressed pulses will be presented.

Due to limited grating efficiency and several passes, the stretcher causes energy losses of around 60 %. To compensate these losses to seed the main amplifiers of the KALDERA system efficiently, a Booster amplifier is required. The development of this amplifier will be discussed in *chapter 4*. The parameter space will be evaluated regarding different aspects, such as efficiency, thermal behavior and gain. The optical and mechanical setup will be described. The characterization of the final Booster includes a parameter scan, a long-term energy measurement and a caustic measurement. The integration of both the previously presented stretcher and Booster amplifier into the KALDERA laser system will be reported. Especially the beam shaping and the position and pointing stabilization will be discussed. Finally, sources of the amplifier output energy jitter will be evaluated.

In the last chapter, a summary of the results will be provided. An outlook will be given to the further development and improvement of the presented setups.

2 Publication list

Part of the results in this thesis have been peer-reviewed and published in the following second-authored journal article.

1. C. Werle, **C. Braun**, T. Eichner,T. Hülsenbusch, G. Palmer and A. R. Maier, *Out-of-plane multilayer-dielectric-grating compressor for ultrafast Ti:sapphire pulses*, Opt. Express 31, 37437 - 37451 (2023) [38]

The following publications are remotely related to this thesis but report on work primarily done by others.

2. S. Jalas, M. Kirchen, **C. Braun**, T. Eichner, J. B. Gonzalez, L. Hübner, T. Hülsenbusch, P. Messner, G. Palmer, M. Schnepp, C. Werle, P. Winkler, W. P. Leemans, and A. R. Maier, *Tuning curves for a laser-plasma accelerator*, Phys. Rev. Accel. Beams 26, 071302 (2023) [32]

Contributions to international conferences

Some results regarding the work on the KALDERA stretcher and out-of plane compressor have been published as conference contributions:

1. C. Braun, C.Werle, G. Palmer and A.R. Maier, *Stretcher design for matching an out-of-plane MLD grating compressor*, Helmholtz Meeting on Optics, Photonics and Lasers, Hamburg, 2024 [40]
2. C. Braun, C.Werle, T. Eichner, G. Palmer and A.R. Maier, *Concepts for High Average Power Ti:Sa Laser Pulse Compressors*, Bad Honnef Physics School on Plasma Acceleration, Bad Honnef, 2023 [41]
3. C. Braun, C.Werle, T. Eichner, G. Palmer and A.R. Maier, *Concepts for High Average Power Ti:Sa Laser Pulse Compressors*, Conference on High Intensity Laser and attosecond science in Israel, Tel Aviv, 2022 [42]
4. C. Braun, C.Werle, T. Eichner, G. Palmer and A.R. Maier, *Concepts for High Average Power Ti:Sa Laser Pulse Compressors*, Matter and Technology Meeting , Hamburg, 2022 [43]

3 Laser pulse amplification for laser-plasma acceleration

As described in the introduction, the scope of this thesis is to develop a stretcher and a Booster amplifier for a laser system which will be used for laser-plasma-acceleration at kHz repetition rate (KALDERA) and a stretcher for the new OPCPA front-end of the ANGUS laser, that drives the LUX laser-plasma-accelerator. To understand the requirements for such laser systems, the basic principles of laser-plasma-acceleration have to be considered and will be briefly described in the following. From this, target output beam and pulse parameters of the KALDERA laser will be motivated, that are relevant for the design of the later described subsystems. The goal is to understand the necessity for sub-50 fs laser pulse durations and for high pulse quality, especially low pulse-front tilt.

3.1 Laser plasma acceleration

The following description of the basics of laser plasma acceleration follows [36].
Figure 3.1 shows a schematic of the acceleration process. A short laser pulse with high-intensity creates a plasma in a gas. The propagating laser pulse pushes the electrons with the ponderomotive force $\vec{F}_{pond}$

$$\vec{F}_{pond} = -\frac{e^2}{4m_e\omega^2}\vec{\nabla}(\vec{E}^2), \tag{3.1}$$

that can be interpreted as radiation pressure. It pushes the electrons along the gradient of the intensity in forward and radial direction. The much heavier ions are not affected and remain at their position. This creates a charge separation and the electrostatic field between the electrons and the ions pulls the electrons back, leading to a longitudinal periodic electron density modulation and electric field, called the wakefield. Its period length is the plasma wavelength λ_p, which is given by

$$\lambda_p = \frac{c}{2\pi}\sqrt{\frac{m_e\epsilon_0}{n_e e^2}}, \tag{3.2}$$

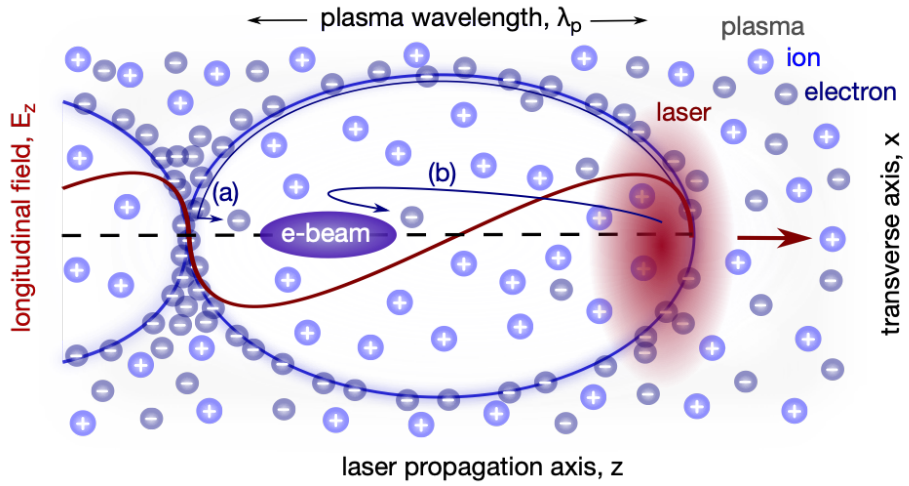

Figure 3.1 – Schematic of the process of laser-plasma-acceleration in the bubble-regime. The drive laser pulse creates a charge separation, which creates an electric field, in which an electron bunch can be accelerated in the rear part of the bubble. Courtesy P.Winkler

where n_e is the electron density, c is the speed of light in vacuum, m_e is the electron mass, e is the electron charge and ϵ_0 is the vacuum permittivity of the electric field. For typical plasma parameters at LUX, this results in $\lambda_p \simeq 30\,\mu m$.
The shape of the wakefield is highly determined by the intensity of the laser pulse, which can be described by the normalized peak vector potential a_0 (see equation 3.3).

$$a_0 = 8.55 * 10^{-10} \lambda_l[\mu m] \sqrt{I_0[W/cm^2]} \tag{3.3}$$

For $a_0 < 1$ the electrons move in a non-relativistic way and the wakefield can be described as a sinusoidal wave. For $a_0 > 1$, the plasma wave reaches the non-linear regime, where the wakefield starts deviating from a sinusoidal shape. The so-called bubble- or blow-out regime is reached, when $a_0 \gg 1$ and when the electrons, that are pushed aside by the laser, reach relativistic speed, within one oscillation of the laser electric field. From equation 3.3 an estimation of the minimal laser intensity can be made, which is required to drive a nonlinear wakefield. Assuming a wavelength of 0.8 µm, where e.g. Ti:Sapphire lasers emit, the minimum intensity $I_{non-lin}$ is around $10^{18}\,W/cm^2$. This gives a first boundary condition for the laser pulse and beam properties. To learn more about the optimal laser parameters for efficient driving of the plasma wakefield, the resonance conditions of this process can be discussed.

To accelerate the electrons efficiently, the excitation of the wakefield should happen resonantly. As the ponderomotive force acts in the direction of the gradient of the laser pulse intensity, the rising edge of the pulse pushes the electrons in the forward

direction, while the falling edge of the pulse pushes them backwards. If this coincides with the movement of the electrons from the plasma oscillation, the wakefield is excited resonantly. This is the case if $c\tau_{pulse} \simeq \lambda_{plasma}/2$. In general, it is advantageous if the laser pulse is rather shorter than longer than the plasma bubble, to not interfere with the trapped electrons at the end of the bubble.

A similar condition is valid for the spatial distribution of the laser. In the nonlinear regime, the ponderomotive force acts transversely as well. This means the electrons are not only pushed to the front, but also to the sides by the laser pulse. Thus, the transverse intensity distribution should fulfill a similar resonance condition as the pulse length: $2w_0 \simeq \lambda_{plasma}$. For a typical plasma density of 10^{-18} the spatial and temporal resonance conditions results in a desired pulse length $\tau \simeq 18\,\mathrm{fs}$, corresponding to around 40 fs FWHM for a Gaussian pulse shape, and a beam waist w_0 of 16 µm. Using these parameters and the previously established condition for the intensity $\mathrm{I}_{non-lin}$, the minimal required laser pulse energy is E_{laser}=3-5 J. These parameters are realistic for efficient laser-plasma-acceleration to energies in the 100s of MeV range [44].

The strong dependence of the wakefield on the laser intensity is one of the reasons for the sensitivity of the electron parameters to the laser parameters. Especially variations in the laser energy, the pulse duration and the focus position affect the parameters of the accelerated electrons, such as electron energy, energy distribution and charge [30, 45, 46]. A sub-percent energy and pulse duration stability as well as sub-µm wavefront stability of the laser at the plasma target are required for sub-percent electron energy stability.

Laser pulses with J-level energy and fs pulse duration can be generated in laser systems, that are based on chirped-pulse amplification (CPA), often using Ti:Sapphire as gain medium [47–49]. In the following, the working principle of CPA laser systems will be described, starting at the mathematical description of laser pulses and dispersion effects. Then the CPA-working principle is explained in more detail and the basic principles of laser amplification are discussed. Finally, the challenges of ultrashort laser pulse systems, specifically Ti:Sa CPA systems, will be discussed and how non-ideal laser pulses affect the electron acceleration in LPAs.

3.2 Laser pulses

3.2.1 Description of laser pulses

The following description of the mathematical representation of laser pulses is based on section 5.1 in [50].
One way to categorize lasers is to differentiate between continuous wave (cw) lasers and pulsed lasers. While the amplitude of the electrical field oscillation is constant

over time for cw lasers, it is time-dependent in a laser pulse. In the time-domain, the electric field of a laser pulse can be written as

$$E(t) = A(t)e^{i(\omega_0 t+\phi(t))} + c.c., \tag{3.4}$$

where $A(t)$ is the time-dependent amplitude of the laser pulse. ω_0 is the carrier frequency, from which the carrier wavelength λ_0 can be derived as ω_0/c. $\phi(t)$ is the temporal phase, which equals the phase offset between the envelope $A(t)$ and the carrier wave.
To describe the temporal shape of a pulse, often, the oscillation-averaged intensity $I(t)$ is used, that, in vacuum, is given by:

$$I(t) = \frac{c\epsilon_0}{2}|A(t)|^2 \tag{3.5}$$

with c, the vacuum speed of light and ϵ_0, the vacuum permittivity. Commonly, the width of $I(t)$ at its $1/\sqrt{e}$, 1/2, 1/e or $1/\mathrm{e}^2$ level is used to define the pulse length. In this thesis, the width at 1/2 level of $I(t)$ (FWHM) is used to define the pulse length Δt.

The temporal change in intensity of a laser pulse is caused by the coherent overlap of electric fields with different frequencies within a certain range, centered around a carrier frequency of ω_0. Thus, laser pulses can be described in the spectral domain, equivalently to the description in the temporal domain. The frequency-dependent electric field $E(\omega)$ can be retrieved by a Fourier transform of $E(t)$:

$$E(\omega) = \int_{-\infty}^{\infty} E(t)e^{i\omega t}dt, \tag{3.6}$$

with the inverse transformation

$$E(t) = \frac{1}{2\pi}\int_{-\infty}^{\infty} E(\omega)e^{-i\omega t}dt. \tag{3.7}$$

It is often given in the form

$$\tilde{E}(\omega) = A(\omega)e^{i\phi(\omega)} \tag{3.8}$$

with $A(\omega)$ being the spectral amplitude. The spectral intensity can thus be calculated analogously to the temporal intensity $I(\omega) \sim |A(\omega)|^2$. It will also be called spectrum in the following and is often given as $I(\lambda)$. Its FWHM will be used as measure of the spectral width $\Delta\lambda$ of a pulse.

$\phi(\omega)$ is the spectral phase of the pulse, which for a fixed $A(\omega)$ defines the temporal shape and width of a pulse. It describes the relative phase between the frequencies of the pulse and the carrier frequency ω_0. For a more accessible description and

quantification one can perform a Taylor expansion of $\phi(\omega)$:

$$\phi(\omega) = \phi(\omega)^{(0)}_{\omega_0} + \phi(\omega)^{(1)}_{\omega_0}(\omega-\omega_0) + \frac{1}{2}\phi(\omega)^{(2)}_{\omega_0}(\omega-\omega_0)^2 + \frac{1}{6}\phi(\omega)^{(3)}_{\omega_0}(\omega-\omega_0)^3 + \mathcal{O}((w-w_0)^4) \tag{3.9}$$

$$\phi(\omega)^{(n)}_{\omega_0} = \left.\frac{d^n\phi(\omega)}{d\omega^n}\right|_{\omega_0} \tag{3.10}$$

The different components of the Taylor expansion can be interpreted physically and the meaning of the first four contributions are:

- $\phi(\omega)^{(0)}_{\omega_0}$: This describes the carrier-envelope-phase, which is the phase difference between the pulse envelope and the oscillating electric field. It becomes relevant in few-cycle pulses. The pulse durations described in this thesis are much longer than this, thus this component is of no concern in this thesis.
- $\phi(\omega)^{(1)}_{\omega_0}$, group delay (GD): Delay of the whole pulse in time. For considerations of the pulse length and shape this term can be neglected.
- $\phi(\omega)^{(2)}_{\omega_0}$, group delay dispersion (GDD): It gives the rate at which the frequency is changing within the pulse, which is called chirp. For strongly chirped pulses it is linearly proportional to the pulse length.
- $\phi(\omega)^{(3)}_{\omega_0}$, third order dispersion (TOD): It is the cubic spectral phase and it can cause pre- or post-pulses. An example of this will be shown later in chapter 5.

The sum of the contributions with order n≥2 are called dispersion $D(\omega)$. Pulses with a spectral phase $\phi(\omega)^{(2)}_{\omega_0} \neq 0$ are called chirped or stretched.

The fact, that the spectral and the temporal representation of the pulse are related by Fourier transformation means that there is a relation of the spectral and temporal width. The pulse length Δt and the spectral width (FWHM) of a Gaussian-shaped laser pulse are connected by [51]

$$\Delta\lambda = \frac{2ln2}{\pi}\frac{\lambda_0^2}{c\Delta t}. \tag{3.11}$$

For example, a Gaussian pulse of Δt=25 fs at 800nm central wavelength, a spectral width $\Delta\lambda$ of 38 nm is required. This means the spectral bandwidth determines the minimal pulse length that can be reached. This minimal pulse length is also called Fourier transform limit (FTL) and pulses of this length are called Fourier-limited. Their spectral phase has to fulfill the condition $\phi(\omega)^{(2)}_{\omega_0} = 0$.
To shape a laser pulse temporally, either the phase or the spectrum must be manipulated. One example is the temporal stretching and compression of pulses. This is the key part of the concept of chirped-pulse amplification, which is going to be described in section 3.3.

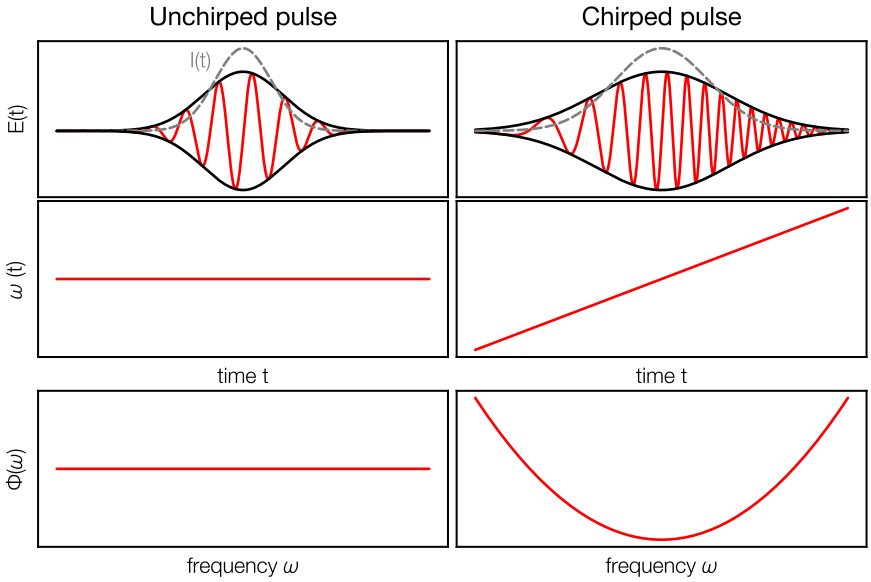

Figure 3.2 – Top: Illustration of the electric field $E(t)$ (red), including the envelope function $A(t)$ and the resulting temporal intensity $I(t)$(grey, dashed) of a temporally compressed pulse (left) and a temporally chirped pulse (right). Middle: Instantaneous frequency of the pulse. Bottom: Spectral phase of the compressed (left) and chirped pulse.

3.2.2 Angular and spatial chirp and pulse front tilt

The previous considerations described pulses with temporal or spectral phase, but a perfect spatial overlap of all colors in the beam. Real pulses however often deviate from this ideal. Apart from wavefront aberrations, that can occur in monochromatic light as well, laser pulses can suffer from spatio-temporal couplings (STCs). This means, that spatial and temporal (or spectral) modes cannot be described independently anymore. These STCs can impact both the laser amplification and the laser-plasma-acceleration process. In the following, the STC pulse-front-tilt and the related angular chirp will be described briefly.

As it was discussed earlier laser pulses are not monochromatic, but contain several frequencies or wavelengths. During propagation through materials, different frequencies generally behave differently. The frequency or wavelength dependent refractive index $n(\lambda)$ reduces the phase velocity in the material to $v_{ph}=c/n(\lambda)$. This not only changes the spectral phase of the pulse, but can lead to a wavelength dependent propagation angle (angular chirp). This not only occurs during material propagation but in any dispersive setup, such as stretchers and compressors.
Angular chirp has several consequences: First, it leads to the spatial separation of the colors (spatial chirp). Second, when focusing the beam, it leads to an increase in the focus spot size. Due to the different angles, the colors have a different transverse

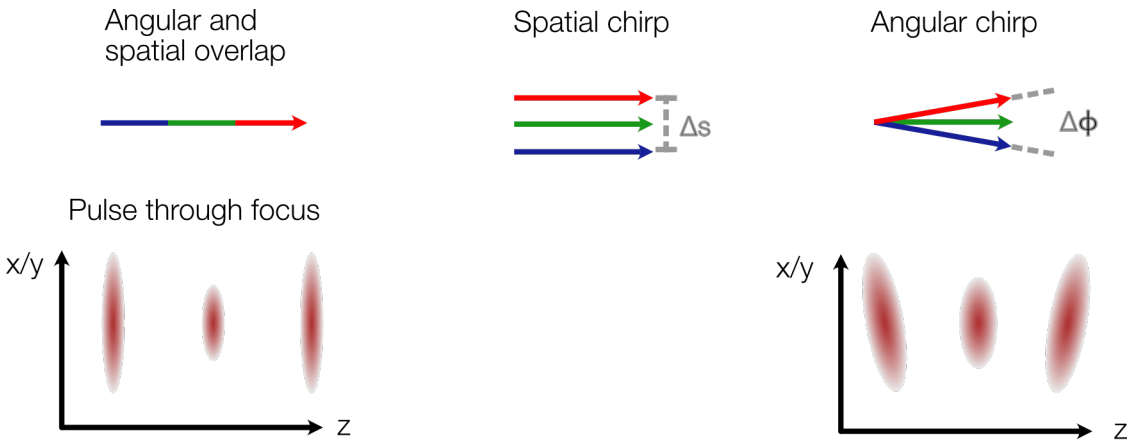

Figure 3.3 – Top: Illustrations of overlapping and copropagating beams of different colors (left), a spatially chirped beam (middle), angularly chirped beam (right). Bottom: Qualitative illustration of the pulse intensity during propagation through a focus, without angular chirp (left) and with angular chirp (right).

focus position, which enlarges the focus spot, even if the individual colors' foci are diffraction limited. Third, the pulse length of the compressed pulse can be increased. Due to spatial separation of the colors, the local bandwidth reduces, leading to a longer pulse length. The last two effects both reduce the focus intensity.
In laser-plasma acceleration, this can hinder efficient electron acceleration. In addition to the reduced intensity, when the angularly chirped beam is focused to the plasma target, the pulse front tilts before and after the focus. With the ponderomotive force acting along the gradient of the pulse intensity it can be understood, that this can steer the electrons transversely.
In figure 3.3, spatial and angular chirp are illustrated at the top. In the bottom, the spatial intensity distribution through a focus is represented for a pulse with an ideal wavefront (left) and for an angularly chirped beam (right). The spatial and temporal enlargement and the tilt of the pulse can be noticed.
Angular chirp not only affects the plasma acceleration, but also the amplification in laser amplifiers, that will be described in the following. If the colors are spatially spread in the gain material, the overlap with the pump beam influences the gain of the individual wavelengths, likely affecting the output spectrum. The precise effect depends strongly on the amount of chirp, the pump and seed sizes and shapes and the amplification gain.
Especially the highly dispersive elements in a chirped pulse amplification (CPA) laser system, the stretcher and compressor can cause residual angular and spatial chirp, if they are not perfectly aligned. In the following these systems will be introduced. In chapter 4 an alignment method will be presented that is used to minimize the angular

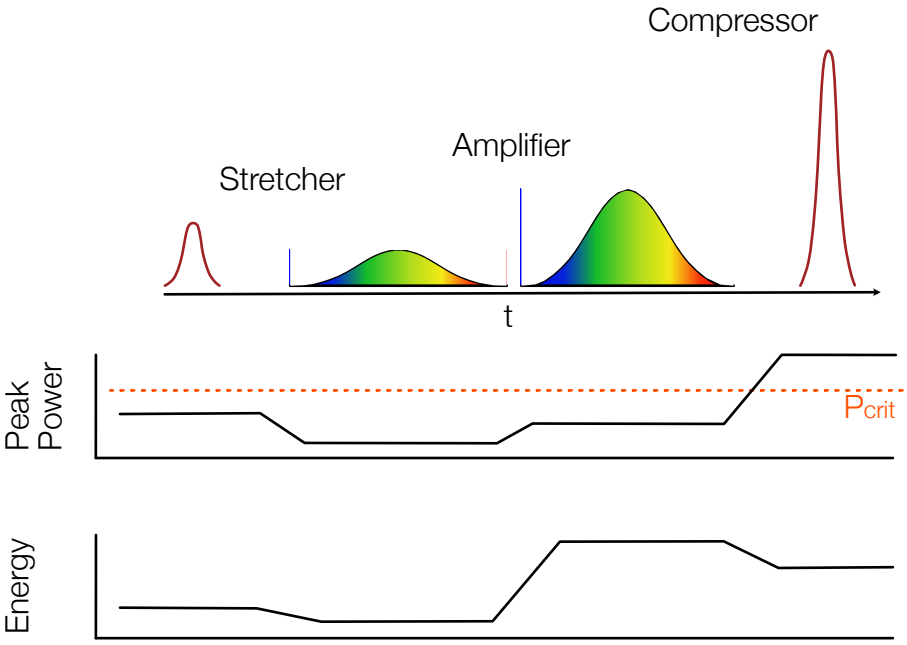

Figure 3.4 – Principle of chirped-pulse-amplification (CPA). The peak power is decreased by the stretching in time and stays below P_{crit} when the energy is increased in the amplifier. After amplification, the pulses are compressed and reach their final peak power.

chirp after pulse stretchers or compressors. The limits of acceptable angular chirp for the presented laser systems will be discussed as well.

3.3 Chirped-Pulse-Amplification (CPA)

Since its demonstration by D. Strickland and G. Mourou [15] Chirped-Pulse-Amplification (CPA) has been used in a variety of high-peak-power laser systems ranging to the PW-level [47–49, 52]. In the following, the principle and the key components, stretcher and compressor, are going to be presented.

3.3.1 Principle

CPA was developed to prevent non-linear effects, such as self-focusing and damage in optics during laser amplification, which were limiting the achievable pulse energy of laser pulses. Its principle is sketched in figure 3.4. The short, but low-energy pulses at the beginning of the laser system are stretched in time, using the spectral composition of laser pulses. The stretched pulses are then amplified to higher energies in one or more laser amplifiers, but because they are stretched, their peak power stays below

the critical power for self-focusing P_{crit}. Only in the final compressor, the pulses are compressed to their short pulse length again, reaching their final peak power. To keep the intensity low and avoid the destruction of the compressor optics, the beam size is increased, too. Only in the final experiment, the laser pulse is focused to a small spot size and reaches its desired goal intensity.

3.3.2 Pulse stretching and compression

Pulse stretchers and compressors are temporally dispersive setups, which means they change $\phi(\omega)$ of a laser pulse by introducing a spectrally dependent delay to the pulse ($\Phi(\omega)^{(2)}_{\omega_0} \neq 0$). This leads to the spectrum being sorted in time and thus the pulse being stretched in time. To compress an already stretched pulse, the dispersion of the compressor has to have the opposite sign of the dispersion of the stretcher. For TW class lasers and their grating stretchers and compressors it is common to introduce a positive chirp $\frac{\delta\omega}{\delta t} > 0$ in the stretcher and a negative chirp $\frac{\delta\omega}{\delta t} < 0$ in the compressor. To achieve a Fourier-limited pulse after compression, the compressor dispersion, the dispersion of the whole laser system and the stretcher, have to add up to zero over the spectral range of the pulse, as it is expressed in

$$D_{tot}(\omega) = D_{Stretcher}(\omega) + D_{LaserSystem}(\omega) + D_{Compressor}(\omega) = 0 \tag{3.12}$$

More details on the individual contributions and how the dispersion of the individual sections can be matched will be discussed in the chapters 4 and 5. In the following, a short overview over different stretching and compression methods is given.

Different setups can be used to stretch and compress optical laser pulses. Common are the use of fibers, prisms, (double-)chirped-mirrors (DCM) or gratings [15, 53–55] but any setup applying a defined dispersion to an optical pulse can in principle be used. It is also possible to combine different concepts in one setup.

All of the mentioned setups introduce the phase shift independent of the intensity of the pulse. In contrast to this, non-linear effects like B-integral or self-phase modulation are intensity dependent and thus act differently on different parts of the pulse, depending on the instantaneous intensity. The on-axis, non-linear phase, the B-integral is given by (from [56])

$$B = \frac{2\pi}{\lambda} \int n_2 I(z) dz [rad]. \tag{3.13}$$

The B-integral depends on the wavelength of the pulse λ, on the non-linear refractive index n_2 of the passed material and the on-axis intensity I(z). If it becomes significantly larger than 1 over a short distance, due to high intensity in a medium, non-linear processes like Kerr-lensing, self-focusing and self-phase modulation can be initiated.

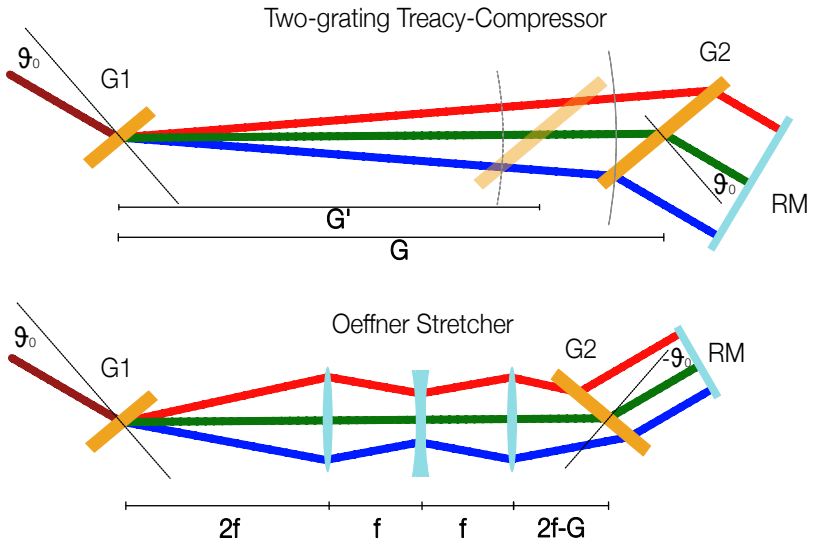

Figure 3.5 – Conceptual layout of a grating compressor and an Oeffner grating stretcher. Both are depicted with transmissive optics. Distance G between Grating 1 and 2 (G1 and G2) defines the stretching factor, the grating incidence angle θ defines the angular chirp after the first grating. After G2, the beam is spatially chirped and is sent back through the setup at a different height by a roof-mirror. While the 'red' part of the spectrum has a longer way in the compressor, it has a shorter way in the stretcher. The beam angles are inverted by the Oeffner telescope, which allows to place the second grating at the negative angle.

This process has to be taken into account in the design of a laser system and intensities should be chosen such, that accumulation of B-integral is avoided [56].

After discussing the effect of modulation of the spectral phase and presenting a few possibilities of phase manipulation, we will now concentrate on the setups, that are often used in TW CPA systems, which are grating-based stretchers and compressors. They are chosen for their large stretching factors and their broad spectral range and flexibility. In the following, the principles and typical layouts of grating compressors and stretchers will be presented.

Treacy grating compressors

In the following the Treacy compressor [57] will be described, as this model is used in the laser systems, described in this thesis. In grating compressors the spectral phase is changed by spectrally dependent propagation distances. This can be seen in figure 3.5. The beam meets the grating under the angle ϑ_0. It is then diffracted, where every

wavelength, following equation 3.14, is diffracted with a different angle ϑ [58].

$$\vartheta = arcsin(-\frac{\lambda}{d}) - \vartheta_0 \tag{3.14}$$

After a propagation distance of G, it meets the second grating. This is placed parallel to the first one, and compensates the angular chirp. The spectral phase originates in the wavelength dependent path length. Longer wavelengths (red beam) propagate further, than shorter ones (blue beam). The larger the grating distance G is, the larger the difference in propagation length and thus the phase shift. This is visualized in the sketch. The curved lines indicate the position where all wavelengths have traveled for the same distance, when the shortest wavelength hits the grating. It is indicated for two grating distances G and G'. The distance between the curved line and the position, where the middle and the longest wavelength hit the grating are longer, when the grating distance is larger. It can be noted, that the longer the grating distance becomes, the larger the grating has to be.
After the second grating, the pulse is still spatially split in its colors. To compensate for this, either a second grating pair is placed in a mirrored orientation to the first pair or a roof-mirror sends the beam through the setup again. This way, the spatial chirp is compensated and the phase shift is doubled as the same path length difference is introduced to the pulse again.
The expressions for the GDD and TOD that is caused by an in-plane Treacy compressor are given in equations 3.15 and 3.16[59].

$$\mathrm{GDD}(\lambda) = -\frac{\lambda^3 G}{\pi c^2 d^2}\left[1 - \left(\frac{\lambda}{d} - \sin\vartheta_0\right)^2\right]^{-\frac{3}{2}} \tag{3.15}$$

$$\mathrm{TOD}(\lambda) = -\frac{3\lambda}{2\pi c}\,\mathrm{GDD}\,\frac{1 + \frac{\lambda}{d}\sin\vartheta_0 - \sin^2\vartheta_0}{1 - \left(\frac{\lambda}{d} - \sin\vartheta_0\right)^2} \tag{3.16}$$

The parameters in these equations are: ϑ_0, the grating incidence angle, d, the length of the grating period, G, the distance between the gratings and the center wavelength λ. The grating period length d is usually given by the grating manufacturer. The GDD can finally be tuned by the grating distance G. The TOD can then be adjusted by the input angle ϑ_0. For the later matching of the spectral phase of stretcher and compressor, not these formulas, but ray-tracing of a compressor model in a ray-tracing program OpticsStudio (OS) is used. In chapter 5, the Treacy compressor as it was described before is modified, as the diffracted beams will be sent out of the incoming plane. This model is called out-of-plane compressor, it can however be described like an in-plane Treacy compressor, with a slightly increased line density [38].

After understanding the principle of a grating compressor, we will discuss its counterpart, the Oeffner stretcher in the following.

Oeffner stretcher

The Oeffner stretcher is a commonly used stretcher type, with gratings as dispersive component and an Oeffner telescope [60], as the imaging system, that is necessary to create the positive chirp for the pulse. This is visualized in the bottom scheme in figure 3.5. The Oeffner telescope consists of a focusing optic with focal length f and a defocusing optic (f/2), that are spaced with a distance f. The telescope flips the angles of the beams, so that the second grating is placed with -ϑ_0. This way, the longer wavelengths travel a shorter distance and positive dispersion is introduced. In figure 3.5 lenses were used as optics to simplify the illustration.

In an Oeffner stretcher, commonly mirrors are used as focusing and defocusing optics. They are arranged such that their curvatures are concentric as it can be seen in figure 3.6. To compensate the spatial chirp in the beam after the first pass, two passes through the stretcher are necessary. To separate in- from outgoing beams either polarization rotation or height steps can be used.

Several possible configurations are possible, to realize an Oeffner stretcher, some of which will be described in the following:
In general, a configuration with one, or two gratings is possible. Schemes of both variations (both with transmission gratings) are shown in figure 3.6. When one grating is used, it is positioned between the center of the concentric telescope and the defocusing mirror. In the two-grating-configuration the first grating is placed in the center of the telescope, the second is placed between the first and the defocusing mirror. Advantages and disadvantages of both variations are going to be discussed later.
Due to the reflective optics, such a stretcher has to be setup set up in a configuration, where the beam circumvents the defocusing mirror. Two possibilities are shown in the side views in figure 3.7.

In stretchers with spherical mirrors, the beam is sent in parallel to the symmetry axis of the stretcher. It hits the spherical mirror off-centered, which introduces a kick in the non-dispersive direction. After propagating over the defocusing mirror and focusing mirror again, the kick is eliminated and the beam is parallel to the input beam at a mirrored height.
In the cylindrical stretcher, the beam is sent in under an angle to the telescope symmetry axis. This angle stays constant as the telescope mirrors are flat in the vertical direction. A simple mirror or a roof-mirror can send the beam back, either at a slightly different angle or at a height step.
Both setups have their advantages and disadvantages. The spherical mirror setup

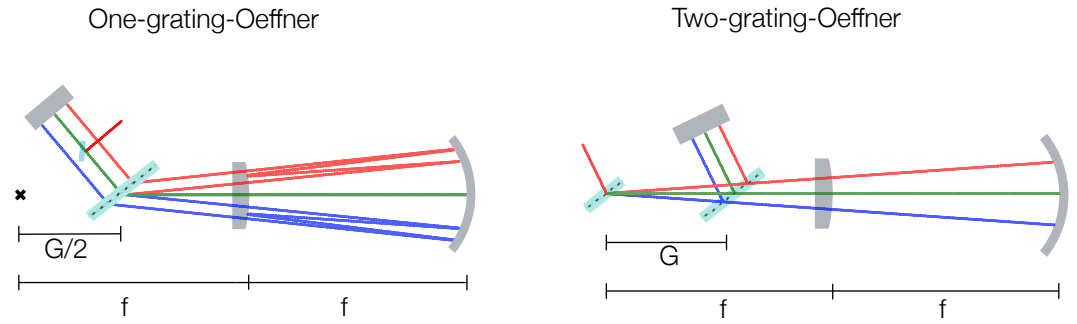

Figure 3.6 – Layout of a one-grating stretcher (left) and a two-grating stretcher, including the beam propagation of three representative wavelengths through the stretchers. The defocusing mirror is placed in the focus of the focusing mirror.

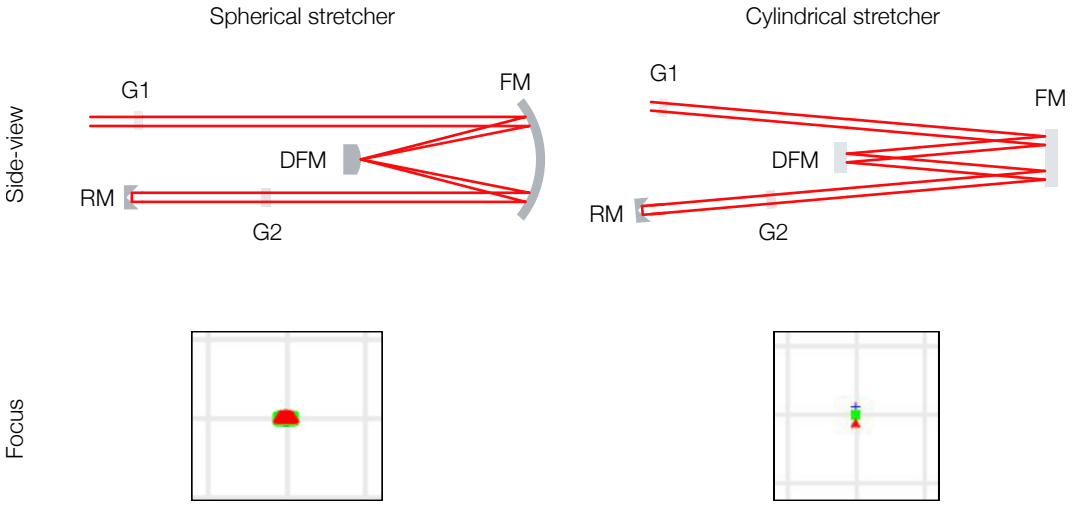

Figure 3.7 – Comparison of two Oeffner stretcher configurations. On the left, spherical mirrors are used, that introduce a height step in the telescope, that is symmetric to the telescope axis. In the right setup, cylindrical mirrors are used, that seem flat from the side, thus the incoming beam is angled. In the bottom the spatial chirp in the far-field is shown for both setups.

is easier to align as most beams are parallel to the table plane. In a two-grating setup, no residual angular or spatial chirp remain in the beam as can be seen from the overlapping spots in the simulated focus.
The advantage of the cylindrical setup is, that the beam is not focused in the non-dispersive plane, which increases the spot size and thus improves the contrast of the compressed pulse [61]. However some residual spatial and angular chirp is in the beam even for an optimal alignment.
We decided to use the spherical mirror design for its easier geometry and the better spatial overlap of all colors in the focus as it can be seen in figure 3.7 (bottom left). With regard to their temporal dispersion, however, both stretchers behave

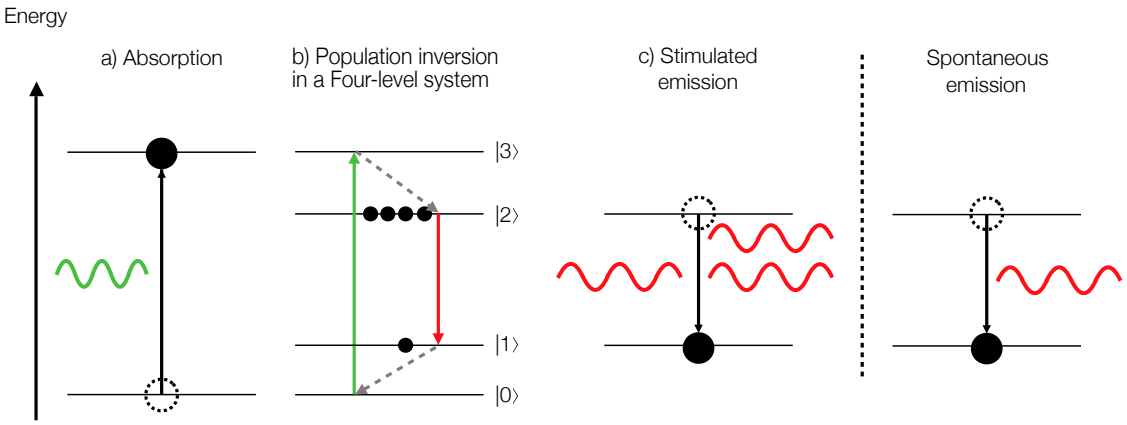

Figure 3.8 – Basic principles of laser amplification. Displayed are stimulated absorption (a), a four-level laser system with population inversion in the lasing transition (b) and stimulated emission (c). Spontaneous emission is depicted as additional process, that occurs in lasers.

(approximately) the same and both can be matched to a compressor. The matching of a spherical Oeffner stretcher to a Treacy-compressor will be described in the sections 4.1 and 5.3.

In the last part, the mechanism and realization of the pulse stretching and compression of the laser pulses was described. In the next section, the amplification of laser pulses will be explained.

3.4 Laser amplification in Titanium-doped:Sapphire lasers

The laser parameters required for laser plasma acceleration, estimated in section 3.1, (3-5 J, <30 fs), are routinely reached by lasers, that use titanium-doped sapphire (Ti:Sa) as gain medium. In the following, the basics of laser amplification are presented, with an emphasis on Ti:Sa lasers.

3.4.1 Basic principles of laser amplification

The generation and amplification in light-pumped laser amplifiers requires three basic processes: Stimulated absorption, population inversion in the laser gain medium (three- or four-level system) and stimulated emission. They are sketched in figure 3.8. A photon of a certain wavelength can be absorbed, if it provides the same energy difference of the electron transition. If this is the case, the electron, represented by the black circle, transits to a higher energy level (a). From there it can either decay spontaneously under the emission of a photon (right sketch), or another photon can

stimulate the decay by passing the medium (c). In this case, the emitted photon is of the same wavelength, polarization and direction as the stimulating photon, which effectively amplifies the incoming light.
The probability of absorption and emission of a photon in the same transition per electron is the same. Thus, to amplify light in a medium, the electron population in the upper energy level has to be larger, than in the lower. This state is called (population) inversion. To reach it, a three- or four-level system is required (b), as it is sketched in 3.8 (left). The pump light excites the electrons to an upper level (|3>), from where they quickly decay via a non-radiative, transition to the upper level of the lasing transition |2>. This way the electrons accumulate on level |2>. The lasing takes place between level |2> and |1>. Energy level |1> is emptied again by a fast non-radiative transition. This way the inversion is created between |1> and |2> and amplification of the incoming light can happen efficiently.
The two non-radiative transitions lead to a difference in energy between the pump photons and the signal photons, which is called the quantum defect.

$$\eta_{QD} = \frac{\lambda_{pump}}{\lambda_{seed}}. \tag{3.17}$$

In three-level laser gain materials, the quantum defect is usually lower, due to only one non-radiative decay. Thus, they can be pumped more efficiently. However, it is harder to achieve population inversion.

If the population inversion is not reduced by stimulated emission, it decays by itself, by spontaneous emission. In Ti:Sa the half-life of this process is $\tau_{Ti:Sa}$=3.2 µs [97]. For efficient laser amplification, the delay between pump and seed should be $\ll \tau_{Ti:Sa}$. Until the population inversion is depleted, the spontaneously emitted radiation can be amplified as well. This phenomenon is called amplified spontaneous emission (ASE) and its strength depends on the available gain. If the gain is higher, than the losses at the crystal surface, even spontaneous lasing can occur within the gain medium. This can happen along the longitudinal or the transverse direction to the intended beam direction (transverse lasing). This free-lasing should be avoided as it poses a competitive process to the intended laser amplification. It can be suppressed, by increasing the losses at the crystal surfaces, e.g. by adding anti-reflective coatings or refractive index matched media.

3.4.2 Calculation of amplification gain with Frantz-Nodvik equations

To calculate the gain of a laser amplifier, the 1D Frantz- Nodvik equations can be used as first approach.

$$G_0^{(p)} = exp(J_{stored}/J_{sat}) \tag{3.18}$$

G_0 is the small signal gain, which is the gain a signal, that is much below the saturation energy, experiences. It depends on the stored fluence J_{stored}, which is the stored energy E_{stored} per pumped area A. It can be estimated by the pump fluence, that is sent into the crystal, multiplied with the absorption coefficient, the quantum defect and the quantum efficiency, which is the fraction of the electrons that can take part in the amplification process. J_{sat} is the saturation fluence, which is a gain medium dependent parameter.
From the gain, the fluence after one pass through the amplifier $J_{out}^{(p)}$ is given by

$$J_{out}^{(p)} = J_{sat} \cdot ln(1 + G_0^{(p)}[exp(J_{in}^{(p)}/J_{sat} - 1)]). \tag{3.19}$$

It depends on the small signal gain $G_0^{(p)}$, the saturation fluence J_{sat}, and on the relation between the input fluence J_{in} and the saturation fluence.
For a multipass amplifier, the gain has to be calculated for every pass p individually. After one pass of amplification, both the available pump fluence and thus the small signal gain and the input fluence have to be calculated again, as some energy was extracted already.

The Frantz-Nodvik equations as they are given above are only one-dimensional in the sense, that only the average fluence of pump and seed are considered, which corresponds to perfectly overlapping flat-top beam profiles. Furthermore, no spectral or temporal dependencies are included. The equations can however be expanded to a 3D space and a temporal and spectral consideration is possible as well.

This is required if the spectral effects of the amplification need to be considered. In CPA laser systems this includes:

- Red-shift: Due to the positive chirp of the pulses, the red part of the spectrum sees the full gain in the crystal, while the blue part sees a partially depleted gain. This leads to a red-shift of the spectrum.
- Gain narrowing: Because the center of the spectrum has the highest fluence and thus sees a higher gain, than the outer wavelengths of the spectrum, the spectrum becomes narrower.
- Spectrally selective amplification, due to spatial and angular chirp: If the seed beam is spatially chirped inside the amplifier crystal, not all wavelengths might overlap well with the pump gain. This can lead to a spectrally varying amplification and to shaping of the spectrum.

One way to mitigate gain narrowing and red-shift is to modulate the spectral amplitude before the amplifier chain e.g. with an acusto-optic dispersive filter (AOPDF). If the central and red wavelengths are attenuated, gain narrowing and red-shift are reduced.

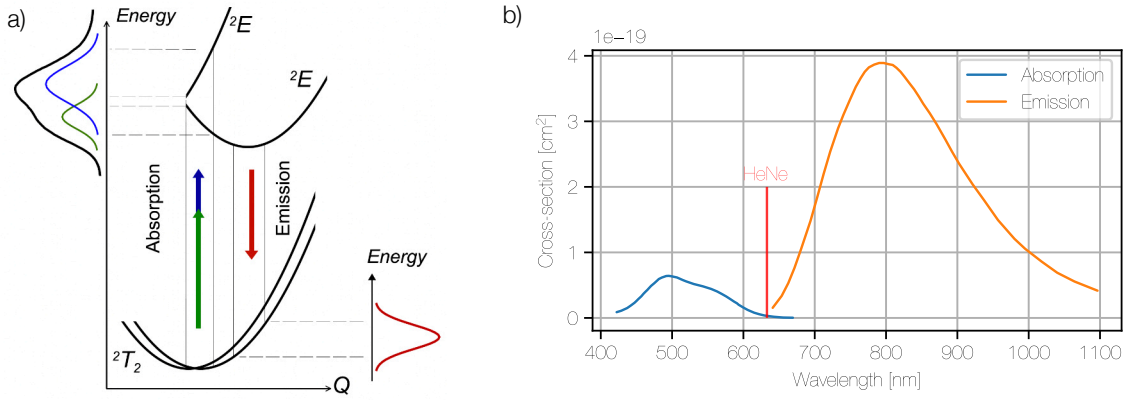

Figure 3.9 – a: Energy scheme of Ti:Sa the absorption (blue/green) and the emission (red) transitions are marked and the energy levels are sketched and named b: Spectrally dependent absorption and emission cross-section of Ti:Sa for π polarization [63]. The wavelength of Helium-Neon laser, 633 nm, is marked with a line.

3.4.3 Properties of Ti:Sa lasers

Titanium-doped Sapphire (Ti:Sa) as gain medium was discovered in 1982 by Moulton [62] and has since then become a standard for TW-laser systems with fs pulse duration. In the following, the specifics of Ti:Sa as laser gain medium will be discussed.

One key feature of Ti:Sa is its broad emission spectrum (see figure 3.9), which enables the amplification of sub-30 fs pulses. At the same time, crystals, large enough to amplify J-level pulses, can be manufactured. The high thermal conductivity is beneficial for efficient heat extraction [63], although its limits will be discussed later.
The energy scheme of Ti:Sa is shown in figure 3.9. Ti:Sa can be pumped with laser pulses in the wavelength range between 450 and 650 nm, with the highest absorption cross-section at 495 nm. The emission spectrum is centered around 800 nm, but spans from below 700 to above 1100 nm.

In figure 3.9 a rough energy scheme of Ti:Sa is shown. It can be described as four-level laser material. Absorption of photons within the absorption spectrum, excites electrons to state ^2E. From this state the electrons pass to level ^2E while the excess energy goes into vibronic excitations, which effectively heats the crystal.
The quantum defect in Ti:Sa for 527 nm pump light is 34 %. This means, that about a third of the pump laser power/energy are transformed into vibronic excitations in the crystal, effectively heating the crystal.

This chapter introduced the basic principles of laser-plasma acceleration, focusing on the laser parameters, that are required, to efficiently drive an LPA. A brief mathematical description of laser pulses is given, leading to the understanding of the spectral phase,

which is crucial, to understand the principle of CPA and the later design considerations. The effects of angular and spatial dispersion are briefly described. The basic principle of high-peak power laser systems, CPA, is explained in detail, to understand the later described pulse stretchers and compressors. Finally, the amplification in Ti:Sa lasers is detailed to introduce it as a gain medium for the later described amplifier.

4 A stretcher for the new OPCPA front-end of the ANGUS laser

The ANGUS laser is driving the Laser-Plasma-Accelerator (LPA) LUX, which is situated on DESY campus in Hamburg. It is a 100 TW peak power laser, based on Titanium-doped Sapphire (Ti:Sa) as gain medium and was originally designed as double chirped-pulse amplification (CPA) laser. It is a commercial laser system from THALES. A scheme of the laser system structure is given in figure 4.1 and will be briefly described, before the development of a new front-end is motivated.

In the original setup a Ti:Sapphire oscillator is seeding the system. The output pulses are stretched and then amplified in a regenerative amplifier, after which they are compressed again and sent through a cross-polarized wave generation (XPW), to improve the temporal contrast [64]. Afterwards they are stretched to 220 ps in an Oeffner stretcher and sent through an acousto optic dispersive filter (Dazzler, FASTLITE). The 2-pass Booster amplifier after the Dazzler provides around 100 µJ of output energy. After the Booster, the beam is passing a Pockels cell, which is used for pulse picking, to reduce the repetition rate from 1 kHz to 1 Hz. The entire section until the Pockels cell is the so-called kHz front-end.

Three multi-pass amplifiers amplify the pulses to their final energy of around 6 J. Afterwards, the beam can be attenuated with a tunable attenuator and the wavefront can be shaped by a deformable mirror. The final stage is the pulse compressor, which is a gold-grating based Treacy compressor, placed in vacuum, that compresses the pulses to sub-30 fs.

As it is already described in [34],[36] and [37] the front-end of the laser system has been drifting in several laser properties such as mean wavelength and spectral bandwidth. In addition, instabilities in the output spectrum of the XPW have been observed due to white-light generation and damage in its crystal. These drifts in the front-end propagated through the system and affected also the electron acceleration [30].

All of this motivated the development of a new kHz front-end, a white-light seeded optical-parametric chirped-pulse amplifier (OPCPA) called Malcolm. It should replace

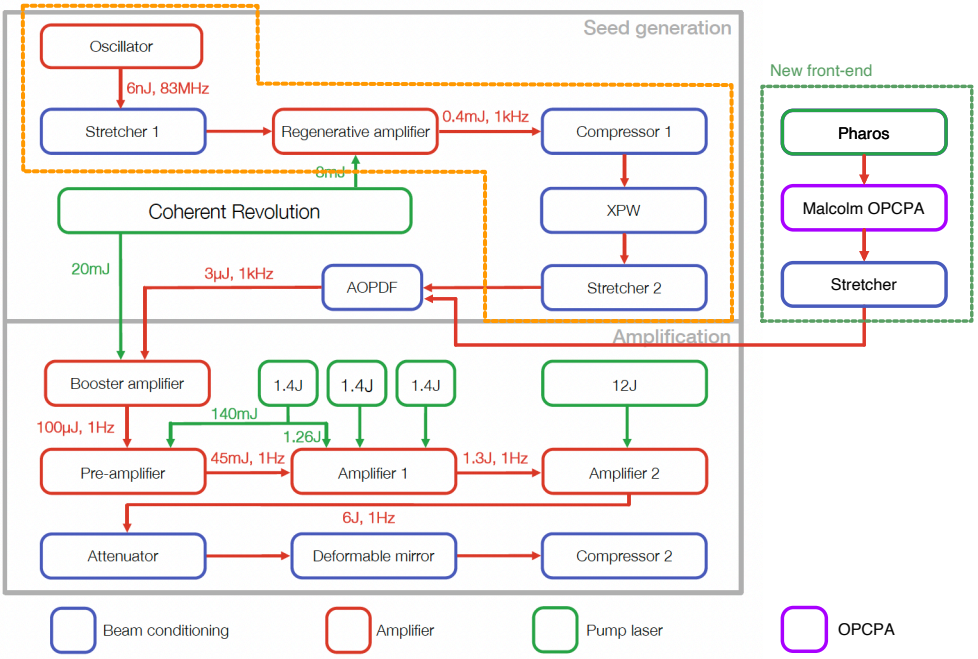

Figure 4.1 – Figure adapted from [36]. Overview of the ANGUS double-CPA laser system. The orange framed part is replaced by the new front-end.

the part of the front-end that is marked with the orange box in figure 4.1. The components of the new front-end are shown in the green box. An industrial Yb-doped laser (Pharos) drives the OPCPA system, that generates around 50 µJ laser pulses centered at 800 nm, providing a spectral bandwidth of 56 nm FWHM (25 fs FTL) [37] . These are stretched in the new stretcher, that is the topic of this chapter. The choice for an OPCPA in comparison to a 'classical' laser has been made based on the following benefits: Due to the parametric amplification and pumping with fs-scale pulses, the temporal contrast is much better than in 'classic' laser amplifiers. The parametric amplification does not require storage of energy inside the amplifier crystals, which strongly reduces the heat load in the whole setup and with that thermal drifts. The setup is driven by an industrial grade Yb-doped laser (Pharos, Lightcon) with a sub-percent long- and short-time energy stability. In the white-light generation a broad spectrum is generated, the 800 nm part of this spectrum is then is amplified in the OPA stages. A more thorough discussion on design and performance of Malcolm can be found in the PhD thesis of T. Eichner [36] and T. Hülsenbusch [37].

Part of the new front-end that should improve the laser stability was also the design and setup of a new stretcher. This was motivated by several reasons: One was to improve the mechanical stability in comparison to the old stretcher and allow repro-

ducible tunability of the opto-mechanics. Another was to include a diagnostic of beam position and pointing into and out of the stretcher, that allows to place the cameras outside of the stretcher housing, to avoid air fluctuations that are caused by heated cameras. Furthermore it facilitates the use of new optics, as the original ones started to degrade already. And it eases the incoupling of Malcolm into the stretcher and with that the integration into the existing laser system. In addition, the spectral phase of the stretcher could be directly adapted to the new total spectral phase, that changed because of the slightly stretched pulses from the OPCPA front-end. The calculation of the required stretcher spectral phase, to enable the compression of Fourier-limited pulses, will be part of the discussion in the next section.

In the following, the design of the optical layout and mechanical setup of the new stretcher will be described. The alignment of the stretcher is explained in greater detail. The characterization of the stretcher, its integration into the existing laser system and its performance in the final system will be presented.

4.1 Stretcher design

To ease the design process of the stretcher, it was decided to copy the optical design of the old stretcher as starting point. As shown in figure 4.2, the stretcher is a one-grating Oeffner stretcher, as it has been described in section 3.3.2. The grating is gold coated and has a line density of 1/g=1400 lines/mm. The focusing mirror (FM) has a radius of curvature of 1 m and the defocusing mirror (DFM) of 0.5 m. Spaced by 0.5 m, they form the imaging Oeffner telescope of the stretcher. A roof-mirror (RM) changes the beam height and sends the beam for the second pass through the stretcher.

The spectral phase of a one-grating Oeffner stretcher is determined by the grating line density, the radius of curvature of the focusing mirror, the grating distance and incidence angle. These parameters have to be chosen such, that the resulting spectral phase fulfills equation 3.12 (see: section 3.3.2). To find the optimal parameters, a matching of the stretcher phase to the system phase was performed. The phases of the following subsystems were considered in the calculation: the compressor, the Ti:Sa amplifiers and the Malcolm front-end. Their dominating phase terms GDD and TOD are given in table 4.1:

The compressor phase was calculated by ray-tracing several wavelengths through a compressor model in the commercial ray-tracing software OpticsStudio. The phase of Malcolm was measured with a FROG device (GECO, Lightcon). The contributions of the Ti:sapphire crystals were estimated with the Sellmeier equation of Ti:Sapphire and

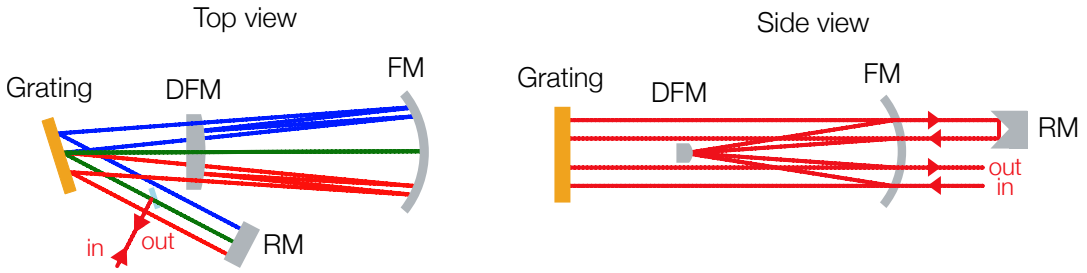

Figure 4.2 – Top and side view of the stretcher for the new ANGUS front-end. It is a one-gold-grating Oeffner stretcher. The beam is coupled in at the lowest beam height. It hits the grating for the first time, is angularly dispersed and passes the focusing mirror (FM) and defocusing mirror (DFM) of the Oeffner telescope, before hitting the grating again, where the angular dispersion is compensated. A roof-mirror introduces a height step and sends the beam through the stretcher a second time.

Subsystem	GDD [fs^2]	TOD [fs^3]
Compressor	-2178453	4370820
Malcolm	1313	-13302
Ti:Sapphire amplifiers	16831	12216
Total	-2160309	4369734

Table 4.1 – Overview of the estimated spectral phase contributions of the different subsystems in the ANGUS laser.

used to calculate the difference of optical pathlengths for the different wavelengths, from which the spectral phase could be calculated. The total path length through Ti:Sapphire in ANGUS is around 0.39 m.

[65] provides an analytical formula for calculating the phase of a one-grating Oeffner stretcher from the parameters grating distance, angle, grating line density and the focusing mirror radius of curvature. This was used for finding stretcher parameters that create a stretcher phase, which is the negative of the combined other phase contributions. The resulting parameters are listed in table 4.2.

In figure 4.3, the resulting phases are shown. The combined phase of compressor, Ti:Sapphire and Malcolm as well as the stretcher phase are plotted on the left. Both have almost the same shape and magnitude, but opposite signs. The residual phase, which is the sum of both phases is shown in yellow. Its amplitude is <50 rads, which is reasonably small and well within the tuning range of the Dazzler. In the right plot, the phase contributions of the Malcolm and the Ti:Sapphire are shown separately, to

Parameter	Value
grating line density (lines/mm)	1400
grating distance (mm)	246.63
angle of incidence (°)	43.3
Radius of curvature (m)	1.00
GDD (fs^2)	$2.05 \cdot 10^6$
TOD(fs^3)	$-4 \cdot 10^6$

Table 4.2 – Fitted parameters of the new stretcher

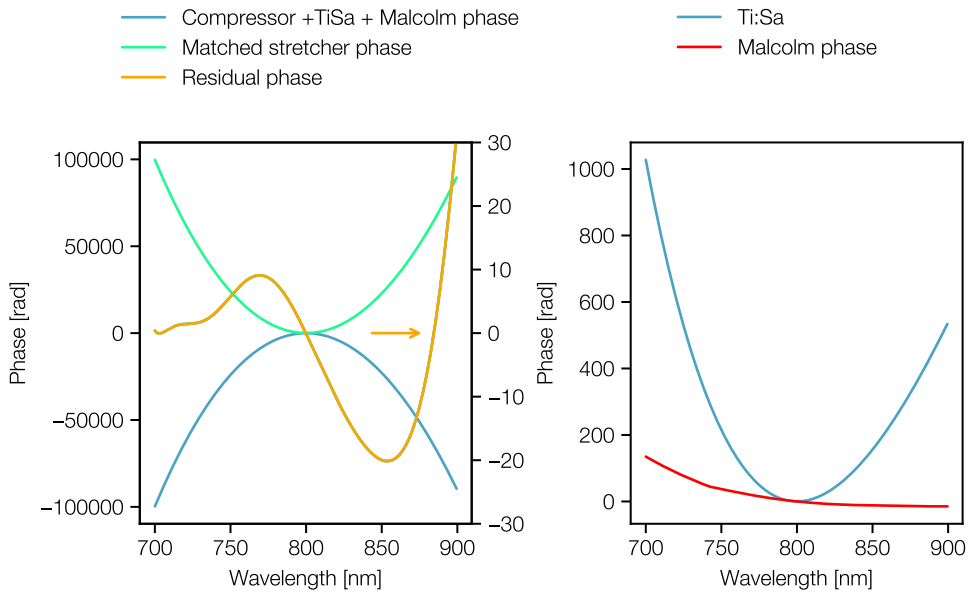

Figure 4.3 – Left: Spectral phases of the stretcher and the combined phase of compressor plus Ti:sapphire crystals plus the Malcolm phase. In addition, the sum of both phases (orange) is given, showing the residual phase of the system. Right: Spectral phase of Malcolm and the Ti:Sapphire crystals shown separately to give an impression of their magnitude.

make them visible. Their amplitude is $< 1\,\%$ of the stretcher or compressor phase. The Malcolm phase is actually the smallest contribution.

The phase matching resulted in the finding of the stretcher parameters. Apart from matching the compressor and system phase, the goal was also to improve the mechanical setup for more reproducible and precise tunability and mechanical stability. The old and the new stretcher setup are shown in figure 4.4.

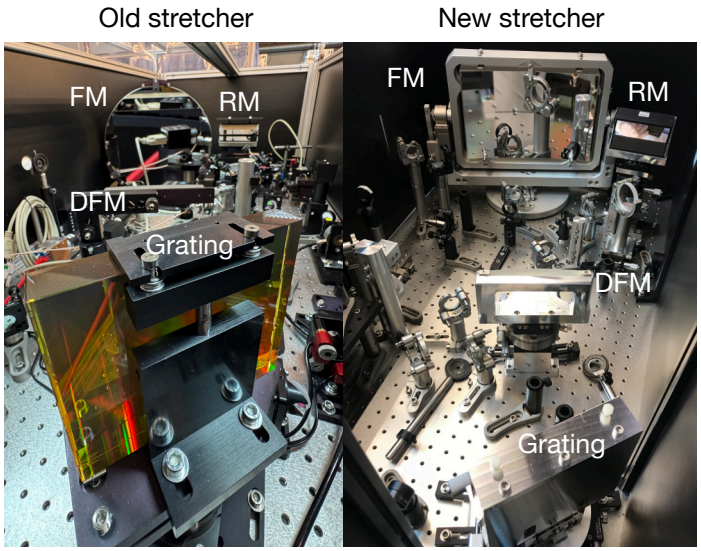

Figure 4.4 – Comparison of the old and new stretcher setup. The focusing mirrors (FM) can be seen in the back, next to the roof-mirror (RM), the defocusing mirror (DFM) sits in the middle and the gold grating in the front of the picture.

To improve the mechanical stability, compared to the previous stretcher, the following changes have been made: The focusing mirror (FM), which was round in the old stretcher, was cut to a rectangular shape to reduce its mass and footprint. This way, it was easier to mount the mirror more rigidly, due to the planar surfaces at the sides and its reduced weight. The final mount was developed in cooperation with Lioptec. It is clamping the mirror in a rigid frame from the sides and top. The frame can be adjusted in its tip and tilt angle.

The mount of the defocusing mirror (DFM) was changed to a mount with two instead of one bases, to make it more rigid. In addition, the mount itself is lower and to adjust the mirror, it is placed on a stack of stages. For the roof-mirror (RM), instead of two individual mirrors, that can move relative to each other, a monolithic hollow-roof prism mirror is used with high alignment tolerances. This and the grating are also mounted in almost monolithic mounts, placed on stage stacks for precise and reproducible alignment. All stages can be locked by locking screws and adjusted with µrad precision. After finding matching stretcher parameters and the optical and mechanical design, the stretcher has to be aligned, which will be described in the following.

4.2 Stretcher alignment

The alignment of stretcher and compressor need special care. This is because the beam is split spectrally in space and angle inside the setup and all spectral components have to combine in the same position and with the same angle after the setup. If this is not the case, the resulting angular and spatial chirp can cause a variety of undesired effects: In the amplifiers, it can lead to a coupling between output spectrum and spatial overlap with the pump beam, which can have negative effects on the laser performance such as spectral drifts or a narrower bandwidth. In the focus, it can reduce the intensity due to the chromatic spatial distribution of the focus, which also leads to a longer effective pulse length [66]. In addition, angular chirp leads to a pulse-front tilt of the beam, which can introduce a kick to the electrons during acceleration [67],[68]. Thus, the compressor and stretcher should be aligned such, that the angular and spatial chirp are minimal.
In the following, first the general alignment of the telescope optics is explained, the minimization of the angular and spatial chirp is discussed afterwards.

4.2.1 General alignment

The first alignment of the optical components included the following steps, which are depicted in figure 4.5 1.-4.

1. Alignment of the tip and tilt angle of the grating: The beam was aligned on a defined input axis with two pinholes at the central height of the stretcher. The grating was placed perpendicular to the beam. The tip and tilt of the grating were adjusted until the beam was back-reflected through both pinholes. This position was noted as zero position on the rotation stage and used as reference to adjust and define the grating incidence angle later.

2. Alignment of the tip and tilt angle of the focusing mirror: The grating was rotated to half the angle between input axis and central axis of the stretcher and the specular reflection was sent onto the focusing mirror. The focusing mirror tip and tilt angle were adjusted until the beam was reflected back through the pinholes on the input axis.

3a. Alignment of the position, tip and tilt angle of the defocusing mirror: The input beam height was changed to a higher beam height, but the input axis remained parallel to the previous one. The pinholes on the input axis were then set to the second, lower beam height, but the same distance to the central plane as the higher axis. The beam is sent over the grating and onto the aligned focusing mirror. As the

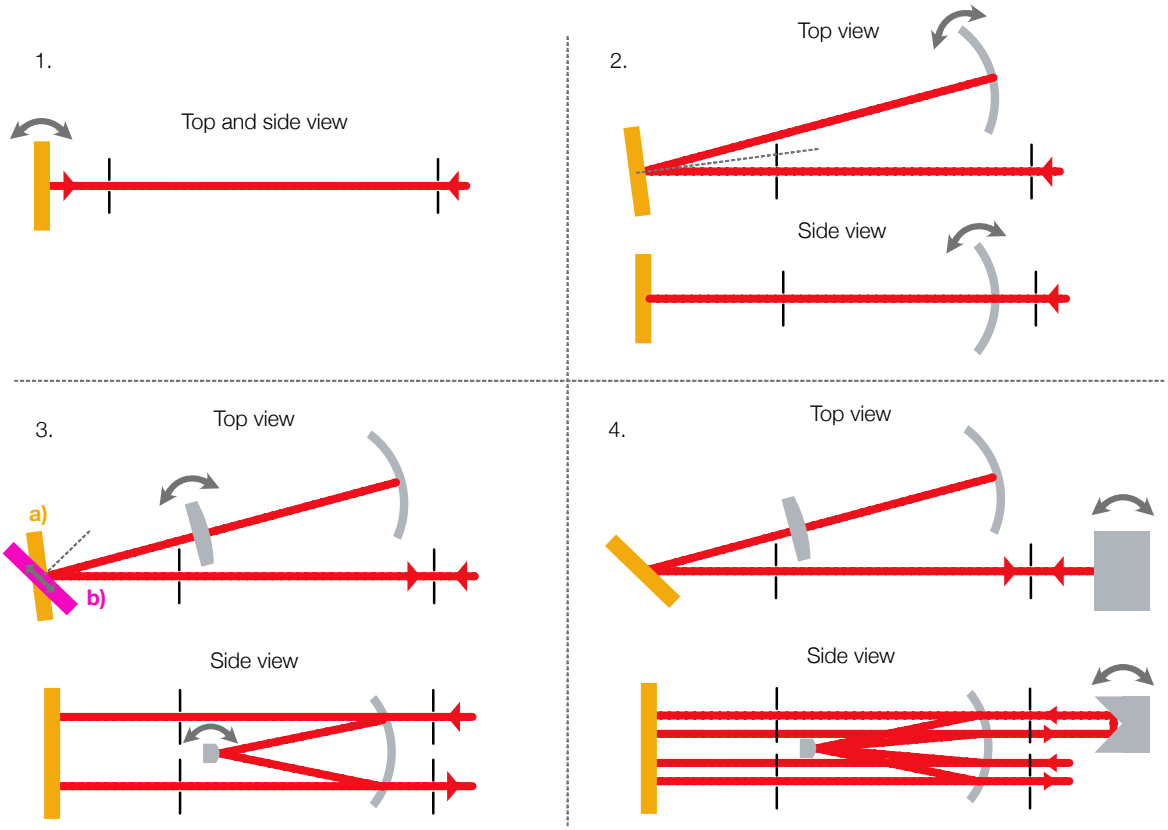

Figure 4.5 – Visualization of the stretcher alignment method. Depicted are the gold grating, the in- and outgoing beam and the stretcher telescope optics, the focussing and defocussing mirror as well as the roof-mirror.

beam is vertically off-centered on the focusing mirror, it is reflected downwards, onto the defocusing mirror and further onto the focusing mirror again. The defocusing mirror tip and tilt angle were adjusted until the beam went through the lower pinholes on the input axis. The longitudinal position of the defocusing mirror is tuned until the output beam is collimated. This can be checked e.g. with a shearing interferometer.

3b. Alignment of the grating in-plane-rotation: The grating is rotated to its design angle, using the previously found zero position as reference. The in-plane rotation is adjusted until the beam aligns with the pinholes parallel to the input axis.

5. Alignment of the roof-mirror: In the last step, the input beam height is changed to the second lowest height and the roof-mirror is placed after the first pass through the stretcher. Its tip and tilt are then aligned such, that the beam exits again on the

output axis at the lowest beam height.

Even after aligning the stretcher to its design angles and layout with the previously described method, it is likely, that the output beam is angularly and spatially chirped. To reduce the chirp as much as possible another, wavelength sensitive alignment has to be performed. This is presented in the following.

4.2.2 Angular chirp optimization with a three-color-laser

To judge if the used methods are sufficient to measure the angular chirp, the maximum acceptable angular chirp should be estimated first. Several effects have to be considered, at the final experiment and in the amplifier that follows the stretcher. At the final experiment angular chirp has mainly two effects: Firstly the spatial separation of the wavelengths in the focus reduces the local bandwidth, which increases the Fourier-transform limited pulse length. So effectively, the pulse duration increases. The angular chirp, that is required to increase the pulse duration by 1 % at the LUX experiment is 0.15 µrad/nm, using equation (19) from [66]. The second effect is the pulse front-tilt, which causes a pointing in the electrons. From a measurement of the electron pointing in dependence of the angular chirp in [68], the pointing becomes significant for angular chirps >0.5 µrad/nm. Both these effects are mainly relevant for the beam after the compressor. Assuming the angular chirp remains unchanged by the amplifiers, it is however strongly reduced between stretcher and compressor, due to the increase in beam size. The beam size is increased from 2-3 mm to 60 mm, which is a magnification of 20-30, which reduces the required precision of the angular chirp by the same amount.
Angular and spatial chirp also affect the amplifier performance between stretcher and compressor. Again two main effects need to be considered: The first is spatial chirp inside amplifier crystals. As mentioned earlier, spectral splitting of the beam in the crystal leads to coupling of the output spectrum with overlap of the beam and eventually narrowing of the amplified spectrum. In the ANGUS laser system the next amplifier is the Booster amplifier. The beam is focused into the crystal with a f=600 mm lens and the beam size in the crystal is around 500 µm. An angular chirp of 0.4 µrad/nm would cause a splitting of 25 µm for a 100 nm spectrum, which would be 5 % of the beam diameter, which can be deemed acceptable.
The second effect is, that the spatial chirp should not become too large along the transport, especially on spherical optics, where spherical spectral aberrations would be acquired. To estimate a limit here, the path until the next amplifier is considered, which is around 2.5 m. To again stay below 5 % of the beam diameter, the angular chirp would need to be below 0.4 µrad/nm for 100 nm bandwidth.
Concluding it can be said, that after the stretcher an angular chirp of <0.4 µrad/nm

should be acceptable. After the compressor, the limit should be smaller to prevent the increase in pulse duration.

Several methods have been developed to measure and minimize the angular chirp of stretchers and compressors [66], [69], [70], [71], and a few will briefly be presented here:

- Imaging spectrometer: An imaging spectrometer can resolve the spectral distribution for points along one transversal axis of the beam. This way the relation between position in the beam and wavelength can be detected. It can also be used in the focus, to measure the angular chirp. The measurement is usually limited to one axis at the time. The minimal resolvable angular chirp depends on the resolution of the used detector chip and the bandwidth of the laser. Exemplary, the commercial imaging spectrometer (MISS, Femtoeasy), used for a 50 nm bandwidth, that is focused over 1 m can measure angular chirps of 0.1 µrad/nm. The later discussion on possible measurement errors will partially be valid for this measurement technique as well.
- Pulse front tilt measurement [66]: As mentioned in chapter 3, angular chirp causes pulse front tilt. Measuring the pulse front tilt with an inverted field autocorrelator can be used to calculate the angular chirp as well. The precision of this measurement was estimated to 0.1 µrad/nm [71].
- Position and pointing measurement of individual colors [69], [70],[71]: Selecting individual colors within the spectrum of the used laser in principle allows to measure spatial and angular chirp in both directions simultaneously and directly by measuring the position or the (focus) position of the individual wavelengths with a camera. The wavelengths can be selected e.g. with a Fabry-Perot-Interferometer [69] or by combining the output of fiber-coupled laser diodes as it was done in the setup presented in the following. With this measurement method a precision of <0.005 µrad/nm has been achieved [71]. In [69] and [70] precision of 0.1 and 0.02 µrad/nm have been obtained. The precision of the presented setup will be discussed in subsection 4.2.2.

The method we used for stretcher and compressor angular and spatial chirp optimization, was presented by D. Papadopoulos in [71] and a schematic drawing is shown in figure 4.6. Light of three different wavelengths within the target spectrum of the characterized setup is coupled into one polarization maintaining single-mode fiber and collimated at the fiber output. This way, all three wavelengths overlap well in space and angle. This three-color-laser is then sent through the dispersive setup, in this case a stretcher, where they experience different beam paths and are recombined again. The angular and spatial chirp that the setup introduces can now be measured by measuring the angular and spatial chirp of the three-color-laser. The spatial chirp

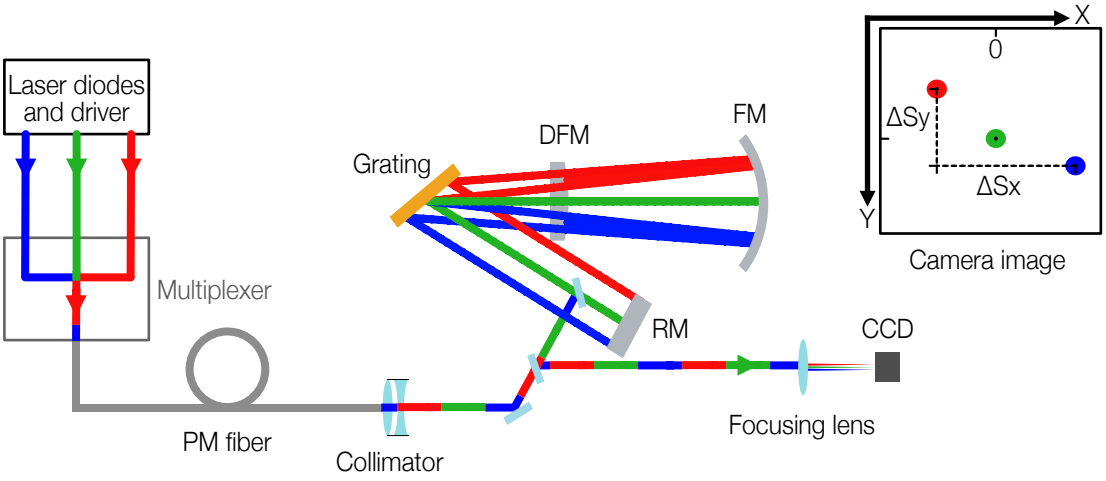

Figure 4.6 – Principle of the 3-color-laser alignment method: The three colors are combined in a fiber, collimated and sent through the stretcher. The beams are focused on a camera and relative positions are determined.

can be measured with a camera, which is placed directly in the beam, and the beam positions of the three colors can be measured individually to determine the spatial chirp in both axes. To measure the angular chirp, a camera can be placed in the focus of an achromatic lens and the transverse focus positions s'$_{x,y,\lambda}$ of the three colors can be measured. In the following this angular chirp measurement method will be described in more detail.

According to the 2x2 matrix formalism, the lateral position of each wavelength λ $s'_{x,y,\lambda}$ after a focusing lens of focal length f and a propagation distance d depends on its angle ϕ_λ and on the initial beam position $s_{x,y,\lambda}$ as described in equation 4.1:

$$s'_{x,y,\lambda} = d \cdot \phi_{x,y,\lambda} + s_{x,y,\lambda} - \frac{d \cdot s_{x,y,\lambda}}{f} \tag{4.1}$$

To use s'$_\lambda$ to measure ϕ_λ, it is advantageous to measure it in the focal plane where f=d and equation 4.1 reduces to

$$\phi_{x,y,\lambda} = f^{-1} \cdot s'_{x,y,\lambda}. \tag{4.2}$$

The angular chirp in horizontal and vertical direction $\frac{\delta\phi_{x,y}}{\delta\lambda}$ can then be calculated with

$$\frac{\delta\phi_{x,y}}{\delta\lambda} = f^{-1} \cdot \delta s_{x,y}/\delta\lambda. \tag{4.3}$$

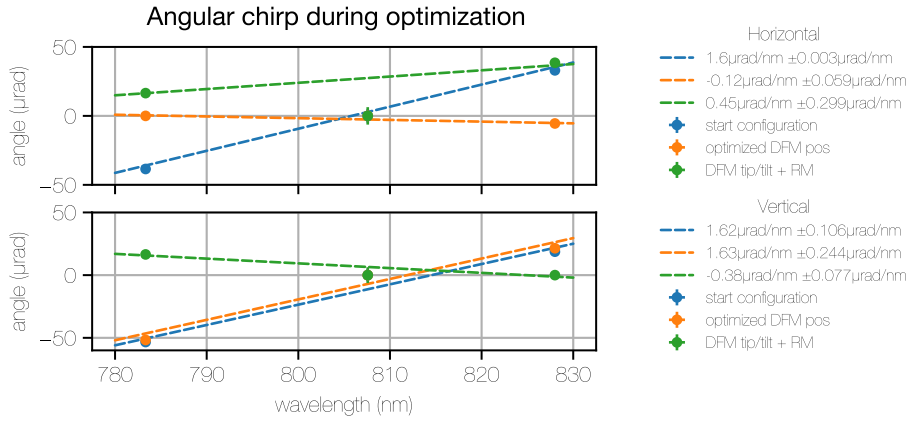

Figure 4.7 – Measurement of the angular chirp before and after optimizing the DFM position, the DFM tip and the roof-mirror alignment. The angles of the central wavelength (806 nm) are all set to zero and overlap in the plot.

During the measurements, mainly the linear chirp $\frac{\Delta\phi_{x,y}}{\Delta\lambda}$ was analyzed as it was the dominant term in almost all cases. And it was the main goal to minimize the linear chirp. Quadratic chirp was present mainly when the chirp was already close to the minimum. Possible sources for it will be discussed later.
The beam positions on the camera were measured and averaged over 1 minute. The angles were calculated with equation 4.2 and the angular chirp was deduced as slope of the linear fit of the positions of the wavelength as it is shown in figure 4.7.

It shows the angle measurement of the three colors after the stretcher during one optimization step of the angular chirp. The horizontal chirp is displayed in the top, the vertical in the bottom plot. The blue dots show the initial positions of the colors. First, the longitudinal position of the defocusing mirror was tuned, to minimize the horizontal chirp. The resulting beam positions are shown by the orange dots. Afterwards the tip angle of the defocusing mirror and the roof-mirror alignment were optimized again, to minimize the vertical chirp and to bring the beams back onto the output alignment marks. The final state of this optimization step is shown by the green dots. The angular chirp of every configuration is then approximated by the slope of the linear fit of the three focus positions. The angle of the central wavelength is set to 0 for all configurations as only the relative angles are important to determine the angular chirp.

In the third state, it is clearly visible, that the chirp is not purely linear. The quadratic chirp can have several sources. One is the combination of spatial chirp at the lens position and a misalignment of the focusing lens. Both a tilt or a lateral misalignment would lead to a change in longitudinal focus positions for the spatially dispersed colors. When the focus lies behind or before the focus of the center wavelength, the measured

lateral position is not only depending on the angle, but on the lateral beam position at the lens as well.
Another reason for quadratic chirp can be an overcompensation of the chirp, that is inherent to the setup. In the case of the one-grating Oeffner stretcher an angular chirp of 2 µrad/nm is expected with the parameters of the presented setup. As this is higher than the limits, that were discussed above, a compensation of it was tried. From ray-tracing simulations in OpticsStudio it becomes clear, that the movement of the defocusing mirror, to compensate this chirp leads to quadratic chirp in the end.
In addition, small quadratic chirp can also be caused by imperfect optics. If the optics surface deviates from its ideal shape, due to the spatial chirp on most of the optics, an additional angle would be introduced to some wavelengths.

Discussion of error sources

After introducing the measurement setup and principle and showing an exemplary optimization process, possible error sources of this alignment method will be estimated and discussed. The error sources can be divided into two types: Errors from the measurement of the angle of the individual wavelengths and additional sources of angular chirp being introduced into the beam by the measurement setup. The errors of the angle measurement will be discussed first and afterwards the errors introduced by the measurement setup and how to avoid them will be described.

Using the law of error propagation and equation 4.1, assuming d=f, the error of the angle measurement can be calculated by:

$$\begin{aligned} \sigma_{\phi_\lambda} &= -\frac{s'}{f^2} \cdot \sigma_d + \frac{\sigma_{s'}}{f} \\ &= (\phi_\lambda[\mu rad] \cdot \frac{\sigma_d}{f}) + \frac{\sigma_{s'}}{f} \end{aligned} \tag{4.4}$$

This means the measurement error of ϕ_λ depends on the one hand on precision of the distance between the lens and the camera chip d and on the other hand on the precision of the positional measurement, which will be discussed in the following.

From equation 4.4 it becomes clear, that close to the point of minimal angular chirp, where ϕ is already small, the error is dominated by the second part of the expression. It can in principle be reduced by using a large focal length focusing lens. However, a larger f increases the focus size, which makes the calculation of the beam position less precise. In addition, a longer propagation length means more propagation through eventually fluctuating air that potentially increases the position jitter $\sigma_{s'_\lambda}$. Thus a good pointing stability improves the precision of the measurement. If the beam pointing

Parameter	Estimated error σ
d	5 mm
s'	standard deviation of position measurement 0.12-0.9 px (1 px=5.5 µm)

Table 4.3 – Overview of error sources for the color dependent angle measurements.

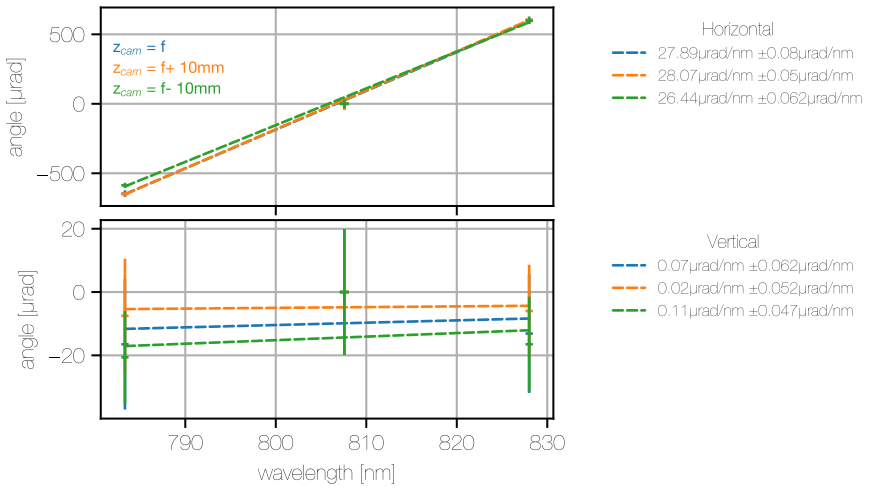

Figure 4.8 – Measurement of angular chirp with different longitudinal camera positions. All error bars are multiplied with 10, for better visibility.

jitter is below one pixel, the use of a camera with a smaller pixel size can the precision of the measurement. Averaging over more data points might increase the precision despite a larger jitter.

The other error source in the measurement of the angle of the individual wavelengths is the longitudinal position of the camera d. Only if f=d equation 4.2 is valid and only the angle of the beam determines the lateral position s'. The error, that is introduced, is proportional to the measured angle and to the precision of the camera positioning relative to the focal length.

To illustrate the effect of these two errors the angular chirp in horizontal and vertical direction was measured for three longitudinal camera positions, at the focus and 10 mm before and after the focus, which is 1 % change of d. According to equation 4.4 the expected change of the angular chirp would be 1 % of the initial value. The results are plotted in figure 4.8.

In the measured beam, the horizontal chirp (top) was relatively large, while the vertical chirp (bottom) was small, already in the range of its error. The error bars of the individual measurement points are only based on the $\sigma_{s'_\lambda}$ of the measurement. The

errors of the linear fits are calculated from the covariance matrix of the linear fit, which was weighted with $1/\sigma_{s'_\lambda}$.

A change of the measured angular chirp with the change of the longitudinal camera position can be observed in both axes. As expected, the changes due to the camera shift are larger in the horizontal, where the angles are larger. The change of the measured angular chirp for 10 mm is close to the expected 1 % of the initial angular chirp in one direction, but much larger in minus direction, which can be caused by additional spatial chirp at the lens as will be discussed later. In the vertical the changes due to the longitudinal camera position change seem to be larger than the expected 1 % of the initial angular chirp. The change is however in the range of the error from the position measurement. As mentioned before, additional spatial chirp in the beam at the lens position affects the spatial distribution of the colors around the focus and thus the angular chirp around the focus.

In principle, the camera can also be angularly misaligned. However, to obtain an error of the relative beam positions of 1 %, the angle misalignment needs to be >8 °. This is larger, than the alignment precision of the camera angle, so this effect is negligible.
In all previous considerations the error of the wavelengths were neglected. The standard deviation of the mean wavelength was measured to be <0.05 nm, which is 0.1 % of the total wavelength range and thus should be negligible as well.

Concluding it can be said, that the main errors for the focus position measurement are the position jitter during the measurement and the precision of the longitudinal position of the camera. The magnitude of the first is in the range <0.1 µrad/nm, the second is around 0.5 % of the measured angular chirp. In the following, possible sources of additional angular chirp in the measurement setup will be discussed.

- The fiber collimator: In general, fibers without angled tip (FC-PC) should be used for this measurement method, as angled fiber ends (FC-APC) introduce a larger angular chirp. Still, we found that the angular chirp after the fiber collimator was around 0.28 µrad/nm in one specific axis. Assuming, the fiber does not introduce angular chirp, this could possibly origin in alignment errors of the internal optics or a tilt of the fiber end inside the collimator. This systematic error on the measurement can however be avoided if the axis in which the angular chirp is present is aligned into x or y direction, such that the other direction does not see the angular chirp. In addition, in the case of the stretcher and compressor, the angular chirp measurement can be performed as relative measurement, by optimizing the angular chirp, until it equals the chirp of the collimator. The direction of the chirp and how it propagates through the system has to be taken into account in this method. Comparing the measurement result from this method to a measurement result obtained with another method or device can be another solution.

- Lens alignment: The positional and angular alignment of the focusing lens needs to be done carefully. A tilt of the lens changes its effective focal length and causes astigmatism in the beam, which complicates the definition of the focal plane. A lateral misalignment of the lens introduces additional angular chirp to the beam as the lens than acts like a wedge in the beam. To estimate this error, the beam was intentionally horizontally displaced on the lens for 2.5 mm in both directions and the change in angular chirp was measured. Figure 4.9 shows the results of the scan. The horizontal chirp changed for around 0.1 µrad/nm. Assuming a linear correlation, the alignment of the lens center to the beam has to be performed with a precision of <0.7 mm to reduce the error to the level of the positional measurement error.

- Spatial chirp: In theory a spatial chirp in the beam should not influence the angular chirp measurement as the lateral beam position in the focus only depends on the beam angle. Special care has to be taken in the following cases: First, if the spatial chirp is very large and the beam spreads out over the lens, spherical aberrations start playing a role and an additional angular chirp can be introduced. In this case for example a ray-tracing simulation can be performed to estimate the error.
  Second, if the camera is not perfectly placed in the focal plane and the beam is spatially chirped, the angular chirp measurement is influenced as well. As the spatial chirp can only be ignored in the focus plane, before or after the focal plane the spatial chirp is present and influences the position measurement of the individual wavelength.
  If spatial chirp is present at the lens it also increases the requirements on precision of the alignment of the lens. A tilt will then for example lead to different focal planes of the different colors. In general, spatial and angular chirp should be optimized in parallel.

Summarizing the error estimation it can be stated, that the alignment of the focusing lens and the camera has to be done precisely. For perfect alignment and especially for small angular chirps, the error seems to be dominated by the pointing stability of the three-color laser after the setup. In the performed measurements it was in the range between 0.03 and 0.1 µrad/nm, which is sufficient to resolve the maximum acceptable chirp after the stretcher. It is comparable to the other presented angular chirp measurement methods.

To further improve the presented method, several measures are possible. The position and pointing stability of the laser and the measurement can be improved. At least in the middle wavelength the jitter was partially caused by intensity fluctuations of the fiber output, that were probably caused by polarization fluctuations in the diode. This could easily be improved with a better engineered design. In addition, a longer focal length of the focusing lens for the angular chirp measurement could be tested, to

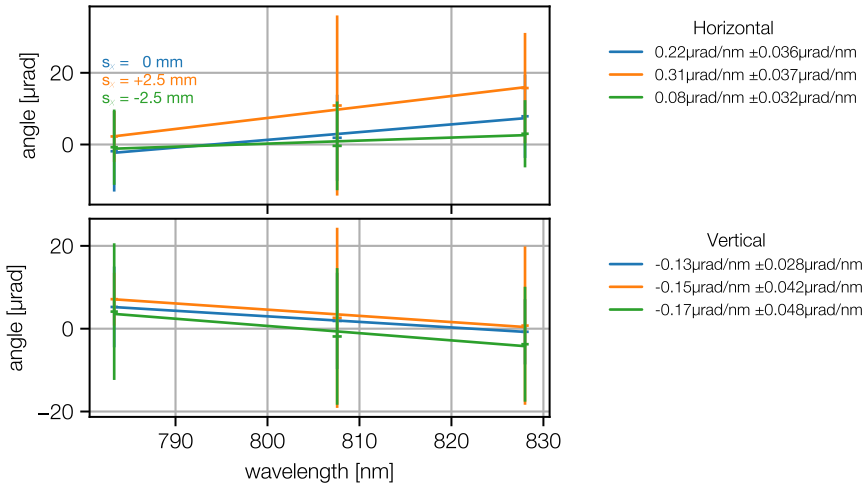

Figure 4.9 – Measurement of angular chirp with different transverse beam positions s_x on the lens. All error bars are multiplied with 10 for better visibility.

increase the resolution. Using more than three colors might help to better understand the chirp and its origins, especially when it is non-linear.

To compare the results of the camera measurements an imaging spectrometer was used. The result is depicted in figure 4.10. The left measurement is taken in the horizontal direction, the right in the vertical. For the evaluation, the center of gravity position was calculated for each wavelength. The resulting positions are represented by the blue dots. To calculate the angular chirp, a linear fit (green line) was applied to these points. Its slope gives the angular chirp. The resulting chirp was -0.4 and 0.5 µrad/nm, respectively. According to the previously performed estimations this is just acceptable for the performance in the later systems.

4.3 Characterization of the MALCOLM stretcher

4.3.1 Pulse duration measurement

After discussing the alignment of the stretcher and its challenges, the characterization of the stretcher is presented next. It was performed to check if the stretcher output is according to the desired specifications. All measurements were performed using the output beam of the demonstration setup of the later OPCPA front-end, Malcolm, as input laser. The input pulses have a pulse energy of around 50 µJ, and are slightly chirped to around 120 fs. Their spectrum has a mean wavelength of 799 nm and a bandwidth of 54 nm FWHM as it can be seen, in figure 4.14 on page 60, which will be discussed in detail later.

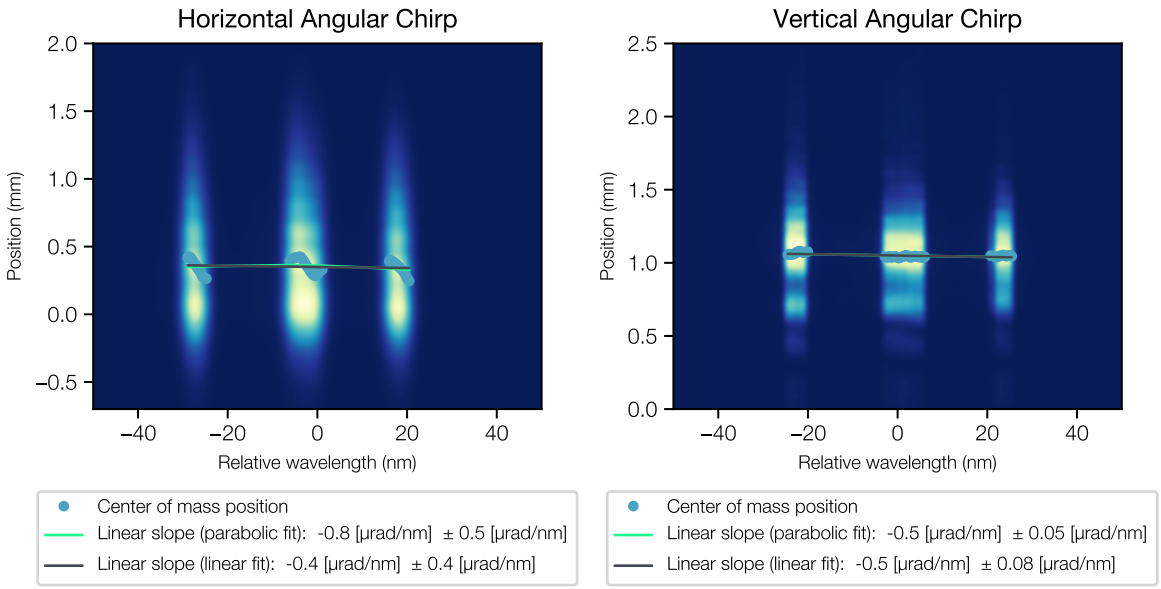

Figure 4.10 – Measurement of the angular chirp in the horizontal (left) and vertical (right), using an imaging spectrometer. The angular chirp is deduced as slope of the linear fit and the linear part of a parabolic fit.

To check the stretcher matching procedure and phase calculation was performed correctly, the stretched output pulse length was measured for several grating distances with a long-range autocorrelator (PulseCheck, APE). The result is shown in figure 4.11. For the grating distance at the center of the stage, which equals the design separation, the measured stretched pulse length is around 270 ps. The pulse length changes with the position of the grating at a rate of 1.56 ps/mm.

To check if the measured pulse lengths match our expectations, the spectral phase, that we retrieved from the ray-tracing in Optics Studio, and the measured output spectrum of the stretcher were used to calculate a theoretical pulse duration. This procedure is sketched in figure 4.12. The input spectrum and spectral phase for the central grating position are displayed in the left plot. A Fourier transformation is performed, to retrieve the temporal shape of the pulse intensity $I(t)=E^2(t)$ after the stretcher, which is plotted in the middle plot. The resulting theoretical pulse length is 312 ps for the central grating position, which is about 40 ps longer, than the measured pulse duration.

To understand this result, the measurement procedure was simulated as well for the previously calculated temporal pulse shapes I(t). The measurement device performs an intensity autocorrelation, which was calculated for I(t) and is plotted in the right plot of figure 4.12. The measurement device then applies a Gaussian fit to this autocorrelation trace (orange), takes the FWHM of the Gaussian fit and divides it by 1.41 to retrieve

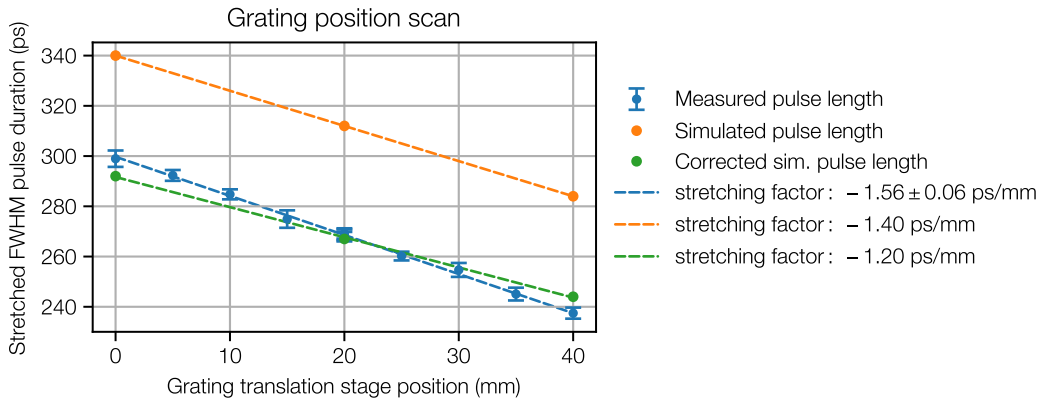

Figure 4.11 – Output pulse length of the stretched pulse for different grating distances. The pulse length was measured with an APE long-range autocorrelator. The simulated results were retrieved from a ray-tracing model of the stretcher in combination with the measured output spectrum, auto-correlation and a Gaussian fit.

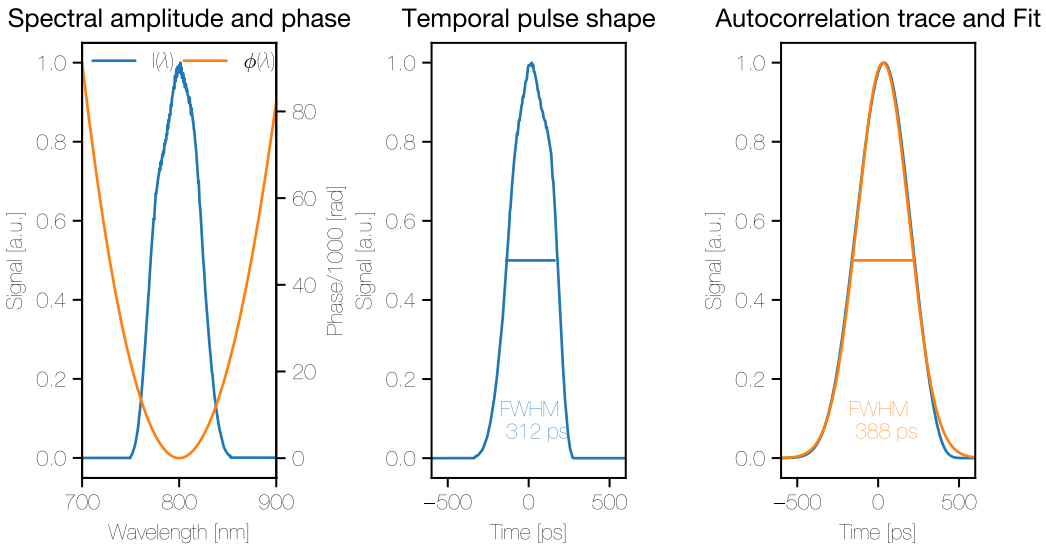

Figure 4.12 – Calculation of the expected pulse length from the spectral phase and amplitude (left) via Fourier-transformation. The resulting temporal intensity (middle) has a FWHM of 312 ps. The measured pulse length can be understood, when the autocorrelation trace and its Gaussian fit (right) are calculated, as the resulting $\mathrm{FWHM}_{AC}/1.41$ equals the measured pulse length of 275 ps.

the pulse length, as it would be correct for Gaussian input pulses.
Performing the same operation on the simulated autocorrelation trace, results in a autocorrelation trace width of 388 ps which, divided by 1.41, results in a pulse length of 275 ps. This matches the measured pulse length within the measurement uncertainty. The same procedure was performed for the largest and smallest measured grating separation. The results of the virtual scan are plotted next to the measurement results in figure 4.11. The pulse length, that is calculated from the spectral phase and amplitude is represented by the orange data points. The slope is -1.40 ps/mm. The pulse lengths, that are then retrieved via autocorrelation and fitting are represented by the green data points. The slope is -1.20 ps/nm, which is lower, than the measured slope. A possible explanation is a slight change of alignment due to the grating distance change, which is inherent to the one-grating Oeffner layout, and could change the efficiency of the auto-correlation process. Another cause could be a change of the spectrum during the scan, which would lead to different pulse lengths as well. For the simulated pulse lengths the same spectrum was used for all grating separations.

It can be concluded, that the calculation of the spectral phase was correctly done and the stretcher performs as expected. However it needs to be taken care, that the measured pulse duration can strongly differ from the real one, especially if the spectrum is not of Gaussian shape, due to the measurement technique of intensity auto-correlation and fit procedure. The design grating distance for the used spectrum, yields a pulse length of 312 ps FWHM. The difference to the pulse length from the old stretcher (220 ps) can be explained due to a much larger spectral width of the Malcolm spectrum, which leads to a longer stretcher pulse length.

The change in pulse length is linear with the grating distance, as expected. During the measurement, the positioning of the stage was reproducible. The center position was measured both, before and after the scan and the results match well. This promises an easily tunable grating separation, to match the compressor grating separation.

4.3.2 M^2 measurement

After the confirmation of the correct output pulse duration, the beam quality of the output was measured as well. The beam quality factor M^2 gives a measure of how close the intensity propagation is to that of a Gaussian beam [72]. As the beams in the front-end are meant to be close to Gaussian, the output beam quality of the stretcher was measured. The measurement was performed with a commercial M^2 measurement device (BeamSquared, Ophir), which focuses the beam and measures the second moment beam size through the caustic. To see the effect of the stretcher, the M^2 was measured before and after the stretcher.

As mentioned before, a non-ideal stretcher alignment can cause angular chirp, which could worsen the M^2. In that case, the M^2 of the beam with the whole spectrum would

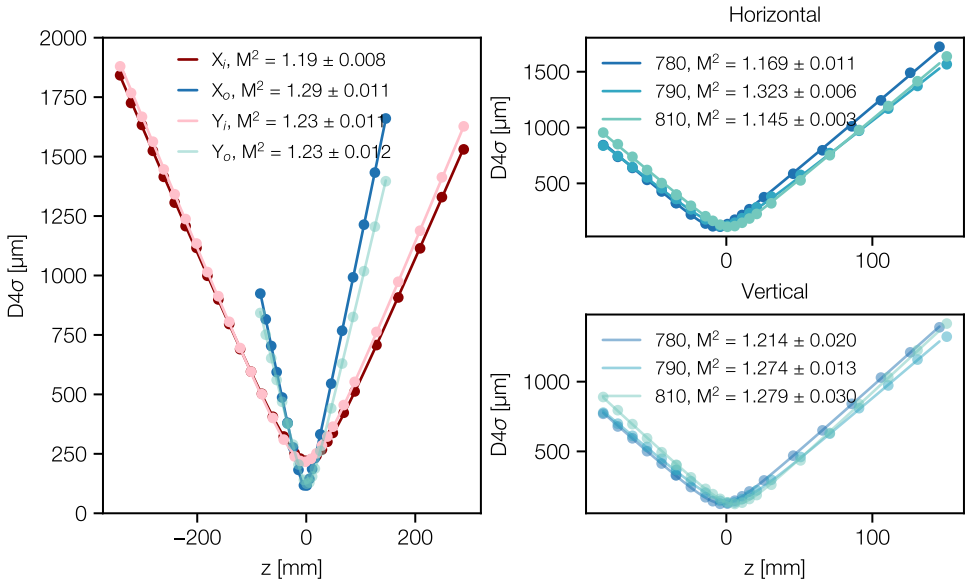

Figure 4.13 – Beam caustic after the stretcher, measured with a commercial M^2 measurement device (BeamSquared, Ophir). The input beam was measured for comparison (left plot, red), the output beam was measured as a whole and using spectral bandpass filters (right plots), to learn about the chromaticity of the caustic. The errors are derived from the covariance matrix of the fit.

have a higher M^2, than individual colors. To test this, the beam was filtered with band pass filters at three wavelengths within the spectrum and the M^2 was measured for all three cases. The results of all measurements are plotted in figure 4.13.

In the measurement of the full spectrum all M^2 values are < 1.3, which means the beams are close to Gaussian, as they were specified. In comparison to the M^2 of the input beam, which is 1.19 and 1.23 , in the horizontal and vertical axis, the M^2 after the stretcher is slightly increased (1.29) in the horizontal, but stays constant in the vertical.
Several factors can lead to an increase in M^2. One is the mentioned angular chirp. In this case, the M^2 of the individual wavelengths would all be smaller, than the total M^2. This is not the case, while 780 nm and 810 nm have indeed a smaller M^2, the M^2 of 790 nm is larger.

A worsening of the beam quality can be caused by surface errors in the optics as well. As it seems that the M2 worsened more in the 790 nm beam, than in the other spectral ranges, the optics, on which the beam is spatially dispersed should be considered. These are the grating, the focusing and defocusing mirror and the roof-mirror. Surface errors on all of them could contribute to a worsening of M^2 in a specific spectral range. The beam quality is however more than sufficient for our application and the beam is suitable to seed the following amplifiers.

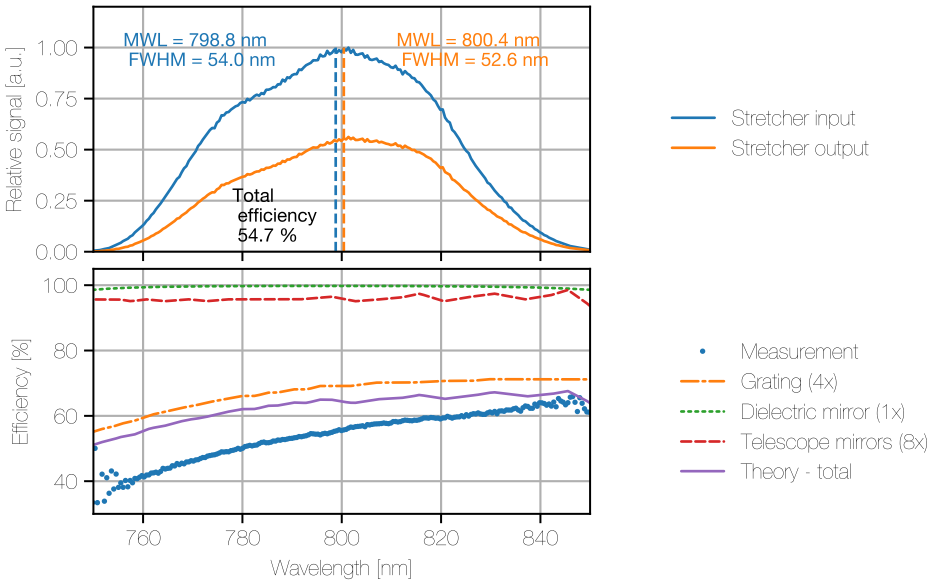

Figure 4.14 – Spectral efficiency of the MALCOLM stretcher. The measured efficiency as well as theoretical efficiencies of the components and of the total stretcher are displayed.

4.3.3 Spectral efficiency

Grating stretchers are often the source of tens of percents of energy losses. To judge the expected output energy and a possible change in spectrum, the input and output spectrum were measured and are shown in the top plot of figure 4.14. The overall efficiency is $\eta_{stretcher}$=54.7 %. The mean wavelength is red-shifted slightly by 1.6 nm and the FWHM of the spectrum is reduced by 1.4 nm, which corresponds to 2 % of the spectral bandwidth.

From the input and output spectrum, the spectral efficiency was determined and is shown as blue curve in the bottom panel of figure 4.14. The efficiency of the stretcher is sloped, longer wavelengths have a higher transmission than shorter wavelengths. To understand the contribution of the individual stretcher components to the overall efficiency, their individual efficiencies as they were provided by their manufacturers, are displayed as well. Their combined efficiency is shown in the violet curve. The highest losses are expectedly caused by the gold grating, which is also responsible for the slope of the efficiency. The second highest losses are due to the protected silver mirrors of the Oeffner telescope. Even if their efficiency is high, they are hit eight times in the stretcher, which results in around 5 % of loss as can be seen in the red curve.

The overall efficiency is slightly lower than expected from the theoretical curve, especially in the range of the lower wavelengths. This can however already be caused by small errors between the simulated or measured supplier data in comparison to the real efficiency. A deviation of only 1 % relative change of the telescope mirror or grating efficiency leads to a change of the total efficiency of around 8 %, which is roughly the difference between the theoretical curve and the measured data.

The integrated efficiency is 54.7 %. According to PGL [73] gold grating efficiencies of 90-95 % can be expected, with four grating bounces this results in 64-81 % maximum efficiency. The gold grating used in this stretcher ranges at the lower limit of this range. Increasing the grating efficiency would be a way, to improve the overall stretcher efficiency. High relative losses are however acceptable in this part of the laser system as the absolute loss in energy is typically still low and can be recovered in the later amplifiers.

4.3.4 Pointing stability

Mechanical stability of the setup was one design criterium for the stretcher. To measure the stability of the setup, a long-term measurement of the input and output beam pointing was performed and the results are displayed in figure 4.15. The pointing was measured using CCD cameras (Basler acA1300-30gm), which measured the focus position of the beam at the input and output of the stretcher. The results of this measurement are shown in figure 4.15. The pointing in X and Y of the in- and output are displayed in the top plots. The differences between in- and output is displayed in the lowest plot.

Over time a drift in both x and y can be observed. In x, the input beam pointing seems to change more, than the output beam. The total input pointing change is around 7 µrad in x and 25 µrad in y. Most of the movement is happening in the first 4 hours, which could hint to a warm-up of the OPCPA laser. Input and output beam however seem to move more or less in the same way. The difference between in- and output increases as well over time. Its magnitude is 4 µrad and 6 µrad in x and in y, respectively.

A probable cause for pointing drifts are temperature changes. Two major heat sources are discussed in the following: The first is the laser beam itself. It has an average power of around 50mW and as the stretcher has a transmission of 55 % 23 mW are absorbed within the stretcher box. The grating causes the largest losses. Part of the power is absorbed by the gold coating [74] and part is reflected into the zeroth order at every grating bounce. These beams are then absorbed by the box walls. Assuming all of the power eventually is absorbed by the air, one can estimate the expected air

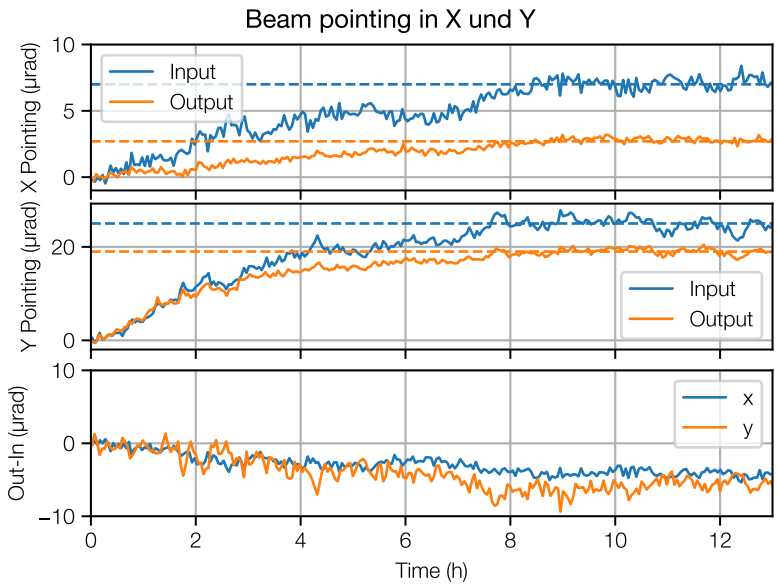

Figure 4.15 – Beam pointing before and after the stretcher in x and y over 13 hours. The difference between in- and output is shown in the lowest plot.

temperature over time. To heat the air in the stretcher box by 1 K, with this power takes around 1.5 h. Thus, a slight temperature increase inside the stretcher box can be expected.

Another and stronger heat source in the setup are the cameras for beam position and pointing measurement, which heat up to 40 °C. They are placed outside of the box, to avoid air turbulence inside the box. The high temperature of the cameras could already explain a movement of the camera by a few µm just by estimating the thermal expansion of the base plate of the camera. This could explain the measured change in pointing between in- and output in vertical direction. The horizontal movement might be caused by similar effects.

To learn more about the heat development inside the box a long-term temperature measurement could be done. To eliminate the influence of the camera heating, an active water-cooling should be installed on them. This way the reliability of the pointing measurement would be improved and the thermal drift of the setup should be reduced.

As the already the camera heating would be enough to explain the measured pointing changes, the stretcher itself most likely does not cause pointing. If the stretcher would cause the pointing, its influence on the subsequent laser could be judged considering the propagation length of the beam from the stretcher output until the Dazzler. The propagation length is about 2.5 m, which would mean a position change of around 12.5 µm would be caused by the stretcher, which is around 1/160 of the beam diameter

in that section, which will not make a difference. The presence of a slow drift of the input beam however motivates a slow beam stabilization into the stretcher.

After confirming the desired behavior of the stretcher by characterizing it on its own in terms of its temporal and spectral properties, characterizing its long-term mechanical stability and its beam quality, the stretcher can be used in the ANGUS system, for stretching the pulses of the new seeder laser MALCOLM. The integration into the total system and its performance will be topic of the next section.

4.4 Integration of the stretcher into the new front-end and connection to the ANGUS laser

As motivated in the beginning, the stretcher should be used to stretch the pulses of the new OPCPA front-end to prepare them for seeding into the ANGUS laser. After characterizing the stretcher and confirming its specifications, it had to be integrated into the overall setup. Figure 4.16 shows a sketch of the layout of the stretcher and its integration into the ANGUS system and the new front-end.

The stretcher is placed next to the engineered version of the Malcolm seeder laser. The beam is guided through the stretcher box, where part of it is used for beam position and pointing diagnostics. The cameras of this diagnostics are placed outside the box, as they usually heat up and can cause air turbulence in the stretcher box. The beam is then finally sent onto the stretcher input axis. After passing the stretcher the beam exits the stretcher on the same axis, but at a different height. Part of the beam is again used for monitoring position and pointing and the beam is sent through a 1:1 imaging telescope. This transports the beam for around 2.5 m into the box of the Dazzler and the Booster multi-pass amplifier, where it is coupled into the ANGUS laser.

To reduce air fluctuations in the stretcher, it is housed. The connections to the OPCPA and the transport to the rest of the amplifier chain are piped. This should increase the passive stability of pointing and position.

To actively stabilize the beam position and pointing between Malcolm and the stretcher, to reduce the influence of eventual pointing changes from Malcolm, as they were described in the previous section, the last two mirrors in the Malcolm box are motorized and stabilize the beam according to the position on the previously mentioned input cameras. At the output of the stretcher and at the input of the Dazzler box, two more mirrors are part of another beam stabilization system. This is a commercial beam stabilization (TEM), which measures position and pointing with two position sensitive detectors (PSD). The stabilized beam is then sent into the Dazzler from where it propagates through the rest of the system. In contrast to the input beam stabilization,

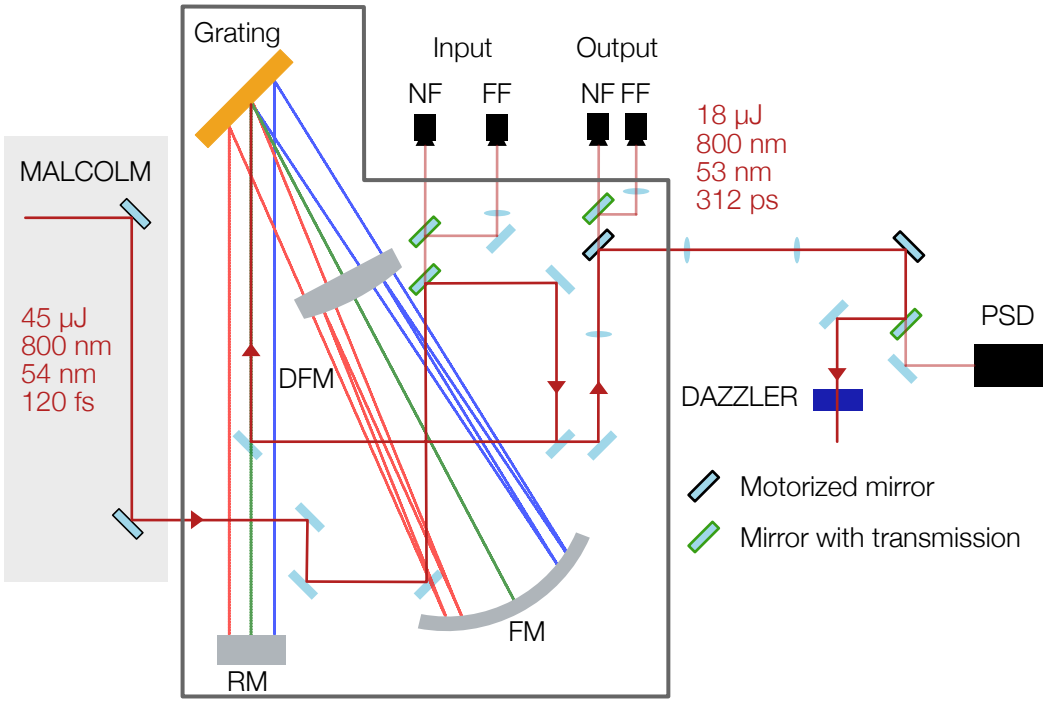

Figure 4.16 – Layout of the stretcher and its integration into the new front-end. The Malcolm output beam is coupled into the stretcher with a camera and picomotor-based beam stabilization. The stretcher output beam is coupled into the ANGUS laser in front of the Dazzler, after an imaging telescope and a commercial beam stabilization.

it is faster and should reduce the pointing jitter, that is acquired by the residual air fluctuations on the beam transport between stretcher and Dazzler.

4.5 Performance in the ANGUS laser

As described above, the stretcher was placed after the new Malcolm seeder laser and the output beam was routed through a telescope and into the Dazzler. From there, it goes through the ANGUS amplifier chain, where it is amplified up to 5 J in several amplification stages. Finally it is sent through the compressor and a 20 m beam line, towards the experiment. To have the pulse compressed at the experiment, the stretcher phase had to be tuned to minimize the pulse duration. This was done in the first step by slowly tuning the grating distance of the stretcher. The pulse length was measured at the target diagnostics with a commercial self-referenced spectral interferometry (SRSI) device (Wizzler, FASTLITE) [75]. Finally the phase was optimized in smaller steps by changing the added spectral phase of the Dazzler. The final pulse duration of

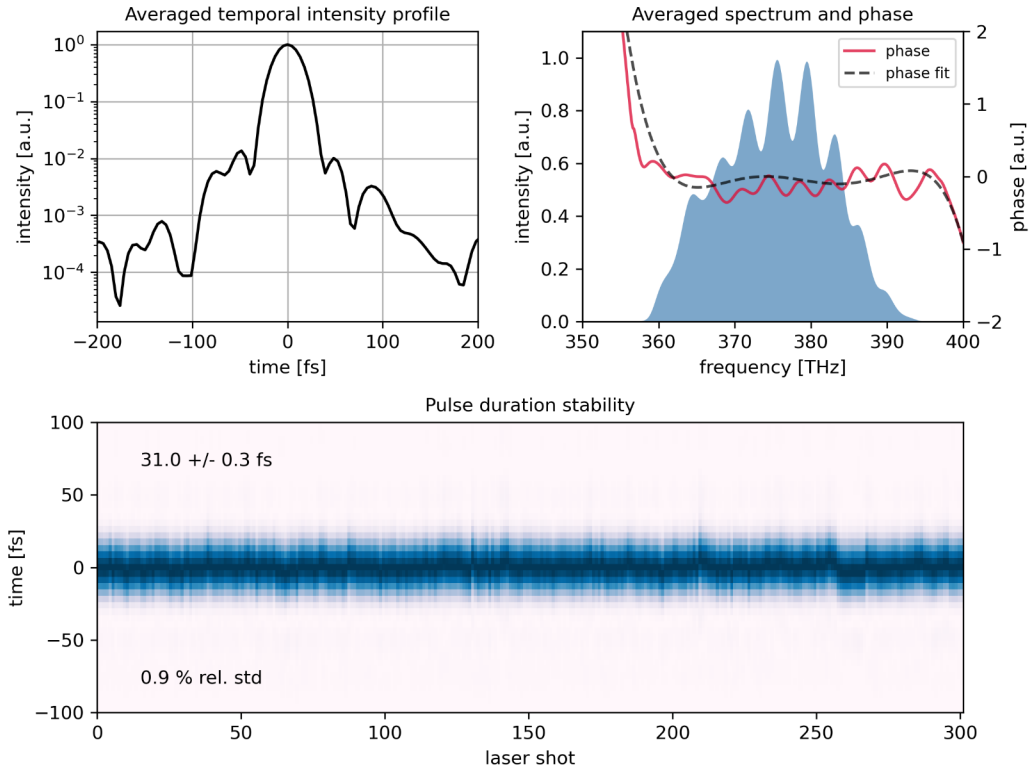

Figure 4.17 – Pulse length measurement of the compressed pulses with a SRSI device (Wizzler). The temporal profile in log scale and the measured spectral intensity distribution and phase are plotted. To measure the pulse length stability a measurement of 300 shots was taken, which is displayed at the bottom. *Courtesy to T. Hülsenbusch and M. Kirchen*

the compressed pulse was 31 ± 0.3 fs. *The presented measurement was performed by T. Hülsenbusch and M. Kirchen*

The measurement of the final pulse is shown in figure 4.17. The temporal intensity is shown on the left and the spectral intensity distribution on the right (blue shaded). The modulation in the spectrum is an artifact of the measurement procedure. The spectral phase, which is reasonably flat over the spectral range of the pulse is shown as well on the right plot. With the new front-end, the pulses could be compressed to slightly shorter pulse durations, 31 fs, instead of 35-40 fs and reach now routinely a sub-percent stability, which was not the case before. The energy stability of all sub-systems has improved as well. A more detailed analysis of the performance of the ANGUS laser with the new front-end, especially in comparison to the old one can be found in the PhD thesis of T. Hülsenbusch [37].

5 A stretcher for the KALDERA laser system

The work presented in this chapter, especially in section 5.7, has partially been published in Optics express [38]. C. Werle has performed the calculation, modeling, planning and setup of the out-of-plane compressor and the planning and setup of the stretcher. The extraction of the pathlength data from the Optics studio model as well as the calculation of the spectral phase from this data have been performed with code initially written by C. Werle. The author of this thesis wrote the main part of the matching algorithm and performed the matching for the presented stretchers. She was in an equal way involved in the stretcher conceptual design, the alignment and characterization and in performing and analyzing the out-of-plane compression demonstration experiment.

5.1 The KALDERA laser system

The KALDERA laser will drive a plasma accelerator for electrons. As discussed in section 3.1, the energy and pulse length for the driving laser for efficient laser-plasma-acceleration are >3 J and sub-30 fs. While the ANGUS laser delivers parameters in this range at 1 Hz repetition rate, the goal of the KALDERA laser is to provide the same parameters at a repetition rate up to 1 kHz. As this is a large step in terms of laser development, the development of KALDERA was divided into three project phases with different target energy and repetition rate in order to develop the required technology step by step. This thesis was conducted during the development, installation and commissioning phase of KALDERA phase 1. A scheme of the KALDERA laser with its different subsystems for each project phase is shown in figure 5.1.

As in the new ANGUS front-end, discussed in chapter 4, a Pharos laser drives an OPCPA (MASUBI), that is used as a seeder for the following CPA system. The pulses are first temporally elongated in a stretcher, the design of which will be discussed in this chapter. Different stretching factors are required for the different project phases which is why two different stretchers will be used. They will be referred to as PICO for phase 1 and STROMBOLI for phase 2 and 3 in the following and the design of both will be discussed. As in ANGUS, an AOPDF (Dazzler, Fastlite) will be used to manipulate the spectral amplitude and phase, which should prevent potential gain narrowing and red-shifting in the Ti:Sa amplifiers and help compress the pulses to their Fourier-limited pulse length. The Dazzler is followed by the PICO booster amplifier based on Ti:Sa, which will be the topic of chapter 6. The booster seeds the

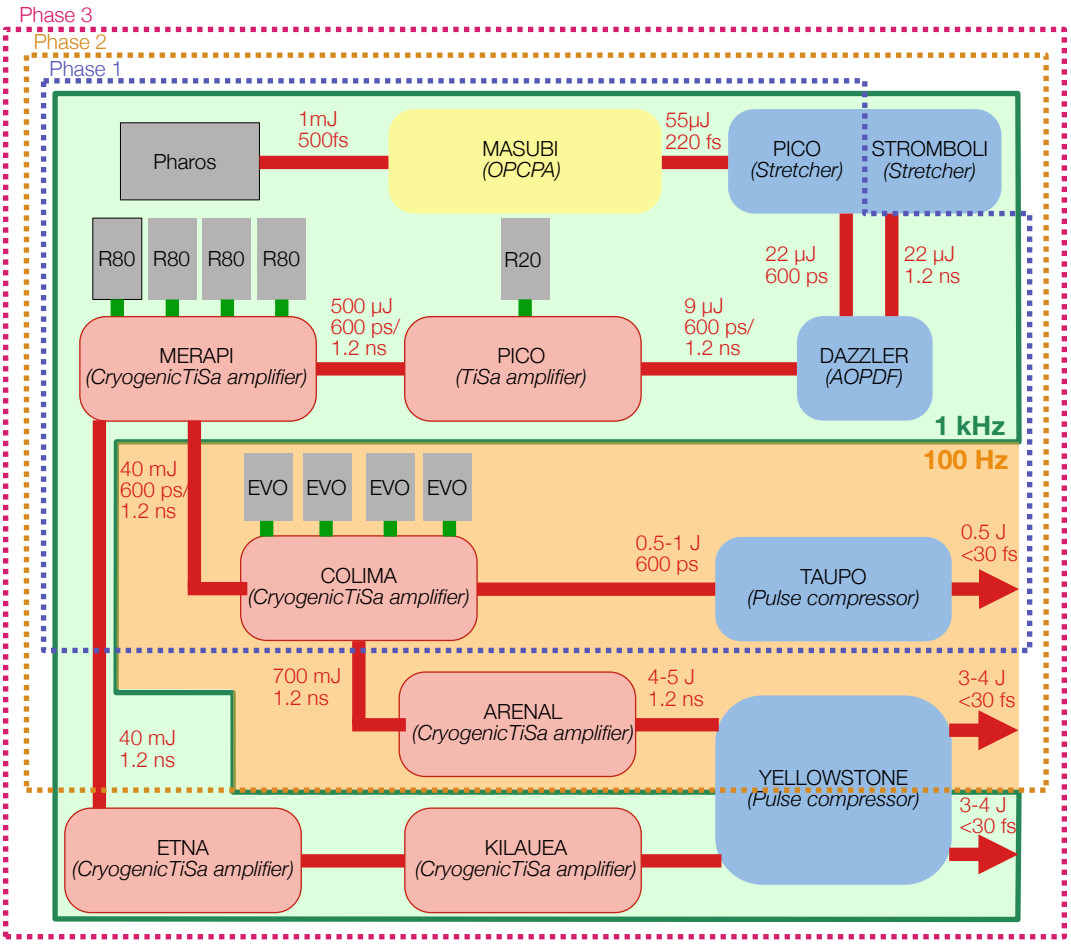

Figure 5.1 – Overview of the KALDERA laser system, including the different project phases. The OPCPA front-end is displayed in yellow, components for dispersion management are displayed in blue, Ti:Sa amplifiers are displayed in red. Pump lasers for the earlier amplifier stages are displayed in grey. The repetition rate of each component is indicated by the background colors, green (1kHz) and orange (100Hz).

first cryogenic amplifier, MERAPI, which provides 40-45 mJ output energy at 1 kHz repetition rate. Up to this point, the system will remain in principle unchanged for all three project phases.

For project phase 1, one more cryogenic Ti:Sa amplifier increases the energy to >500 mJ, but at a reduced repetition rate of 100 Hz. The TAUPO pulse compressor then compresses the pulses to <30 fs. For project phase 2, another amplifier (ARENAL) will be added. It increases the pulse energy to 4 J and will be running at 100 Hz. With the increase in energy, the compressor needs to be exchanged, as the fluence on the compressor gratings has to remain below the damage threshold. The influence of pulse

energy and average power on the compressor and stretcher design will be discussed in greater detail in the next section.

In project phase 3, the COLIMA and ARENAL amplifiers will be replaced by amplifiers with similar output energy, but at 1 kHz repetition rate instead of 100 Hz. The compressor and stretcher of project phase 2 are used in phase 3 as well.

In all three phases, the pulses should finally be compressed to <30 fs. To achieve this, two requirements need to be fulfilled: First, the spectral bandwidth of the pulse has to support this pulse length, which means that the Fourier-limited pulse length of the spectrum should be ≤30 fs. Second, the spectral phase has to be flat over the full spectral range to actually reach this Fourier-transform limit. The second condition is also expressed in

$$D_{\mathrm{tot}}(\omega) = D_{\text{Front-end}}(\omega) + D_{\mathrm{Stretcher}}(\omega) + D_{\mathrm{Amplifiers}}(\omega) + D_{\mathrm{Compressor}}(\omega) = 0. \quad (5.1)$$

The biggest contributions in this equation are $D_{\mathrm{Stretcher}}(\omega)$ and $D_{\mathrm{Compressor}}(\omega)$, as will be shown later. For this reason their dispersions have to be matched well by design. In the following, it will be motivated that the KALDERA compressor must fulfill a number of conditions due to the high average power. The stretcher, which is placed in the front-end where power and energy are much lower, can be adapted more flexibly. This motivates the detailed description of the compressor design given in 5.2, as the design influences the shape of the spectral phase.

The spectral phase contributions of the front-end and the amplifiers will be estimated to determine their influence and eventually adapt the stretcher design accordingly. Both will be described in section 5.3. The implementation of the final stretcher parameters into an optical design will be described in 5.4. The alignment of the stretcher will be detailed in section 5.5. The characterization of the stretcher, that includes measurements of the pulse length, the beam quality, the spectral transmission and the mechanical long-term stability, will be described in section 5.6. Section 5.7 will report on the demonstration experiment for the compression of sub-30 fs pulses with an out-of-plane compressor in combination with the stretcher.

5.2 Compressor design

In designing the KALDERA compressor, the biggest challenge is the high-repetition rate and the corresponding kW average power. Several sources reported on the sensitivity of grating compressors on average power in existing TW peak-power laser systems with even much lower average power [76, 77]. The gold-coated gratings that are commonly used in these compressors absorb around 3-4% of the laser power [74].

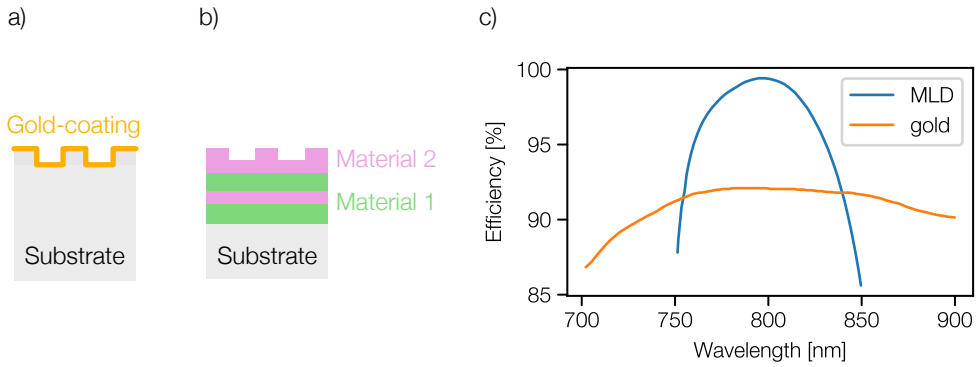

Figure 5.2 – Schematic drawing of a gold (a) and MLD (b) grating, adapted from [82] and [83]. c: Spectral diffraction efficiency of a typical gold grating (Horiba, 1480 lines/mm, 800 nm) in comparison to an MLD grating.

Since the gratings are usually placed in vacuum, no convectional cooling can take place and the gratings can heat up significantly. The heat has two effects: First, it causes deformation of the grating substrate, that introduces spatio-temporal couplings (STCs) in the compressed pulse, which reduces the pulse intensity in the focus. Second, if the surface temperature increases and reaches a temperature >250 °C the grating's coating is damaged. The effect of the deformation on the wavefront and beam divergence has been measured at the ANGUS laser system [77]. Spatio-temporal couplings that originate from these deformations have been simulated [78, 79].

T. Eichner has conducted a study on the capability of gold-coated gratings regarding an increase in average power for beam sizes comparable to the final stage of KALDERA [36]. In this study, he finds, that for a low expansion grating substrate, such as Zerodur, deformation induced STCs start affecting the pulse noticeably for average powers > 1 kW. However, at that point the grating surface temperature would already be above the critical temperature of 250 °C where the grating's coating starts taking damage. Introducing a simple cooling scheme into that model, leads to a factor of ≈ 2 in average power until the same temperatures are reached. Experiments of active cooling of compressor gratings have been performed by Power et al. [80] and Alessi et al. [81]. The maximum average intensity from these experiments is named as 3.88 W/cm^2 [80]. This corresponds to an average power of around 388 W for the KALDERA target beam parameters. In [81] an average power of 680 W is achieved . Both are however not quite sufficient for the final parameters of KALDERA [33], leading to the conclusion, that gold gratings are not a suitable option for the KALDERA compressor and an alternative has to be found.

An alternative grating type are multilayer-dielectric (MLD) gratings [84]. They are compared to gold gratings in figure 5.2. The fundamental difference is that the coating consists of a stack of dielectric layers with alternating higher and lower refractive index

instead of a metal layer that itself is reflective for a broad range of wavelengths. The diffraction efficiency of an MLD grating depends very much on the exact dimensions of the grating structure as well as the multi-layer thicknesses [84]. In addition, it shows a much stronger dependency on the incidence angle as well as the wavelength of the incident light [84, 85].

The first advantage of MLD gratings is that they absorb much less power than gold gratings. The absorption from MLD gratings has been measured to be in the range of tens of ppm [86]. The main loss process is reflection into the zeroth order. This strongly reduces the gratings' heating and mitigates the aforementioned heat-induced deformation and destruction.

The second advantage is that they reach higher peak diffraction efficiencies [73]. However, due to the wavelength and angle dependence of the interference condition, their efficiency is very dependent on the wavelength λ and the specific angle θ the grating is used at [85]. Thus, the spectral bandwidth they provide is more limited, as is the input angle acceptance range. Efficiencies of a typical gold-coated (HORIBA, 1480 lines/mm for 800 nm cwl) and an MLD grating are compared in figure 5.2.

The MLD grating reaches a much higher peak efficiency of >99 % compared to the gold grating with around 92 %. But while the gold grating efficiency is almost constant from 750-900 nm, the MLD grating efficiency has a much narrower peak, limiting the bandwidth of the compressed pulses. For pulses within the spectral range, however, the overall efficiency η increases. This is especially significant considering the final efficiency after a four-grating compressor η^4. Thus, the use of MLD-gratings helps to reduce the energy requirements of the final amplifier, which again relaxes cooling requirements and cost for pump power in the laser amplification chain. Last but not least, the laser-induced damage threshold (LIDT) of MLD gratings tends to be higher, than that of gold gratings [84]. This makes MLD gratings attractive for systems with high final pulse energies and average power.

Only recently MLD gratings for the use in Ti:Sapphire fs-laser systems have been designed and manufactured [73, 86]. To achieve the highest and spectrally broadest diffraction efficiency, they have to be used at incidence angles close to the Littrow-angle [73]. This means the incidence angle θ_{in} fulfills equation

$$\theta_{in} = \theta_{-1}, \tag{5.2}$$

where θ_{-1} denotes the diffraction angle of the -1st order [87]. To still ensure the separation of the incoming and the diffracted beam, it was proposed to introduce an additional tilt to the grating, that sends the diffracted beam out of the initial beam plane [73, 86, 88]. This configuration is called out-of-plane (OOP) geometry and a compressor of that geometry is shown in figure 5.3. For small angles (δ<10 °) the supported bandwidth stays mostly unchanged. However, there are a few downsides

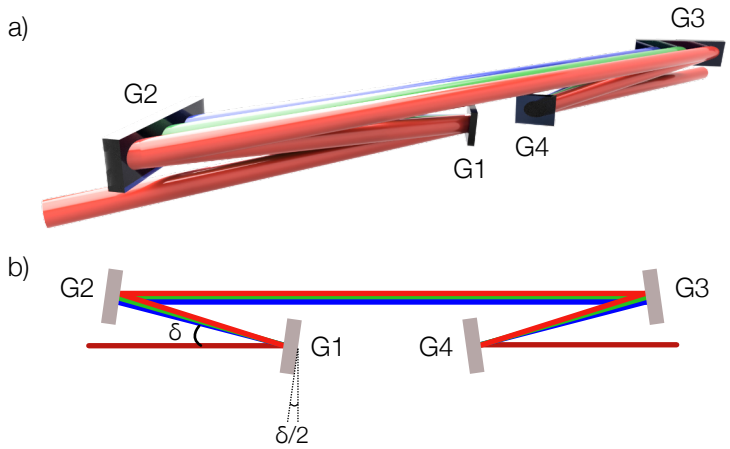

Figure 5.3 – Iso-view (top) and side view (bottom) of a four-grating OOP compressor with out-of-plane angle δ. Figure adapted from [38].

to this approach: Firstly, it increases the complexity of the setup and alignment of the compressor, as not all beams propagate parallel to the table plane. Secondly, the beam size is decisive for the distance between the gratings of a grating pair. As the full beam has to achieve a height step from the first to the second grating and the angles are limited to angles $<10\,°$, the minimum grating distance and thus the minimum dispersion is mainly governed by the beam size. The beam size again is determined from the final pulse energy and the maximal allowed fluence that needs to be well below the damage threshold of the compressor gratings. This means scaling the laser energies does not only lead to a scaling of grating size, but also a scaling of the compressor dimensions and ultimately the stretched pulse length.

For KALDERA such an OOP compressor has been designed and modeled in the ray-tracing program OpticStudio (OS) for both project phase 1, with 500 mJ output energy and project phases 2 and 3 with 3-5 J output energy by C. Werle. The grating density was 1480 lines/mm for both, the grating incidence angles are 36.3 ° and 36.8 °, the grating distances are 820 mm and 1770 mm. The OOP angle $\delta/2$ is 3.8 °. From the ray-tracing in OS, an optical path length difference for the wavelengths between 700 and 900 nm was extracted which was then used to calculate the spectral phase $\phi_{\text{compressor}}$. The effect of the out-of-plane angle on the spectral phase was already considered this way.
Knowing the spectral phase of the compressor, the remaining contributions from the front-end $\phi_{\text{front-end}}$ and the amplifiers $\phi_{\text{amplifiers}}$ will be estimated next.

5.3 Stretcher matching

The front-end of KALDERA is a double OPCPA system [36] and delivers 25 fs FTL pulses, that are stretched to around Δt=220 fs. Assuming Gaussian-shaped pulses, the front-end GDD can be estimated using [89]

$$\mathrm{GDD} = \frac{\Delta t_0^2}{4ln2}\sqrt{\left(\frac{\Delta t}{\Delta t_0}\right)^2 - 1}, \tag{5.3}$$

where Δt_0 is the Fourier-transformed pulse length and Δt the stretched pulse length. This results in $\mathrm{GDD_{OPCPA}} = 1974\, fs^2$, which corresponds to <1% of the total phase.

The laser gain medium Ti:Sapphire causes most of the spectral phase for the amplifier system, as the laser passes a significant amount of that material. Its contribution was estimated based on a preliminary design of the laser amplifier chain. The contribution to the spectral phase was calculated from the wavelength-dependent refractive index [90]. An estimated length of propagation through Ti:Sa in KALDERA and the resulting GDD, TOD, FOD and FiOD are listed in table 5.1:

	Total Ti:Sa length [mm]	GDD [fs^2]	TOD [fs^3]	FOD[fs^4]	FiOD[fs^5]
Phase 1	210	12188	8846	-3269	9091
Phase 2 & 3	290	16831	12216	-4514	12553

Table 5.1 – Overview over the propagation length through Ti:Sa in the KALDERA amplifier system and the resulting GDD, TOD, FOD and FiOD for KALDERA phase 1 and 2 and 3

These contributions will be considered in the matching of the stretcher dispersion to the compressor dispersion.

The mirrors in the laser system are customized broadband mirrors with high LIDT and a specified with a dispersion of $<|50|\,\mathrm{fs}^2$. The number of mirrors in the system is around 150 for project phase 1 and 200 for project phases 2 and 3. Which means the potential additional GDD adds to $<|7500|\,\mathrm{fs}^2$ or $<|10000|\,\mathrm{fs}^2$. Because only the absolutes of the mirror GDDs are known it was not included in the dispersion matching routine. The amplitude of the phase is small enough that the contribution of the mirrors can easily be compensated for, either by slightly tuning the stretcher parameters after the setup, or by manipulating the phase with an AOPDF. It can compensate phase mismatches up to a GDD of around 100000 fs^2 from unaccounted sources. The AOPDF that is used in KALDERA is the Dazzler (HR450-1050, Fastlite). This allows to optimize the pulse length at the experiment without readjusting the stretcher [91]. Other potential

Parameter	500 mJ	5 J
grating line density (lines/mm)	1480	1480
grating distance (mm)	406.909	880.367
angle of incidence (°)	36.031	36.299
Radius of curvature (m)	1.00	2.50
Diffraction angle for 800 nm (°)	36.563	36.173

Table 5.2 – Final parameters of both stretchers. The line density and the mirror radius of curvatures were set. The grating distance and angle were fitted with analytical formulas [65] and the diffraction angle for 800 nm was calculated from the input angle and the grating line density.

components that would contribute to the spectral phase are e.g. lenses, the air, and windows.

After discussing and estimating potential contributions to the spectral phase by the amplifier chain, the stretcher phase can be matched to minimize the final spectral phase. Jiang et al. [65] provide analytical formulas to calculate the spectral phase of an Oeffner stretcher in dependence of its parameters radius of curvature of the focusing mirror R, incidence angle θ, grating line density g and grating distance G. Using the provided formulas, these parameters could be used as fit parameters to match the negative of the compressor and amplifier phase, such that equation 3.12 is fulfilled.
For availability of components, the grating line density was fixed to 1480 lines/mm and, after a first step of fitting, the radius of curvature for the focusing mirror was fixed to an even value close to the fitted one for availability of mirror substrates. In addition, it had to be ensured that the telescope provides enough space for the gratings.

To save space and keep the optics small, the stretcher was planned as a double-pass configuration. This means the outgoing beam is sent through the stretcher a second time at a different height, which doubles the stretching factor.
In total, the fitting was performed for two stretchers: The first is matching the compressor of KALDERA phase 1, designed for a 500 mJ beam with a fluence of 50 mJ/cm^2. The second provides an estimation for KALDERA phases 2 and 3 with an energy of 3-5 J and the same fluence on the compressor gratings. Both stretchers were planned and simulated with the same methods.

In figure 5.4, the spectral phase of the compressors (blue), the amplifiers (black) and the stretcher (pink) are shown for both configurations, project phase 1 (left) and project phases 2 and 3 (right). The residual spectral phase (orange, right y-axis) ϕ_{tot} is dominantly of 4th order and <30 rad over the wavelength range from 700-900 nm. The resulting stretcher parameters that create the shown stretcher phase are summarized in table 5.2. As expected, the Littrow configuration of the compressor leads to angles of incidence in the stretcher, that are close to the Littrow configuration as well. This

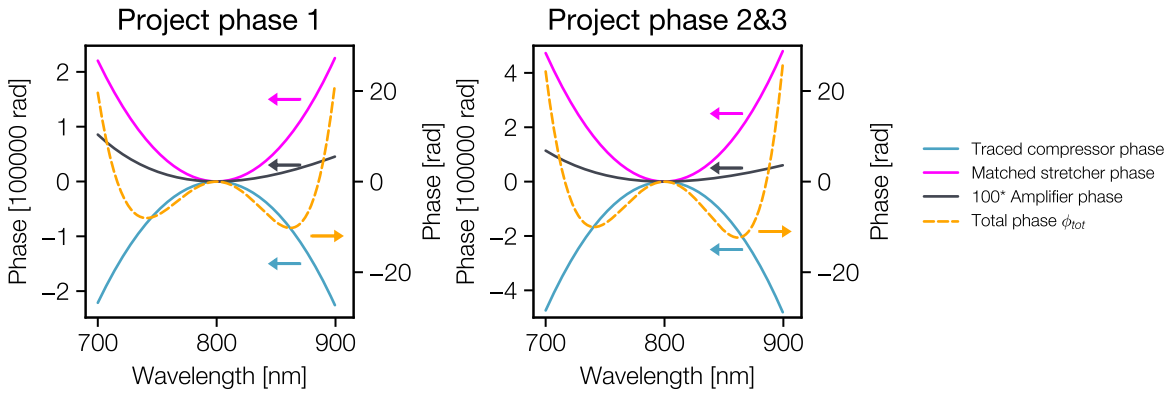

Figure 5.4 – Spectral phases of compressor (blue), stretcher (pink) and combined amplifier and OPCPA (black), which was multiplied by 10 to improve its visibility. The residual error (orange) is obtained by adding all three of them. The left pane shows the phases for project phase 1, the right for project phases 2 and 3.

means again, that the diffraction angle is almost the same as the input angle. The realization of such a stretcher will be discussed in the next section.

5.4 KALDERA stretcher design

The required stretcher parameters have been determined in the previous section. Most notably, the input and output angle are very similar. To realize this geometry with reflective gratings one has to achieve a separation between the incoming and outgoing beams by means of an out-of-plane geometry similar to that of the compressor. As this highly increases the geometric complexity of the stretcher, transmission gratings were chosen instead, where incoming and diffracted beam are naturally separated. As mentioned before, the stretcher was designed to be used in double-pass to gain more stretching in a smaller footprint. As discussed in chapter 3, a two-grating stretcher provides a higher beam quality, than a one-grating stretcher. Especially, since a double-pass stretcher is planned, a two-grating stretcher is chosen. The final stretcher is a two-transmission-grating Oeffner stretcher which is passed two times.

The final design is shown in figure 5.5. The beam meets the first grating (G1) under the angle ϑ and is diffracted. It passes the Oeffner telescope, consisting of a focusing mirror (FM) and a defocusing mirror (DFM). In the side view (a), the height steps that the roof-mirrors introduce to the beam can be seen. The top view (b) shows the spectral splitting of the beam, where the longest wavelengths (red beam) are diffracted stronger than the shorter wavelengths (blue beam). The analytical formulas from [65] are valid for a geometry where all beams propagate in the central plane of the

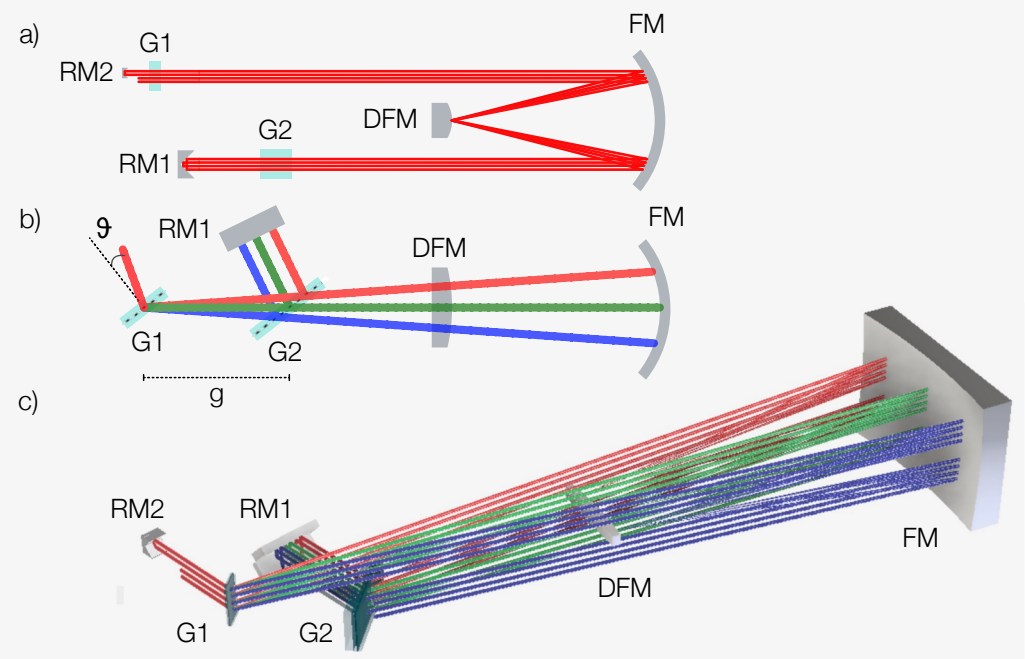

Figure 5.5 – Layout of the final stretcher. Side view (a), top view (b) and iso view (c) of the two-grating transmission grating Oeffner stretcher, with the optical components: Transmission gratings G1 and G2, focusing mirror (FM), defocusing mirror (DFM) and roof-mirrors RM1 and RM2. The grating distance G and the grating incidence angle ϑ are sketched in the top view. Figure adapted from [38].

telescope. To check if the real setup with reflective optics and beams offset to the central plane gives the same phase, the stretcher was modeled in OS and the expected stretcher phase was calculated using the same ray-tracing algorithm that was used for the compressor before. The resulting phase is compared to the analytically matched phase in figure 5.6 and the residual error is displayed in red. It is close to zero over almost the full spectral range and thus negligible.

As the stretcher parameter and layout have been explained, the alignment procedure will be discussed in the following.

5.5 Setup and alignment of the stretcher

As described in the previous chapter, the alignment of the stretcher requires special care as non-optimized stretchers cause angular and spatial chirp in the beam. In this section, the general alignment and the angular chirp optimization will be discussed.

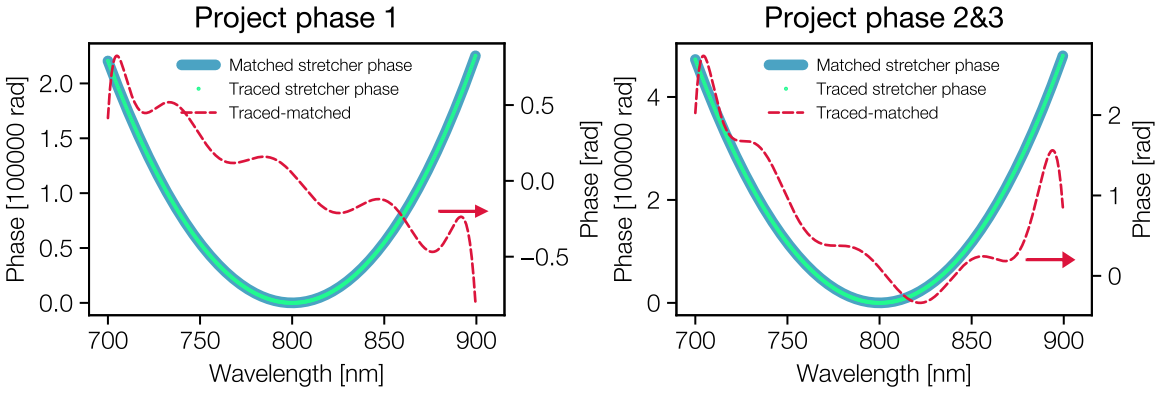

Figure 5.6 – Comparison of analytical (blue) and traced (green dots) stretcher phase. Their difference is marked in red and within the range of a few rad.

5.5.1 General alignment

The first alignment of the optical components included the following steps, which are depicted in figure 5.7 a)-d).
1. Alignment of the tip and tilt angle of the focusing mirror: The beam is aligned on the defined input axis with two pinholes at the central height of the stretcher. The focusing mirror is placed perpendicular to the beam. The tip and tilt of the focusing mirror are adjusted until the beam is back-reflected through both pinholes.
2. Alignment of the position, tip and tilt angle of the defocusing mirror (DFM): The beam is aligned on the central axis of the stretcher, but at height h above the symmetry axis. The DFM position, tip and tilt angle are adjusted until the beam is reflected back through both pinholes on the input axis but at height h below the symmetry axis (green).
3. The input beam is aligned at its design angle. The first grating (G1) tilt and in-plane-rotation are tuned, until the beam passes the irises on the stretcher central axis (green).
4. The second grating is placed at its design position and tuned until the diffracted beam is at the designed output axis. The fine tuning is performed during the angular chirp optimization.
After the stretcher is roughly aligned, a fine alignment has to be performed to minimize the angular and spatial chirp.

5.5.2 Angular chirp optimization with a three-color-laser

The limits for acceptable angular chirp are the same as the ones discussed in section 4.2.2. However, in contrast to a one-grating Oeffner stretcher, a perfectly aligned two-grating Oeffner stretcher does not cause any chirp (see chapter 3). Furthermore,

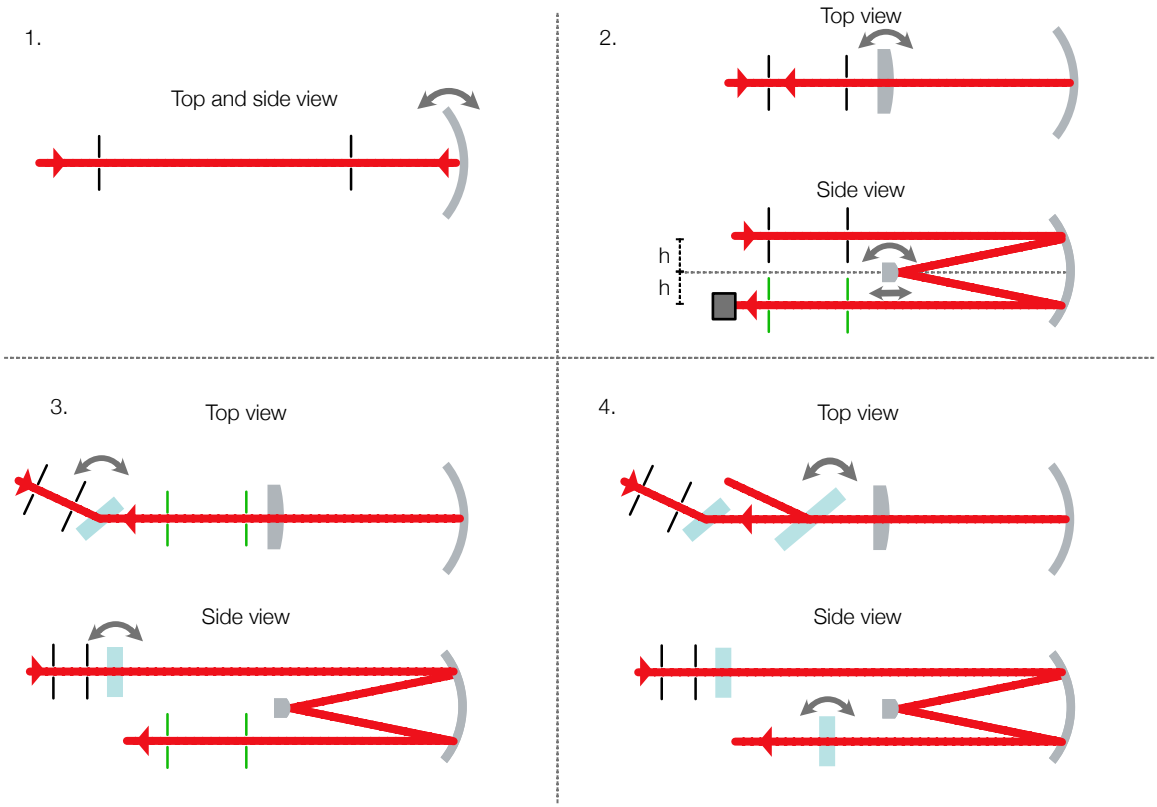

Figure 5.7 – Visualization of the stretcher alignment method. 1. Tip and tilt alignment of the focusing mirror; 2. Tip and tilt alignment of the defocusing mirror, tuning of telescope length on collimation; 3. Alignment of grating 1 angle and in-plane rotation; 4. Alignment of grating 2 tip, tilt and in-plane rotation

because both gratings can be tuned independently, the compensation of the angular chirp is relatively straight-forward. Horizontal chirp can be minimized by adjusting the second gratings' tilt angle, vertical angular chirp can be optimized by adjusting the second gratings' in-plane-rotation.

During the optimization the angular chirp was measured with the three-color-laser method that was described in detail in the previous chapter. As before, the transverse focus positions of the three colors were measured. The angular chirp is then approximated by the slope of the linear fit of the three focus positions. As described in the previous chapter, the output of the three-color-laser itself shows some angular chirp. This was measured prior to the stretcher optimization and the result is represented by the blue dots in figure 5.8. The stretcher was tuned until the output beam showed the same angular chirp as the three-color laser, performing a relative measurement.

The angular chirp after the unoptimized stretcher (pink) is around 1 µrad/nm in both axes. It can be reduced by tuning the G2 in-plane rotation and tilt angle. After the optimization, the linear angular chirp after the stretcher (black) is the same as the

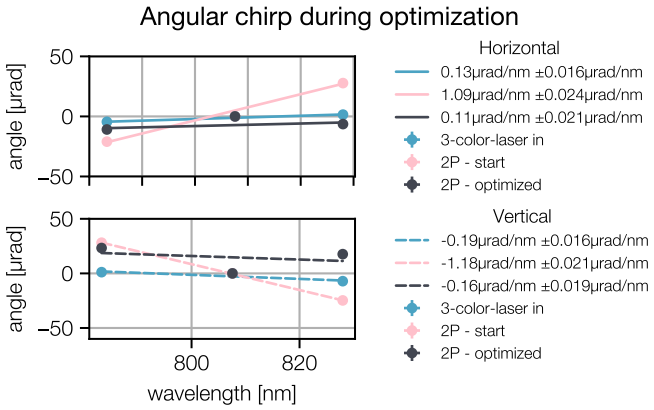

Figure 5.8 – Angular chirp of the three-color laser (blue). Measurement of the angular chirp before (pink) and after (black) the optimization of the G2 in-plane rotation and tilt angle.

three-color-laser angular chirp within the measurement precision. The error is deduced from the quality of the fit and the standard deviation of the position measurement. Even if the linear chirp was successfully minimized, the final setting still shows a residual quadratic chirp, that could not be compensated.

To check the method, another measurement of the angular chirp was performed using a commercial imaging spectrometer (MISS, Femtoeasy). The results are shown in figure 5.9. To evaluate the measurement, the center of mass positions for every wavelength are calculated, which are represented by the red dots. The angular chirp is derived as the slope of a linear fit of these positions. In both directions the chirp is below or in the range of the resolution limit of 0.1 µrad/nm, that was estimated for this imaging spectrometer in section 4.2.2. It is below the critical values for angular chirp in a stretcher, discussed in section 4.2.2, so the alignment the alignment procedure was successful. The minimization of the spatial chirp was performed analogously to the minimization of the angular chirp, except, that the near-field position of the three-colors was considered, instead of the focus position. A precision in the range of µm/nm was achieved and deemed sufficient. In the next section the characterization of the stretcher will be described.

5.6 Characterization of the KALDERA stretcher

To characterize the performance of the stretcher, multiple measurements were performed. The pulse length of the output pulses was measured for several grating distances to confirm the spectral phase calculations. The beam quality factor M^2 was determined for the beam with the whole spectrum and for four individual wavelengths

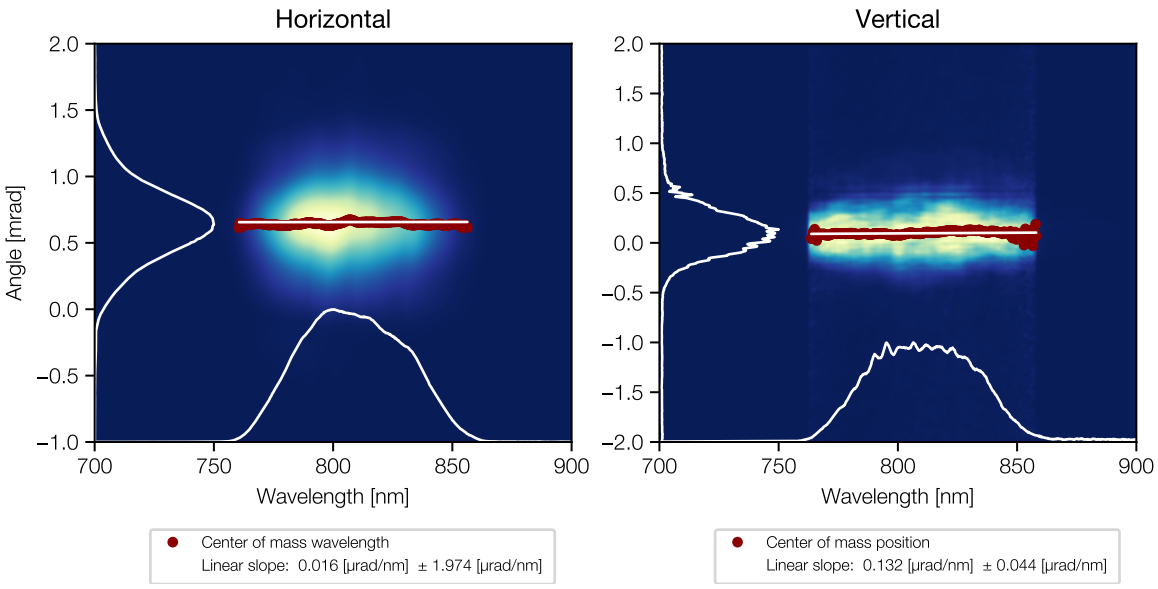

Figure 5.9 – Measurement of the angular chirp with an imaging spectrometer (MISS) after alignment with the three-color-laser method. The beam was focused onto the imaging spectrometer with a f=1000 mm lens. The measured signal in horizontal (top) and vertical (bottom) direction is shown. The beam position for every wavelength (red dots) and a linear fit (white) is shown.

within the spectrum. A long-term measurement of pointing and position of the in- and output beams has been performed and the spectral efficiency of the system has been characterized and compared to the expected efficiency.
As is shown in figure 5.10, the characterization is performed with the output of the development setup of the later KALDERA OPCPA front-end. The pulse energy was 40 µJ, the central wavelength 790-800 nm and the spectrum had a Fourier-limit of 24 fs. The pulses were temporally stretched to around 300 fs.
Except for the pointing measurement, all of the characterizations have been performed in a configuration where the grating distance was set to match the compressor of the later out-of-plane demonstration experiment and not for project phase 1-3. This means the absolute pulse lengths are smaller than the pulse length that will be used later in KALDERA. The change of pulse length per change of the grating distance, however, should be the same as in the later configuration for KALDERA. The routine of determining the spectral phase and pulse length is the same for both cases and can be thus checked as well. The other measured parameters should not change either.

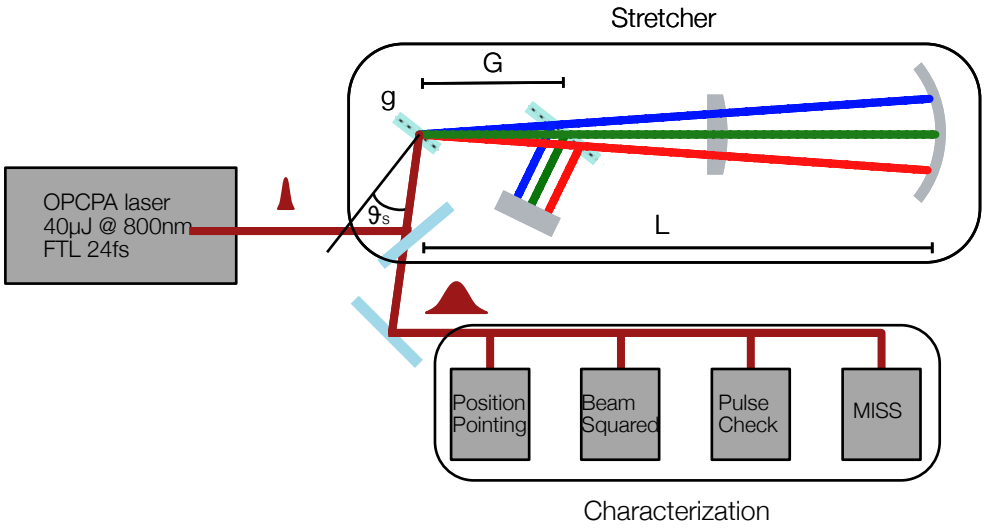

Figure 5.10 – Setup of the characterization measurements of the stretcher. The input beam is an OPCPA laser. After the stretcher several measurement devices are placed to measure beam and pulse properties as M^2, pulse duration, angular chirp and position and pointing.

5.6.1 Pulse duration measurement

To check the correct stretching of the pulse and confirm the previous simulations, the stretched pulse length was measured with a long-range autocorrelator (APE PulseCheck). The grating distance was scanned and the pulse length and output spectrum were measured for every setting (see figure 5.11, red dots). The error bars represent the standard deviation of the measured pulse lengths.

As for the previous stretcher, the grating scan was performed in the simulated model in Optics Studio as well. For every set point a ray-tracing was performed for several wavelengths to determine the path length difference. From these path lengths and the measured spectrum of every set point, a pulse length was calculated, represented by the blue dots.

The pulse lengths, that were calculated by this method differ from the measured pulse lengths. The same routine of simulating the measurement routine that was used to understand the difference in pulse length for the previous stretcher was applied to this measurement as well. The resulting pulse lengths are represented by the orange dots. The values match the measured ones, which indicates, that again the measurement procedure causes the mismatch between the measured and simulated values, likely due to the non-Gaussian spectral intensity distribution. Both in the simulation and in the measurement, the pulse length changes linearly with the grating distance. The slope

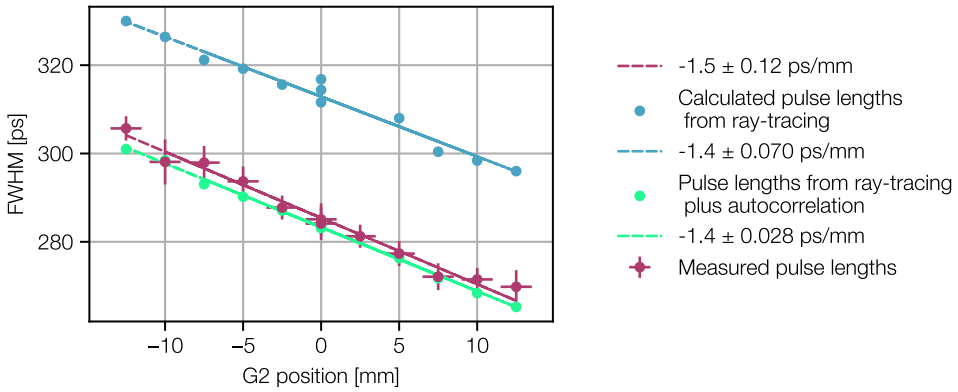

Figure 5.11 – Output pulse length of the stretched pulse for different grating distances. The pulse length was measured with an APE long-range autocorrelator. The simulated results were retrieved from a ray-tracing model of the stretcher in combination with the measured output spectrum.

of the linear fits lies in the range of 1.5 ps/mm. The pulse width is 312 ps FWHM for the central position.

5.6.2 M^2 measurement

To learn if the stretcher affects the beam quality factor M^2, it was measured for the input and output beam of the stretcher. The measurement was performed with a commercial M^2 measurement device (BeamSquared, Ophir) which focuses the beam and measures the second moment beam size through the caustic. The results are presented in figure 5.12. The M^2 was determined by using

$$w_{x/y}^2(z) = w_{0x/y}^2 + M_{x/y}^4 \left(\frac{\lambda}{\pi w_{0x/y}} \right)^2 (z - z_0)^2 \tag{5.4}$$

as fit function [72]. The errors were derived from the estimated precision of the beam size measurement (5 µm) and the fit error.
In the plots on the left, the input beam (red, X_I/ Y_I), the beam after the stretcher (blue, X_O/ Y_O) and the output beam of the stretcher, that was discussed in the previous chapter (green, X_A/ Y_A) are compared. It can be noted, that the M^2 of the input and output beam are the same, within their error ranges. In comparison, the M^2 of the previous stretcher is a little higher, which could hint to the previously mentioned aberrations, that are introduced by a one-grating stretcher, in contrast to a two-grating stretcher. The difference is however not large. In y all three M^2 values are again the same within their error range. It should be noted, that all three beams had different input beam sizes, which is the main reason for the different waist diameters.

The measurement of the output beam with different bandpass filters, shows again a higher M^2 in x in the 790 nm beam, which could already be seen in the previously described stretcher. All other measured M^2s are close to each other and close to the M^2 of the non-filtered beam, which hints a good angular overlap. Overall, the good M^2 of the input beam is conserved in the stretcher.

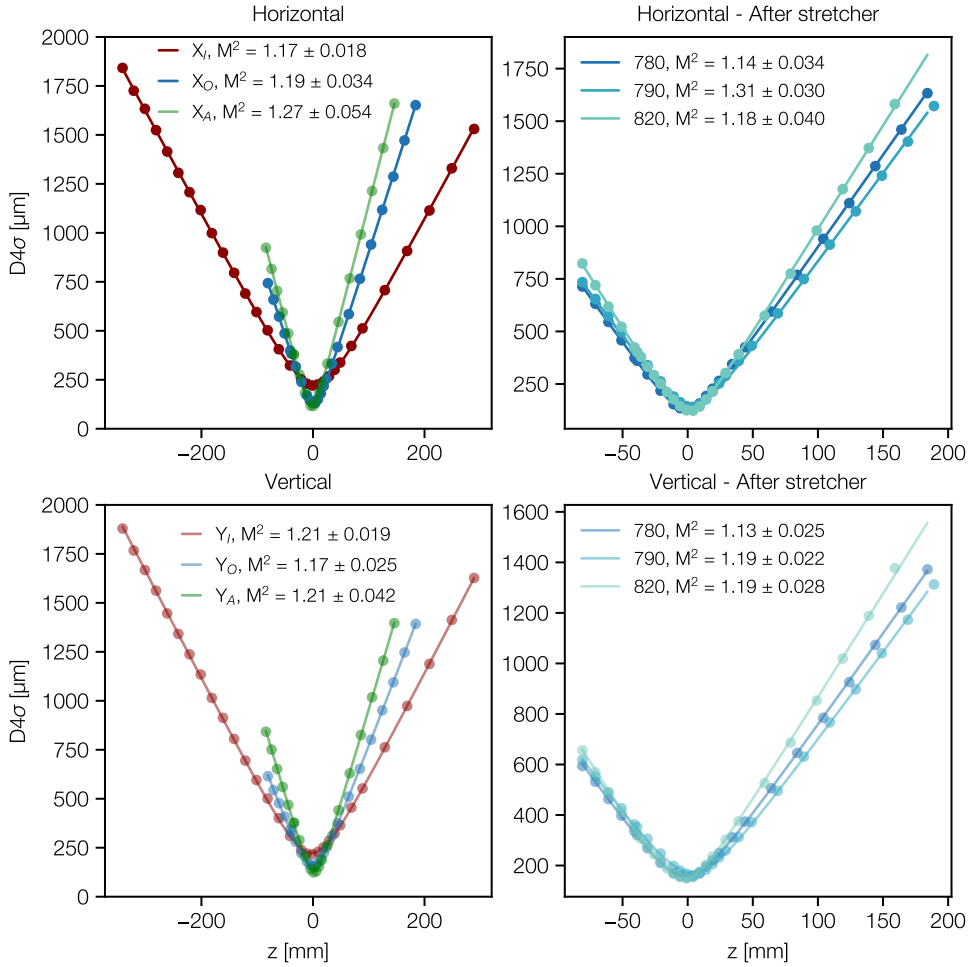

Figure 5.12 – Left: Beam caustic of the beam into the stretcher (red), out of the stretcher (blue) and out of the stretcher, described in the previous chapter (green), measured with a BEAMSquared device. The dots represent the individual beam size measurements along z, the solid line is a fit, from which the M^2 was determined. Right: Beam caustics of the stretcher output, filtered with different bandpass filters. On both sides, the top shows the horizontal, the bottom the vertical beam axis.

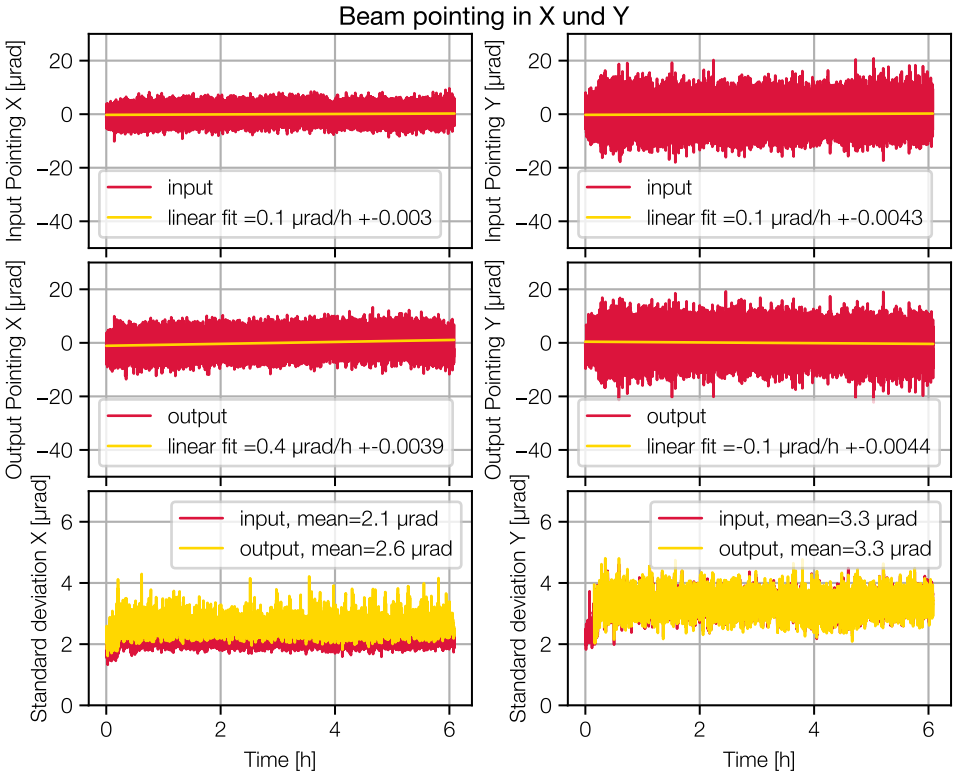

Figure 5.13 – Beam pointing in x (left column) and y (right column) before (top row) and after (middle row) the stretcher. A linear fit (yellow) shows the trend, the rolling standard deviation (window size =100) is shown in the bottom for input (red) and output (yellow).

5.6.3 Beam pointing measurement

Mechanical stability of the setup was one design criterium for the stretcher. To proof the stability, a long-term measurement of the input and output beam position and pointing has been performed,using the input and output online diagnostics of the stretcher. The results are displayed in 5.13. The pointing in x (left column) and y (right column) at the input (top row) and at the output (bottom row) are shown. To visualize the drift, a linear fit is added to the data. In x, a drift of 0.1 µrad/nm shows in the input beam. The drift of the output beam shows a slightly larger drift with 0.4 µrad/nm. The drift in y is 0.1 µrad/nm for both, in- and output, with flipped signs. The standard deviation of the pointing for in- and output in x and y is shown in the bottom row. In x, the standard deviation increases slightly through the stretcher, in y, the jitter is exactly the same as the input jitter.
It seems that stretcher output pointing jitter and drift in y originate from changes of the input pointing. An increase in pointing jitter in x as well as a small drift can be noticed. The source of this is not clear yet. During the measurement, the stretcher

was enclosed in a metal box. The main two possible sources for an increase in beam pointing jitter would be heating of the air due to four running cameras inside the box, or mechanical movement of components. A first step to improve the pointing in x would be the installation of a camera cooling. To prevent large drifts of the input beam a beam stabilization is installed in front of the stretcher. Overall, the pointing stability of the stretcher is already very low. To reduce pointing jitter in the sections after the stretcher another beam stabilization system is installed. Its influence on the beam stability and on the energy stability will be discussed in chapter 6.

5.6.4 Spectral efficiency

The spectral efficiency was measured to estimate the overall energy losses in the stretcher and to judge if the stretcher transports a sufficient bandwidth for <30 fs pulses. The measurement was performed by sending the beam of the OPCPA front-end in and measuring the spectrum right in front and directly after the stretcher. In order to measure in the broadest possible range, the OPCPA was tuned to three different spectra that were combined for the final curve, averaging over the data in overlapping spectral areas. The resulting spectral efficiency is shown in figure 5.14. The theoretical stretcher efficiency that is shown for comparison was obtained by combining the spectral efficiency curves of the individual stretcher optics provided by the manufacturers.

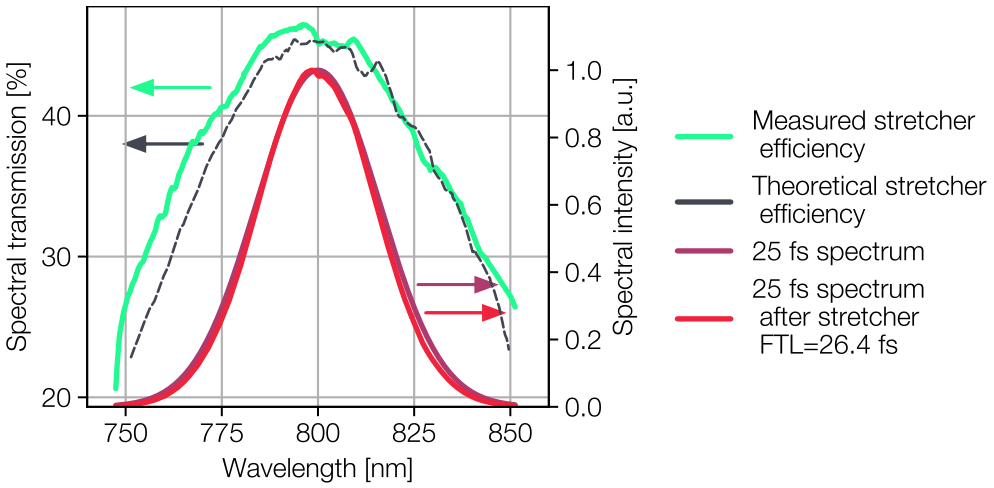

Figure 5.14 – The measured spectral efficiency of the total stretcher (light green) is compared with the expected efficiency (black). An exemplary output spectrum (red) is shown, assuming a 25 fs FTL input spectrum (violet).

The measured efficiency matches the expected efficiency well in overall shape and absolute values. The efficiency is, however, relatively low for a stretcher, at 46.5 % as peak value and 43.5 % integrated transmission over a 25 fs spectrum. This is mainly caused by the double-pass configuration that includes eight bounces on the gratings. As the gratings are the least efficient component, the overall efficiency is reduced. These losses must be compensated by the subsequent amplification chain.
The effect of the spectral efficiency on the pulse length is illustrated by multiplying the spectrum of a 25 fs Fourier-transform limited pulse (violet curve) with the spectral efficiency. The FWHM of the resulting spectrum (red curve) is around 2 nm smaller which increases the FTL to 26.4 fs.

After a thorough characterization of the pure stretcher performance, it was used in the demonstration experiment for an out-of-plane compressor based on multilayer-dielectric gratings, which will be described in the following section.

5.7 Demonstration of sub-30 fs-pulse compression with an out-of-plane compressor with multilayer dielectric gratings

To prove the feasibility of a MLD grating compressor to compress pulses to sub-30 fs at KALDERA, a compression demonstration experiment was set up using a smaller on-air MLD compressor. The stretcher grating distance was set up to match the demonstration compressor grating distance. The general setup for this experiment is shown in figure 5.15. The same seed laser that was used for the stretcher characterization was used for the demonstration experiment. Both the stretcher and compressor were prealigned with the three-color-laser to minimize angular and spatial chirp and achieve optimal compression. The fine alignment of the beam into the setups was performed using previously set up position and pointing diagnostics at the in- and outputs. After the compressor, a long-range autocorrelator from PulseCheck, a FROG measurement device (Grenouille) and a high-dynamic third-order range autocorrelator (Tundra, Ultrafast Innovations) were set up as temporal diagnostics for the compressed pulse.

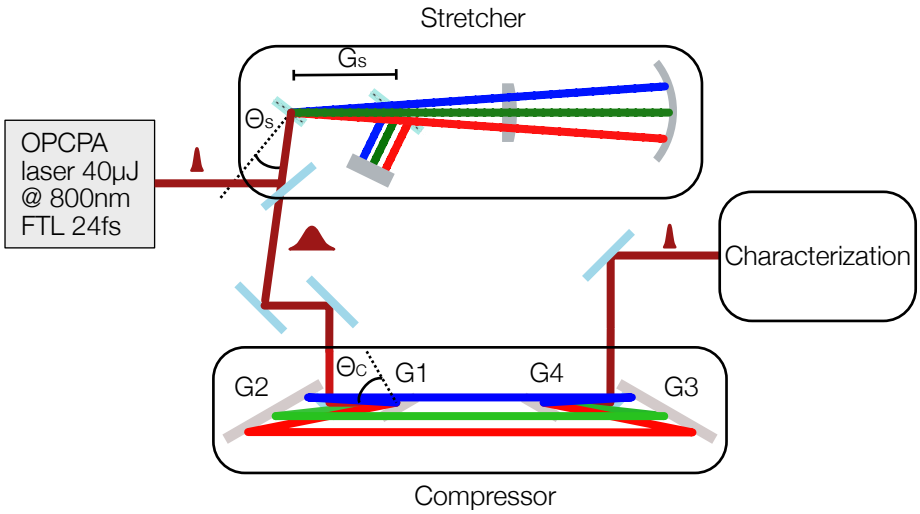

Figure 5.15 – Setup of the OOP compression demonstration experiment. The characterization was performed, using a long-range autocorrelator (PulseCheck), a FROG measurement device (Grenouille), a short-range autocorrelator (Wizzler) and a high dynamic 3rd order range autocorrelator (Tundra) for contrast measurement. Adapted from [38].

The compressor was used in two different configurations. As larger MLD gratings were not available, during the experiments, the larger gratings (G2 and G3) were replaced by gold-coated ones. This configuration was used for the compression experiment. For the later polarization experiment, the gold gratings were replaced by smaller MLD gratings.

For the final compression of the pulses, it was necessary to precisely match the grating angles and distances of the stretcher and compressor. To reach this state, we scanned the angle of the stretcher gratings and optimized the compressor grating distance to achieve the shortest pulses for every set point. The pulse lengths were first measured with the long-range autocorrelator, which could measure the longer pulse lengths far from the optimum. Then the pulses were characterized by the FROG device, which also measures the spectral phase.

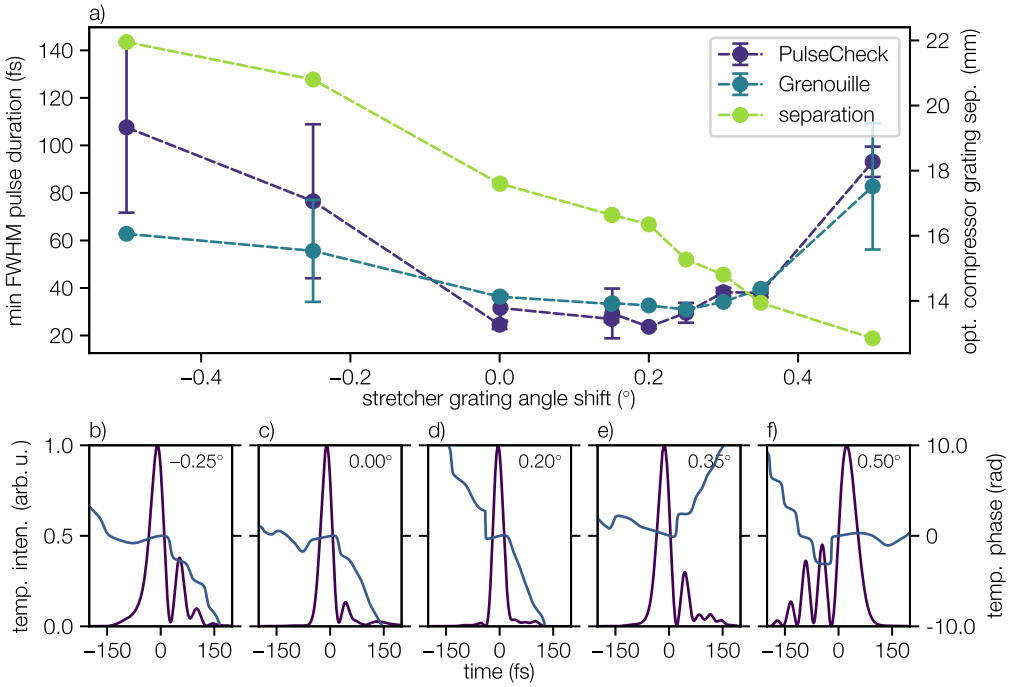

Figure 5.16 – Results of the angle matching procedure: The upper plot shows the pulse FWHM measured with the PulseCheck and the Grenouille for different angle settings and the grating distance at which the minimal pulse length was achieved. The lower plot shows the pulse shape and the reconstructed spectral phase. Courtesy of C. Werle.

In figure 5.16, the measured minimal pulse lengths are displayed for every angle. The grating distance at which it was reached is displayed as well (green). The temporal intensity and the corresponding temporal phases are depicted for five grating angle set points.
The minimum measured pulse length was 29 fs proving that sub-30 fs pulses can be compressed in an OOP MLD compressor. The minimum length was reached 0.2 ° away from the initial set point. This deviation can easily be caused by small inaccuracies due to the mechanical setup.
During the scan of the stretcher grating angles, the retrieved pulse shapes show clear side lobes for the non-fully-compressed pulses. More lobes appear the further away the angle is from the optimum. They originate from the remaining TOD, which is caused by the mismatched grating angles between stretcher and compressor.
Tuning the stretcher angles instead of the compressor grating angles was beneficial for three reasons: First, the acceptance angles of the stretcher grating ($\approx$3 °) are larger than the acceptance angles of the MLD compressor gratings ($<$1 °), providing more tuning range. Second, the geometry of the stretcher conserves the internal alignment under grating angle change. Third, the angular chirp optimization required for ever

input angle setting is easier to perform in the stretcher, since it has only two gratings. While the optimization was performed with the long-range autocorrelator and the FROG device, the optimally compressed pulse was finally characterized with a self-referenced spectral interferometer (SRSI, Wizzler, FASTLITE). The results are shown in figure 5.17. The averaged temporal profile (a) has a width of 25.9 fs, which is close to the Fourier-limit of 25.1±0.3 fs. A statistic of the pulse length over 6000 shots (b) shows that most of the measured pulse lengths lie within 25 and 27 fs and all were clearly below 30 fs. The mean value is 25.9±0.71 fs. The temporal profile, especially in the logarithmic plot (c), shows a small post pulse. This can most likely be improved in the future using a Dazzler. The spectral phase shows a dominantly fifth order error. The modulation over the spectrum hints a fourth-order error as well. This can be expected from the matching error between stretcher and compressor as it can be seen in figure 5.4. The pulse length could be improved in comparison to the previously presented measurement by an optimization of the OPCPA output spectrum.

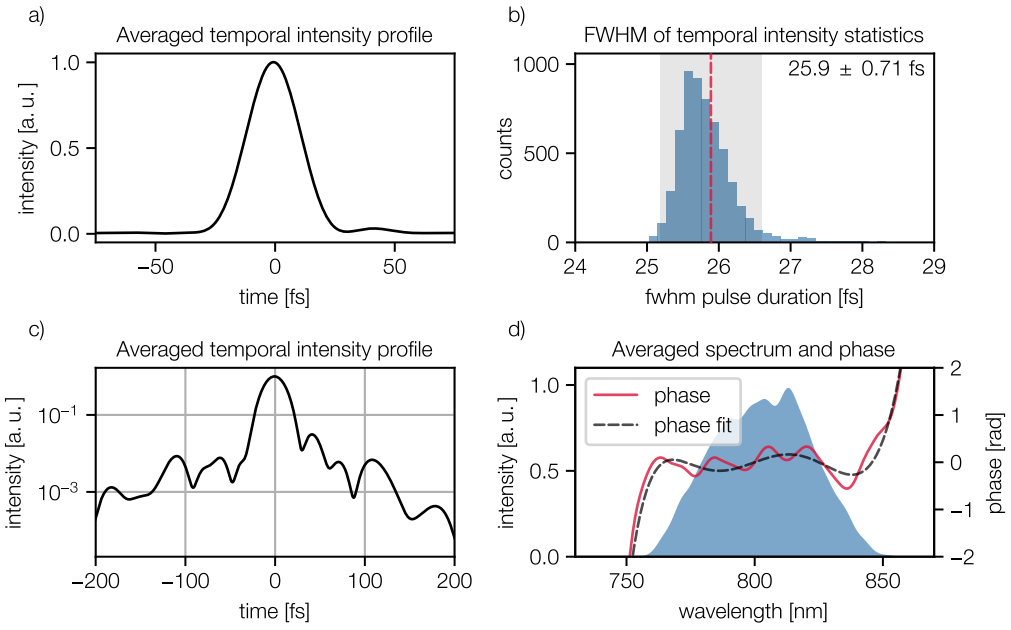

Figure 5.17 – Wizzler measurement of the compressed pulse. Left: Measured temporal intensity profile in linear (a) and logarithmic scale (c); Right: Statistics of the measured pulse duration over 6000 shots (b) and measured spectrum and spectral phase including polynomial fit (d) (adapted from [38])

Apart from the spectral and temporal properties, another concern with OOP MLD compressors is the state of the output polarization. Due to the out-of-plane angle, the polarization changes from a clear s- or p-polarization to a mixed state for the grating. The relative angle between polarization and grating lines depends on the way the OOP angle is introduced into the gratings. According to Smith et al. [92], three

configurations called 'lab', 'pitch' and 'roll' are typically described. Each of them effectively corresponds to a certain rotation angle between the input polarization and the compressor around the beam axis. These angles are marked by the red, dashed lines in figure 5.18. In the 'lab' configuration, this angle is zero. According to Smith et al., the 'lab' configuration is also close to optimal efficiency.

To predict the output polarization state, however, a full simulation of the electromagnetic field in all grating layers is required, which had not been performed, yet. To check the results experimentally, we performed a polarimetry experiment. The experimental setup is shown at the top of 5.18. It consisted of an entrance waveplate for tuning the polarization angle and a polarizer for cleaning the input polarization. After the compressor, another polarizer was placed to analyze the output polarization. During the experiment, the polarization angle ϕ_{in} was tuned within $\pm 10\,^\circ$ with the waveplate. The first polarizer was then optimized for maximum transmission and the energy behind the polarizer was measured at position 'A' as input energy E_{in}. After the compressor, the energy E_{out} was measured at position 'B'. The minimal and maximal achievable energy behind the second polarizer E_{min} and E_{max} were measured as well and the angle of the polarizer for maximum transmission ϕ_{out} was noted.
From this, the following could be calculated: 1. the compressor efficiency $\epsilon = E_{out}/E_{in}$, 2. the polarization angle rotation ϕ_{out}-ϕ_{in} and 3. the polarization contrast E_{max}/E_{min}. In figure 5.18, all three observables are plotted for the scanning range. The efficiency changes slowly with the polarization; within the scanning range it only reduces to 90 % of the maximum transmission. The fit function is $(\mathrm{a}\cdot\sin(2(\alpha\text{-}\alpha_0))+\mathrm{c})^4$ with a, the modulation depth, α_0 the angle of the maximum efficiency and c, the average efficiency. The angle of the maximum efficiency is, however, slightly off from $0\,^\circ$ and closer to the pitch configuration. Another remarkable feature is, that the efficiency, according to the fit parameter a does not drop to zero, but only to around 0.5 ± 0.15 of the peak value. This is in the same range as it was observed by Smith et al. in [92]. For a better conditioning of the fit, a larger scanning range would have been required. The output polarization changes linearly with the input polarization, but since the slope is much smaller than 1, it means the compressor is, to a degree, functioning as a polarizer. The slope of the linear fit is 0.04. However, the linear fit shows an offset of around $-1.3\,^\circ$ in vertical direction, which means the polarization is rotated at zero degree input angle.

The polarization contrast, i.e. the relation between linearly and circularly polarized light, shows a clear maximum at $0\,^\circ$ input angle where the contrast is around 6000:1. It strongly decreases for small deviations from this angle; the full-width half-maximum is only $2.8\,^\circ$. This shows that for polarization-contrast-sensitive applications the compressor should be set up in lab-configuration.

Another important pulse property for laser-plasma acceleration is the temporal contrast. Pre-pulses or a high-intensity before the main peak can pre-ionize the plasma and

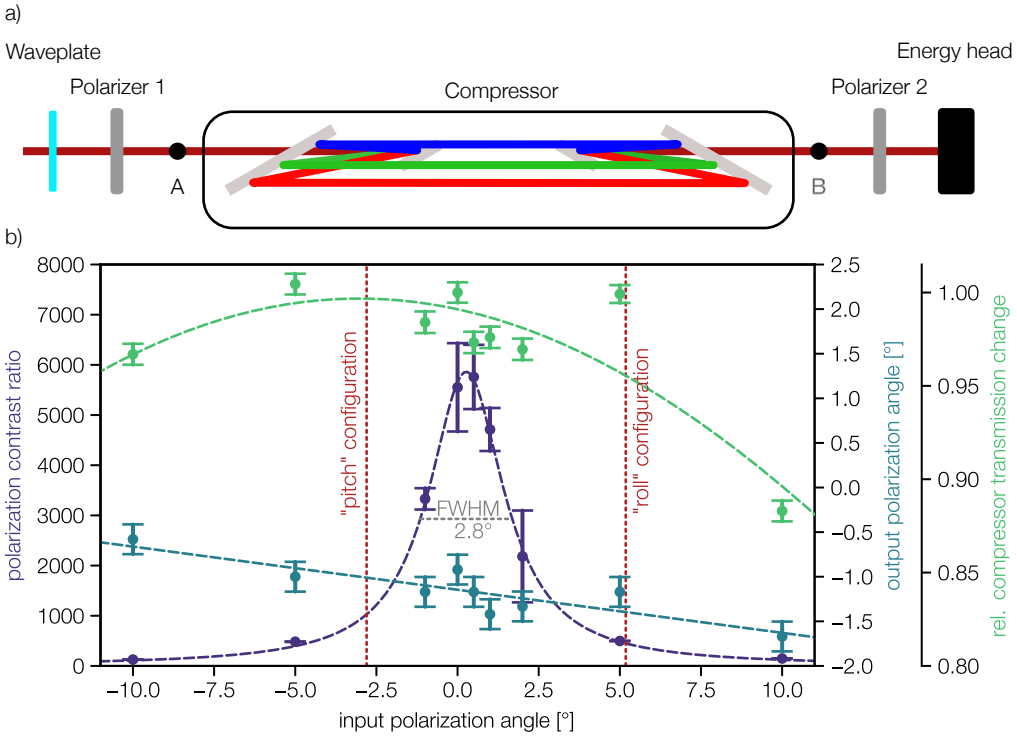

Figure 5.18 – Top view of the measurement setup (top) and results (bottom) of polarimetry experiment of the MLD OOP compressor (adapted from [38])

prevent electron acceleration or reduce the intensity and thus the accelerating field. Post-pulses within a fs-range can disturb the trapped electrons, worsening their properties e.g. divergence. To measure the contrast of the compressed pulses, we used a high-dynamic range third-order autocorrelator (Tundra, Ultrafast Innovation). The result of the measurement is displayed in figure 5.19 (red) and compared to the contrast measurement before the stretcher (blue), which was performed by T. Eichner [36]. The noise level is at $4.1{\cdot}10^{-9}$ for the output pulse contrast measurement, which was the limit due to the relatively low input energy level.

In the range of 100 fs, the contrast was unchanged to the OPCPA contrast. At -100 fs it reaches a level $< 10^{-2}$ (grey, inset). In the range from 100 fs to 10 ps a symmetric 'triangular' signal is visible, which is likely caused by the surface roughness of stretcher and compressor optics which causes high frequency phase noise, that is transformed to temporal noise by the compression [93]. No pre-pulses are visible within the measured range.

The measured contrast levels are comparable to other CPA laser systems for laser-plasma-acceleration and should be sufficient for the electron acceleration [94, 95]. A better surface quality of the stretcher reflective optics, especially the defocusing mirror, could improve the contrast further [96]. In addition, the use of a Dazzler might help

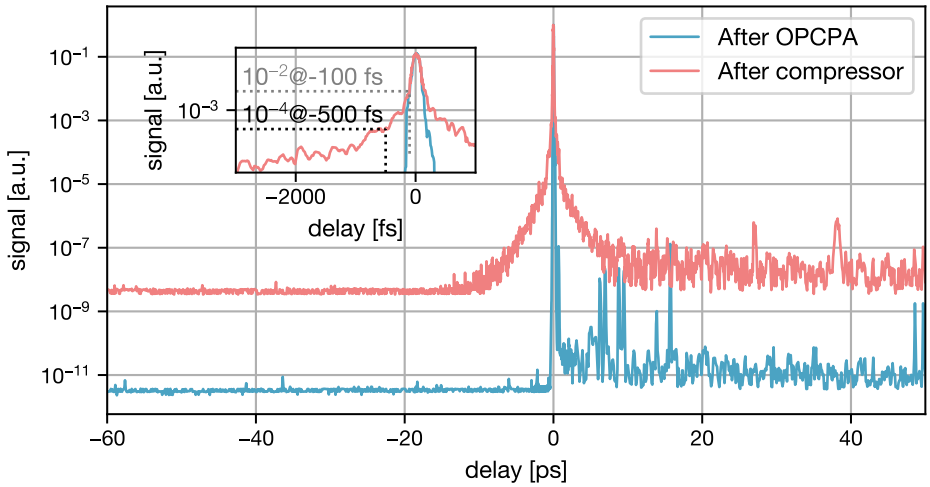

Figure 5.19 – Contrast of the compressed pulse after the compressor in comparison to compressed pulses after the OPCPA laser. Both were measured with a third-order-autocorrelator (Tundra, Ultrafast Innovation). The inset shows a zoom from -3 to 1 ps around the pulse with logarithmic y-scale.

suppress very close post or pre-pulses, that originate in higher-order spectral phase mismatches .

In this chapter, the calculation, planning, setup, alignment and characterization of a pulse stretcher for the KALDERA laser was presented. The necessity of using an OOP MLD grating compressor was explained and the determination of the stretcher parameters to match the compressor and systems's dispersions was described. The alignment and setup of the stretcher was detailed. With the stretcher characterization measurements, it was shown, that the stretcher is suitable for operation in the KALDERA laser system. The temporal stretching followed the theoretical prediction, the spectral efficiency allows for the transmission of sub-30 fs pulse spectra. The mechanical setup proved to be stable over longer times and the beam quality of the OPCPA laser was preserved. Finally, the stretcher was used in combination with an OOP MLD grating compressor to demonstrate pulse compression to sub-30 fs pulses. The spectral phase could be tuned and compression to 25.9 fs was demonstrated. The effect of the input polarization on the efficiency, output polarization and polarization contrast was investigated and the used grating positioning configuration was confirmed to be optimal. The temporal contrast was measured and judged sufficient for laser-plasma acceleration. It can be concluded, that an OOP MLD compressor in combination with a two-grating transmission grating Oeffner stretcher is a suitable choice for the KALDERA laser.

6 A Booster amplifier for the KALDERA laser system

After describing the design, setup and performance of the stretcher for the KALDERA system, the next subsystem, the Booster amplifier, will be discussed in this chapter. In the following, the design, setup and performance of this amplifier will be presented. As it can be seen in the overview of figure 5.1 it is the first amplifier with Ti:Sapphire as gain medium. It is followed by the MERAPI amplifier, which is the first cryogenic Ti:Sapphire amplifier in the amplification chain. The target parameters of the Booster amplifier are given in table 6.1.

Repetition rate	1 kHz
energy	>500 µJ
energy stability (rms)	<0.5 %
central wavelength	790-800 nm
spectral bandwidth	>35 nm, support 25 fs pulses
spatial distribution	Gaussian, round

Table 6.1 – Target output parameters for the Booster amplifier

The purpose of this amplifier is to compensate the energy losses, that are introduced by the stretcher and the Dazzler and to provide a high-quality seed beam for amplification in the following amplifiers. The energy should be sufficient to allow for gain saturation in the next amplifier MERAPI, which is between 0.5-1 mJ, with a repetition rate of 1 kHz. The spectrum should support 25 fs pulses, for a Gaussian spectral shape, this would require a FWHM bandwidth of 35 nm. The mean wavelength should be around 800 nm as this is the design wavelength of the KALDERA laser system. It should rather be slightly blue-shifted, to compensate a possible red-shift of the spectrum in the later amplifiers. The spatial profile of the output beam should be as round as possible, to ease the optimization of the overlap of pump and seed in the following amplifiers, and have a smooth, Gaussian distribution. The goal of the following section is to define amplifier parameters and a design, that enable these output parameters. The amplifier parameters, that will be discussed are: the pump energy and an adequate pump laser, the crystal length and doping, the beam diameter and the number of passes.

6.1 Amplifier design

6.1.1 Pump laser requirements

From the target output parameters, the required specifications of the pump laser for this amplifier can already be deduced: It should be pulsed with a repetition rate of 1 kHz. The wavelength should be within the absorption spectrum of Ti:Sapphire, which ranges from around 450-620 nm as discussed in section 3.4.3 and shown in figure 3.9. The minimum required pulse energy from the pump laser is estimated from the target output energy and an estimation of the expected pump efficiency. This is described in equation 6.1.

$$E_{pump} \geq \frac{E_{out}}{\eta_{abs} * \eta_{QD} * \eta_{QE} * \eta_{geo}} \tag{6.1}$$

E_{out} is the target output energy, η_{abs} is the absorbed fraction of the pump, which is determined by the doping concentration and the crystal length as will be discussed later and should be $\geq$90 %. η_{QD} describes the efficiency, that is caused by the quantum defect, the energy difference between a pump and a seed laser photon. It can be calculated according to 3.17 as η_{QD}= 500 nm / 800 nm = 0.625. η_{QE} is the quantum efficiency, which gives the portion of excited atoms, that can actually take part in the lasing process and is in the range of 80 % in Ti:Sa at room temperature [97]. η_{geo} is the amplification efficiency, that derives from the geometrical overlap of pump and seed in the crystal. The exact value of η_{geo} strongly depends on the actual setup and beam sizes and should reach at least 80 % in the later setup. From this estimation the theoretical minimum pump energy is 2.5 mJ, to reach 1 mJ of output energy. More effects like losses from the used optics and the crystal coatings could be included. The pump energy should be provided with an energy stability at least as good as the target output energy stability of 0.5 % rms.

We finally chose to use a Revolution 20 from Coherent as pump laser. It is a frequency-doubled Nd:Ylf laser, that emits 220 ns pulses with 527 nm wavelength, a pulse energy of up to 15 mJ at 1 kHz repetition rate. Its rms energy stability is specified as <0.5 % [98]. We measured an energy stability of <0.2 %. The beam intensity distribution in the near-field (left) and in the focus (right) is shown in figure 6.1. The near-field distribution shows a slight ellipticity, the vertical line-out profile shows a flat-top beam, while the horizontal shows an increased intensity in the center. The focus is slightly elliptic in the other direction, but the lineouts are closer to Gaussian beams. A measurement of the M^2 gives a value of around 26 and 33 in the horizontal and the vertical axes. The pump beam size in the amplifier crystal will be discussed later as well as the required optical setup.

After choosing a pump laser, more parameters need to be decided on, to ensure the target output parameters are met. These are: the beam diameter, the crystal length and

Repetition rate	1 kHz
energy	15 mJ
energy stability (rms)	<0.5 %
central wavelength	527 nm
pulse duration	220 ns
M^2	around 30

Table 6.2 – Specifications of the Revolution 20 pump laser

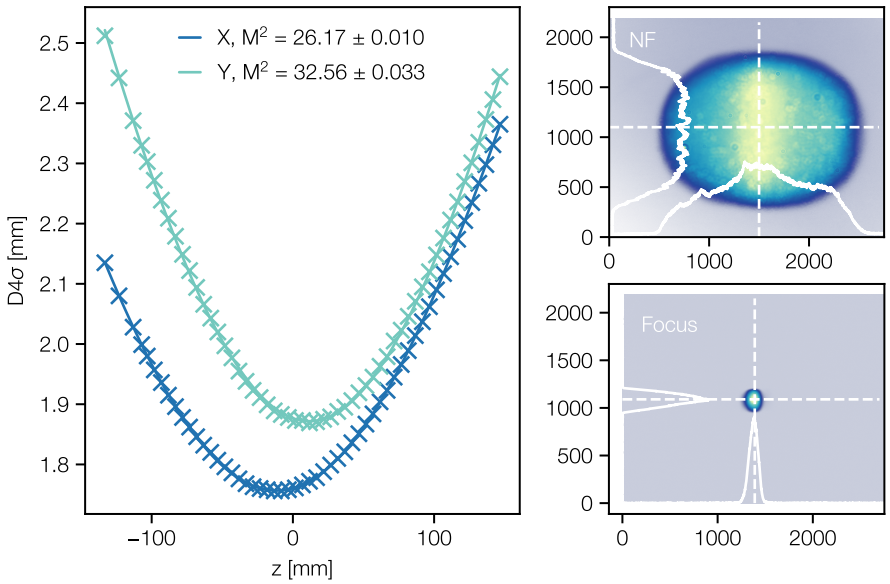

Figure 6.1 – Beam quality factor (M^2) measurement and beam intensity distribution in the near-field (top right) and focus (bottom right) of the Revolution20, which will be used as pump laser.

doping concentration and the number of passes the seed takes through the amplifier. In the following, all of them will be discussed in detail after a few general considerations.

A multi-pass amplifier configuration was chosen for the setup implementation. Due to the moderate average pump power of <15 W, a cryogenic cooling approach was not considered, as water cooling should cool the crystal sufficiently, which will be confirmed in sub-section 6.1.4. The pump and seed beam diameter greatly influence the amplification dynamics and are also relevant for the selection of the crystal properties, thus they will be discussed first. The evaluation will be based on 1D Frantz-Nodvik gain calculations, that do not require knowledge about the exact crystal parameters as the spatial distribution of the gain within the crystal and pump-seed-overlap are neglected in the first step. These effects will be partially taken into account during the discussion of the crystal parameters and later a full 3D simulation will be performed,

Pump energy	15 mJ·η_{pump}= 6 mJ
Seed energy	8.8 µJ
Passes	5
Saturation fluence	0.6 J/cm^2
Input beam diameter	0.5-1 mm

Table 6.3 – Parameters of Frantz-Nodvik based gain calculations.

to confirm the expected output parameters. Even this simplified approach should provide meaningful insight into the amplification dynamics and enable choosing a suitable beam diameter.

6.1.2 Gain calculation

From equation 3.19, it is clear, that the beam diameter greatly influences the amplification dynamics. Thus, to reach the target output parameters, the output energy and fluence in dependence of the beam size need to be determined. In a first approximation, this was done based on the Frantz-Nodvik equations, as they were presented in 3.4.3. Spatial, temporal or spectral effects were not yet considered here, which means round, flat-top beams with perfect overlap were assumed. Time was not resolved, but the whole pulse energy was assumed to arrive instantaneously and the wavelength was set to 800 nm.

The assumptions for the simulation are given in 6.3: The pump energy, as described earlier, was 15 mJ. To account for absorption, quantum and geometrical efficiency the pump energy was multiplied by the minimal expected efficiencies η_{abs},η_{QE} and η_{geo} that were defined earlier. The seed energy was estimated to be 8.8 µJ which results from: a) the expected output of the OPCPA front-end, 55 µJ, b) the measured transmission of the stretcher 40 % and the estimated transmission of the AOPDF, which is around 40 %. The resulting beam energy was calculated for every pass, up to 5 passes. The results of the diameter scan are shown in figure 6.2. The left plot shows the output energy for every beam diameter and each pass. The target minimum output energy of 500 µJ is marked by a red, dashed line. This energy is reached by all tested beam diameters within four passes. The energy saturates at around 6 mJ, which matches the expected available energy, based on the efficiency that was estimated with equation 6.1(15 mJ/2.5). The right y-scale gives the overall gain for every point. The maximum gain is >600, which is much larger, than in the later amplifier stages. The scan shows that the beam diameter influences how fast the output energy reaches the maximum energy.

The right plot shows the corresponding fluences. The dotted line at 0.6 J/cm^2 marks the saturation fluence of Ti:Sapphire. In literature different values can be found for

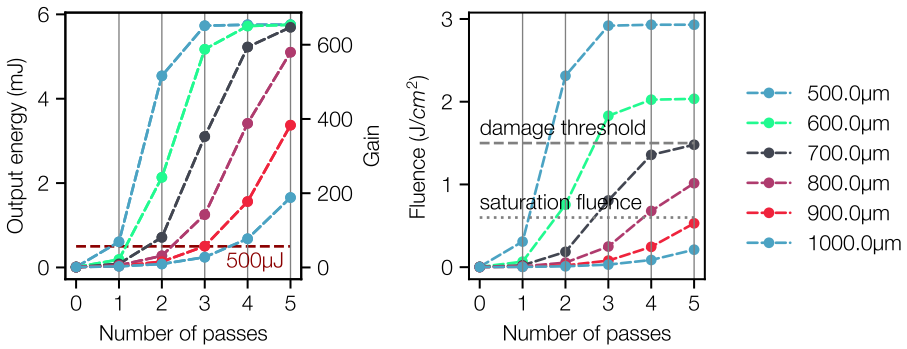

Figure 6.2 – Results of the 1D Frantz-Nodvik gain simulation. The output energy (left) and the corresponding fluence (right) were calculated for different beam diameters for up to 5 passes through the amplifier, assuming 8.8 µJ of seed and 15 mJ pump energy with 90 % of absorption. The target energy (red, dashed line) saturation fluence (dotted line) and the damage threshold (dashed line) of the mirrors and crystal are marked.

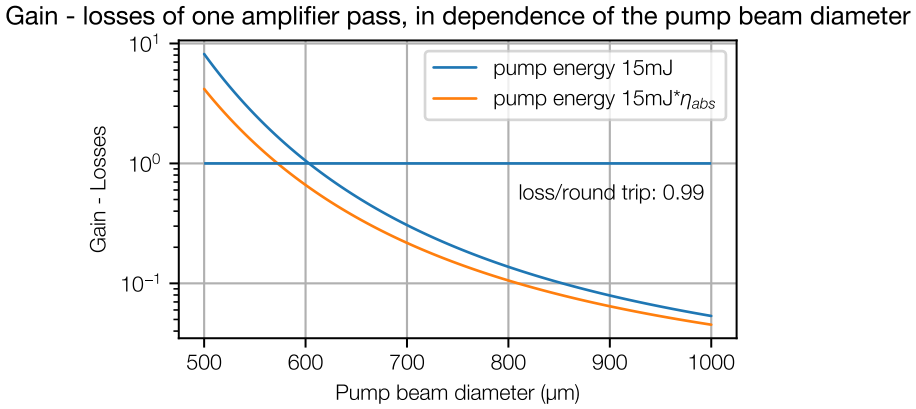

Figure 6.3 – Gain for a free-run laser in the Booster with full pump absorption in dependence of the pump beam diameter.

the saturation fluence of Ti:Sa [99, 100]. From comparison between our Frantz-Nodvik simulations and the parameters of the amplifiers at the ANGUS laser system (4), we found, that a fluence of 0.6 J/cm^2 yields the most fitting results. The dashed line at 1.5 J/cm^2 marks the estimated damage threshold of the mirrors and the crystal coating for 600 ps pulses. For safe operation the fluence should be well below this value.

As the gain is relatively high in the amplifier, it should be checked, if the threshold for a free-running laser is met. This threshold is met when the gain of one pass through the gain medium exceeds the 'losses' at the end surface. For an exemplary

AR-coating at the crystal end face of <1 % reflectivity, a gain of 100 would be required for free-lasing.

To better understand this limitation, the longitudinal gain was calculated for different beam diameters, once, assuming 100 % absorption of the pump energy and once including an absorption efficiency of 90 %. From this gain, the losses at the crystal end face were subtracted. The results are plotted in figure 6.3. The threshold for lasing is marked with a blue line.

The plot shows, that below 600 µm beam diameter a free run laser is probable for the current pump energy. This should definitely be avoided for several reasons: First, it can compromise laser amplification with the seed pulse. Free lasing would start immediately when the pump pulses arrived, while the seed usually has a small delay. This means free-lasing could already deplete some gain in the crystal and thus reduce the available gain for the seed. Second, even slightly below the free-lasing threshold, the level of amplified-spontaneous emission (ASE) is relatively high, which worsens the contrast of the pulse [101] Third, it poses a risk for the following amplifiers. If no seed is sent to the crystal, while the pump laser is running, a free-running laser could eventually propagate to the following amplifier stage and be amplified. As its beam properties, such as spatial mode, spectral intensity and pulse length, are unknown it could lead to damage in optical components, e.g. the laser crystals. Concluding it can be said that to avoid a free-run laser and to suppress ASE, the beam diameter should be >700 µm. As the amplification simulations show, that the target energy can be reached with this beam diameter within 2-3 passes, this beam diameter seems suitable. In the following, a beam diameter of 800 µm will be assumed. Its suitability will be confirmed in the following considerations.

6.1.3 Crystal parameters

The investigation of the behavior of the amplification and free-lasing gain in dependence of the beam diameter allowed to find a suitable beam diameter. We are now in a position, to discuss the crystal parameters crystal length and doping concentration next. Both parameters mainly influence the absorption and geometrical efficiency, whose target values of of η_{abs}=0.9 and η_{geo}=0.8 were given earlier.

For choosing the crystal length l_{crys} and doping concentration, several considerations can be made. In Ti:Sa crystals doping concentrations between 0.03-0.25 % are commonly available, which corresponds to absorption coefficients α between 0.6 and 4.1 cm^{-1}. A measure for the crystal quality is the figure of merit (FOM), which is measured as $\eta_{abs}(pump)/\eta_{abs}(seed)$. A low FOM causes unwanted reabsorption in the lasing wavelength, which leads to heating of the crystal [102]. Crystals with higher absorption coefficients often have a lower FOM, which motivates the use of lower

absorption coefficients. Typical values for FOMs are 100-300. As the seed energy is already rather low, the absorption of the seed by the crystal should be as low as possible. Crystals with a FOM of 300 are available for $\alpha < 2.1\,\mathrm{cm}^{-1}$, so this will pose an upper limit for the absorption coefficient.

Another reason to use a lower absorption coefficient is that it increases the longitudinal homogeneity of the absorbed energy inside the crystal. This benefits the heat extraction from the crystal in a side-cooled setup, as well as the amplification efficiency. The higher the absorption coefficient, the more energy is absorbed in the first millimeters. Another way to improve the homogeneity is to pump the crystal from two sides.

To find the minimal possible absorption coefficient α, the absorption efficiency η_{abs} needs to be calculated. It depends on α as well as on the crystal length and is given by the Beer-Lambert law of absorption [103]. In figure 6.4 (top) the absorbed pump fraction in dependence of the crystal length for different absorption coefficients is plotted. As expected, the longer the crystal and the higher the absorption coefficient, the higher is the absorption efficiency. For α=1.60 cm^{-1} the target 90 % absorption is only reached for crystal length >1.5 cm. For α=2.1 cm^{-1} the crystal length should be >1.2 cm.

Another consideration that plays an important role in choosing the crystal length is the geometrical overlap between pump and seed. For longer crystals the overlap between pump and seed reduces, because of the typically non-collinear overlap between seed and pump. For a symmetric beam profile, often, pump and seed beam are arranged such, that they cross in the middle of the crystal. This reduces the amplification efficiency, especially because the pump absorption is highest in the end faces. The geometric efficiency η_{geo} derived from this non-collinear overlap is plotted in dependence of the crystal length for 1 and 2° angle between pump and seed in the middle plot of 6.4. These angles are already small for a multi-pass amplifier but as it can be seen in the plot, already reduce the efficiency by >10 % for all considered lengths for an 800 µm beam diameter.

To chose an optimal crystal length both the absorption coefficient and the pump-seed overlap have to be considered. Both have an influence on the pump efficiency. Thus, to find the optimal crystal length, the absorption efficiency η_{abs} and the efficiency arising from the geometrical overlap η_{geo} can be multiplied. The resulting efficiency in dependence of the crystal length is plotted in the bottom plot of figure 6.4. For both angles the middle of the scanned crystal lengths seems to be favorable. With an absorption coefficient of 1.85 cm^{-1} in a 15 mm crystal an efficiency of >74 % can be reached with a 2 ° incidence angle. This should be suitable to reach the desired amplification. A reduction of the incidence angles would improve the efficiency further.

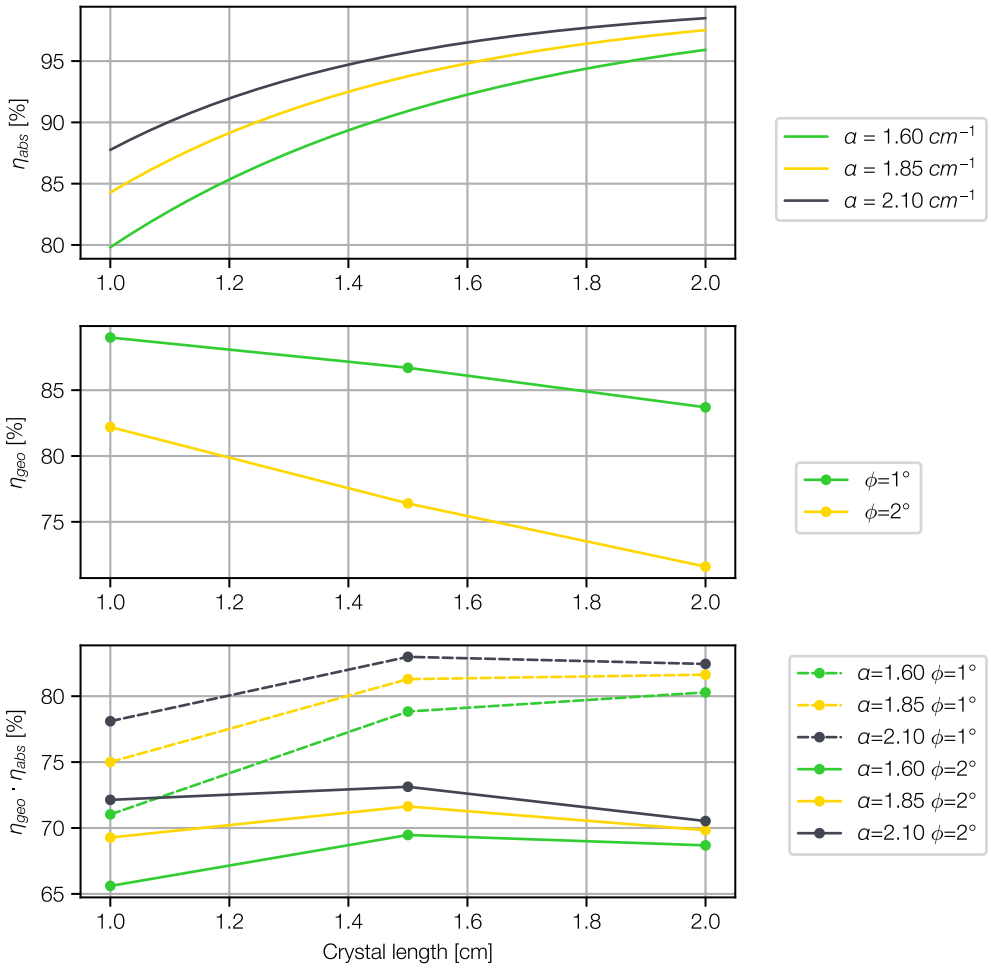

Figure 6.4 – Top: Calculated pump absorption efficiency in dependence of the crystal length for different absorption coefficients α. Middle: geometrical overlap efficiency between seed and pump in dependence of the crystal length for two incidence angles ϕ. Bottom: Combined efficiency from absorbed energy and geometrical overlap for different absorption coefficients and incidence angles.

The last consideration regarding the crystal parameters is the discussion of the transverse gain. In many amplifiers transverse amplification or even lasing leads to unwanted gain depletion, similarly as it was discussed before for a longitudinal free-running laser. To check if this could be the case in this amplifier, the transverse gain was calculated according to equation 6.2 from [104].

$$G_{trans} = exp\left(\alpha \cdot d \cdot \frac{F_0 \nu_{las}}{F_{sat} \nu_{pump}}\right) \tag{6.2}$$

The parameters are: F_0, the initial fluence on the crystal surface, F_{sat}, the saturation fluence of Ti:Sa, for which we used $0.6\,\mathrm{J/cm^2}$. ν_{las} and ν_{pump}, the laser and pump frequency and the beam diameter d. For the previously given beam and crystal parameters, the expected maximal transverse gain is 1.6, which is orders of magnitude smaller, than the longitudinal gain and should thus be negligible.

So far, the crystal parameters were discussed and an absorption coefficient of $1.85\,\mathrm{cm^{-1}}$ and a crystal length of 15 mm was chosen. The final crystal diameter was set to 6 mm, as it was well available and offers a sufficient aperture for the beam. With this knowledge, the thermal behavior of the crystal, primarily the resulting thermal lens, will be studied next. The influence of the beam diameter and pump power on the thermal lens will be investigated with simulations in the finite-element modeling program COMSOL and measurements.

6.1.4 Thermal lens simulations and measurements

In addition to the gain, the second aspect to consider for the beam diameter is the thermal behavior of the crystal. This becomes clear in the analytic expression for the thermal lens, that is caused by the thermally-induced change in refractive index [105]:

$$f^{-1} = \frac{\delta n/\delta T}{2\kappa A} P_{heat} \tag{6.3}$$

It includes the material constants $\delta n/\delta T$, the thermo-optic coefficient, which describes the change of the refractive index with temperature, as well as the thermal conductivity κ, the absorbed power P_{heat} and the beam area A. So, apart from the material parameters, the thermal lens depends on the beam size and the pump power. The simulations and measurements, that will be presented in the following confirm this.

While the temperature-dependent refractive index change is the dominant effect for Ti:Sapphire [106], more phenomena are usually combined under the term thermal lens. All are caused by the pump power that is absorbed in the crystal and affect the wavefront of the seed beam. They are listed in the following [106]:

- Bulging of the end faces of the crystal due to the thermal expansion of the crystal: As the pump is often absorbed along the central axis of the crystal, this is where it heats up most. Consequently, the longitudinal expansion is largest in the central area of the crystal, which leads to curved end faces. These act like the curved surfaces of a lens.
- Photoelastic effect : The optical pumping of the crystal causes stress in the crystal structure. This leads to a change of the refractive index and thus to lensing. This effect has a thermal and a non-thermal contribution [107, 108]

For collinear, or close to collinear propagation of seed and pump, as we have in this amplifier, the mainly radially symmetric temperature profile leads to a change in wavefront curvature, which equals the effect of a lens. With larger angles or temperature distributions with other than rotational symmetry along the z-axis, other wavefront deformations such as tilt or astigmatism can become significant as well.

Using the material constants for room temperature from table 6.4, a beam diameter of 800 µm and a heating power of $P_{Pump} \cdot \eta_{abs}$=15 W·0.93, assuming all absorbed pump power is contributing to heating of the crystal, the focal length of the thermal lens would be <200 mm, according to equation 6.4. This is a strong thermal lens in the sense, that its effect will be noticeable within the propagation inside the amplifier setup, making it non-negligible. Thus, the thermal lens has to be accounted for in the design of the Booster.

Equation 6.4 considers only a 2D transversal thermal distribution and no cooling. It does also not include any thermally-induced stress effects such as bulging. To account for these thermal effects, we decided to perform thermal lens simulations with the finite-element simulation software COMSOL and perform a measurement of the thermal lens, which will be described in the following.

The thermal lens simulation and measurement were performed in cooperation with Dr. J. B. Gonzalez Diaz.

To model the effect of the thermal lensing on the seed beam different calculation modules of COMSOL have been used. In the first step the multiphysics module 'Heat transfer with radiative beam in absorbing media' has been used to model the absorption of the pump and the resulting temperature distribution inside the crystal. The crystal was modeled as cylinder. The temperature dependent material properties refractive index n, thermal conductivity ϵ_{TC} , thermal expansion coefficient ϵ_{TE} and thermo-optic coefficient ϵ_{TO} were extracted from [109, 110]. For room-temperature these values are listed in table 6.4.

The crystal cooling was simplified by assigning a fixed temperature of 20 °C to the outer surface of the crystal, which imitates the ideal case of perfect cooling of this surface with a 20 °C coolant. For the optical pumping two different configurations were studied: pumping from one side and from two sides with evenly split pump power. Accordingly, the optical pumping was realized by initializing either one or two circular power sources of a total power of 15 W with a dedicated diameter d_p at one or both end faces of the crystal. The power is absorbed in the crystal, according to the set absorption coefficient. The power source provides a continuous pumping power and an equilibrium thermal profile of the crystal is reached, especially in transverse direction,

property	value
refractive index n	1.76
Thermo-optic coefficient $\delta n/\delta T$	13*10^{-6}/K [106]
thermal conductivity κ (room temperature)	33 (W/K*m) [106]
thermal expansion coefficient (room temperature)	5*10^{-6}/K [106]
absorption coefficient α	1.85 cm^{-1}

Table 6.4 – Material properties of (Ti:)sapphire for COMSOL thermal lens simulations

between the pumped region and the cold, outside surface. According to literature, the temporal constant of changes in the temperature distribution in Ti:Sa is in the range of 0.5 s [111]. As this is much larger, than the time between two pump pulses (1 ms), it can be assumed, that a thermal equilibrium is reached in the crystal.
The results of the calculated temperature distributions are given in figure 6.5 for a beam diameter of 800 µm. It can be seen, that the crystal temperature only rises to around 35 °C, which is acceptable. The temperature distribution is used as base for the calculation of the temperature dependent properties, especially the refractive index, which are updated accordingly.

To deduce the thermal lens from this, the COMSOL module 'Geometrical optics' is utilized. In this, a set of rays is initialized in front of the crystal with the previously calculated refractive index profile and propagates through it. The effect of the thermal lens then shows in the propagation after the crystal, where the beam size over the propagation length, could be extracted from the ray-tracing. The focal length of the thermal lens was determined as the distance between the crystal and the minimal beam diameter.

The simulation was performed for beam diameters of 550, 800 and 1100 µm and for the two different pumping schemes, pumping from one and pumping from two sides. The resulting thermal lenses are displayed in figure 6.5. A parabolic curve was fit to the simulation results, as this is the behavior that would be expected from the analytical formula.
The simulated focal lengths of the thermal lens are about double as long as the ones retrieved from the analytical formula. One explanation could be, that the COMSOL simulation is taking cooling into account, which reduces the temperature and the temperature gradient and thus the thermal lens. As no cooling is considered in the analytical formula the resulting thermal lens is stronger.

The simulations confirm that the bigger the beam size the weaker is the thermal lens. Pumping from both sides leads to a slightly weaker lens, than pumping from one side

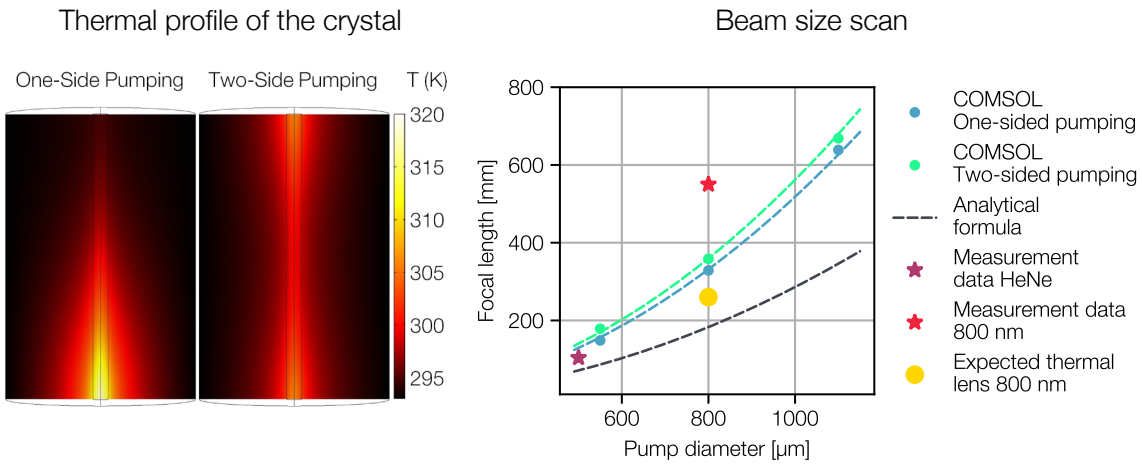

Figure 6.5 – Results of the thermal lens simulations with COMSOL: Focal length of the thermal lens in dependence of the pump beam size (left) for 15 W pump power. A x^2 fit is added to the simulated data as well as the results from the analytical formula. Experimental results, that are discussed later, are added for comparison. Two exemplary simulated thermal profiles of the pumped crystal for one- and two-sided pumping (right) for an 800 µm diameter beam are shown.

and should thus be implemented in the amplifier design, to reduce the thermal lens as much as possible. The simulations suggest, that for beam diameters smaller than 1 mm the thermal lens focal length will be below 0.6 m.

To visualize the effect of different thermal lenses on the beam caustic, the resulting change of beam size for a 800 µm diameter collimated beam is displayed in figure 6.6. For the thermal lenses of the expected range, the propagation length at which the beam diameter changes for more than 10 % is $\leq$75 mm. As the gain simulations showed, more than one pass is required for reaching the target energy, hence some shaping of the beam size between the passes has to be implemented within the amplifier setup, to keep the beam inside the amplifier crystal at the desired beam size. In addition, the beam size on every optic has to be carefully checked, as the beam diameter is going to change throughout the amplifier and potentially fluences above the damage threshold of optics can be reached.

To check the simulation results, we performed a measurement of the thermal lens. The idea was to excite the crystal with the pump laser, which is also used in the later amplifier. This creates a thermal distribution and a thermal lens, which is then probed by a Helium-Neon-laser (HeNe; HNL210L, Thorlabs), that is sent through the crystal. The crystal was wrapped in indium foil and placed in a copper mount, which was water cooled, the water temperature was 21 °C.

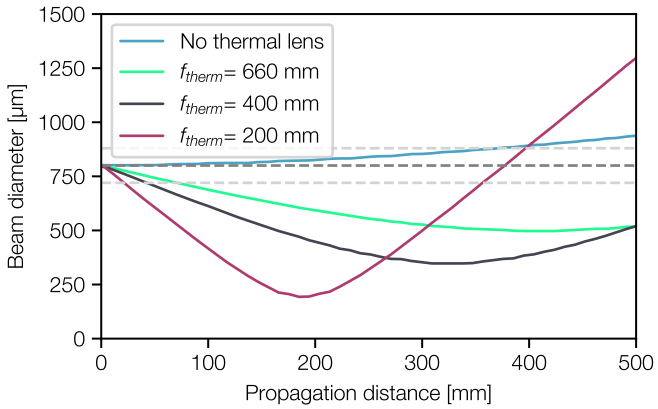

Figure 6.6 – Beam caustic of a 800 µm diameter beam, which is focused by lenses of different focal lengths.The initial beam size of 800 µm and a 10 % change of the beam size are indicated by dashed lines.

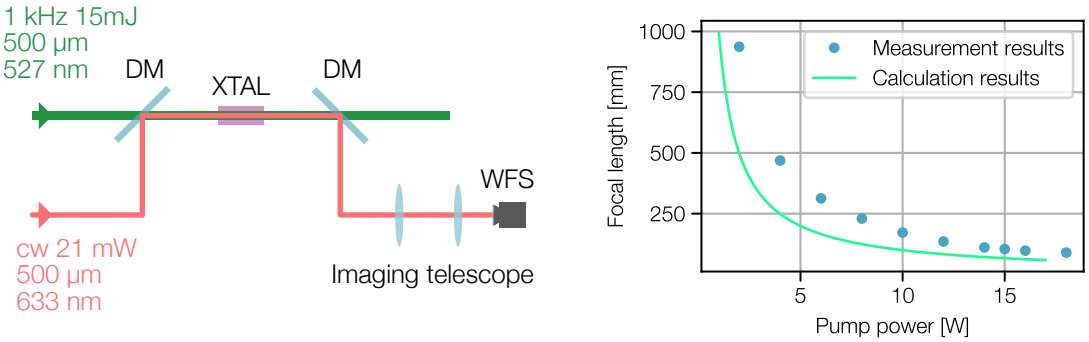

Figure 6.7 – Left: Experimental setup of the thermal lens measurement. A HeNe is used to probe the pumped XTAL crystal. The thermal lens is measured by measuring the change of the wavefront. Right: Measured and calculated focal lengths of the thermal lens, for different pump powers.

The effect of the thermal lens on the HeNe is measured by measuring the change of its wavefront, depending on the pump power. The setup is shown in figure 6.7. The utilized HeNe laser emits at 633 nm, where almost no absorption or amplification happens in Ti:Sa (see figure 3.9). Thus, just the thermal lens in the crystal may affect the probe beam. For optimal overlap inside the crystal, the pump and the HeNe laser are combined on one axis with dichroic mirrors, that reflect the HeNe and transmit the pump light. The pump beam, with 500 µm beam diameter, is sent into the crystal from one side and most of it is absorbed in the crystal. The HeNe passes the pumped crystal, where it is affected by the thermal lens, which changes the wavefront. It then passes through a telescope, which images the beam at the exit plane of the crystal onto a wavefront sensor (HASO4, Imagine optics). The wavefront software performs a modal reconstruction of the wavefront using Zernike polynomials as bases. The Zernike

polynomial coefficient C_3 gives the amount of the defocus, which can be related to the focal length of the thermal lens via equation 6.4 with R_{mes}, the measured radius of curvature of the wavefront and r_p, the pupil radius over which the wavefront is evaluated [112].

$$R_{mes} = \frac{r_p^2}{4C_3} \tag{6.4}$$

For 15 mJ pump energy the focal length of the thermal lens was measured to be 104 mm. This is around 20 % shorter, than it was predicted in the simulations (compare figure 6.5). Several effects could lead to this. First, the real experimental setup could increase the thermal lensing. Thermal stress could be added by the mounting of the crystal and the cooling might not be perfect, e.g. the thermal contact to the copper mount could be impaired. This would lead to a slightly higher temperature or temperature gradient.

Second, the photo-elastic effect is not considered in the COMSOL simulation. Measurements by [107] and simulations by [106] hint that the photo-elastic effect could affect the thermal lens to some degree in Ti:Sa. The presented simulations and measurements suggest that the thermal lens has to be taken into account in the planning of the amplifier setup.

In this section, the pump laser parameters, the beam and crystal parameters were estimated, that are necessary to reach the target output beam parameters. The gain dynamics, the efficiency and the thermal behavior of the crystal were investigated in dependence of the beam and crystal parameters. Specifically, the output energy, the free-lasing gain and the thermal lens were considered, all of which highly depend on the beam diameter. To reach the highest output energy with as few passes as possible, the beam diameter should be small, but >600 µm, to prevent free-lasing. The thermal lens reduces with larger beam diameters, which makes it easier to handle and compensate. A larger beam diameter is also less sensitive to pointing and position changes. The beam diameter of 800 µm was finally chosen, as the target energy of 1 mJ can still be reached within 3 passes, which simplifies and eventually shrinks the geometrical setup. The beam diameter is however as big as possible to relax the thermal conditions and positional precision requirements. In addition, the gain should be well below the free-lasing threshold.

So far, the decision on the beam parameters were based on, 1D Frantz-Nodvik calculations. To confirm, that the target parameters are still met, when spatial, spectral and temporal effects are included, the next step is the simulation of the amplifier stage in a 3D program.

6.1.5 3D simulations with CommodPro

To confirm the simulated output energy of >500 µJ after three passes for a 800 µm beam, another simulation was performed with the commercial software CommodPro [113]. In this simulation the measured pump beam profile is used and the beam propagation through the crystal in 3D is considered. The bow-tie amplifier geometry is introduced, to simulate the realistic spatial overlap between pump and seed beam. In addition, the beam profile and output spectrum can be analyzed, to see if any noticable effects occur.
The simulation parameters are listed in table 6.5 and correspond to the target parameters in the later setup. The simulation is split in two parts: In the first part,

Pump energy	15 mJ
Doping concentration	0.1 %
Crystal length	15 mm
Seed energy	8.8 µJ
Passes	3
Saturation fluence	0.6 J/cm^2
Input pump and seed beam diameter d4σ	0.8 mm
Input angles	pass 1 and 2: 2 °; pass 3:0 °

Table 6.5 – Parameters of CommodPro amplifier gain simulations.

the pump beam propagation and absorption by the crystal is simulated. From this simulation the gain distribution can be exported. This distribution is introduced to the crystal in the amplification simulation. In this second simulation the propagation and amplification of the seed beam is calculated.
For the simulation of the gain, the measured focused beam profile of the pump laser was used. Collinear pumping from both crystal sides was implemented. For the amplification simulation, three passes through the amplifier were simulated. The beam was passing the crystal with 2 ° input angle in the first two passes, under 0 ° in the last pass. The seed beam profile was circular and Gaussian, as this is the target for the real beam profile as well.
To simulate a 800 µm beam diameter for all three simulated passes, no thermal lens was added in the simulation. The effect of natural divergence was avoided by implementing a short beam path. This seems a valied approximation as the beam size will be adapted for every pass in the later setup.
The output energy after every pass is plotted in figure 6.8. The final output energy is 759 µJ, which is well above the target energy. The amplification reaches saturation in the third pass, hinting an efficient depletion of the gain in the crystal. The simulation allows to analyze the depletion of the gain in the crystal, which is shown in figure 6.9. The gain after the last pass is clearly reduced, especially in the center region, compared to the previous ones. In general, the pump profile is slightly elliptic, as it

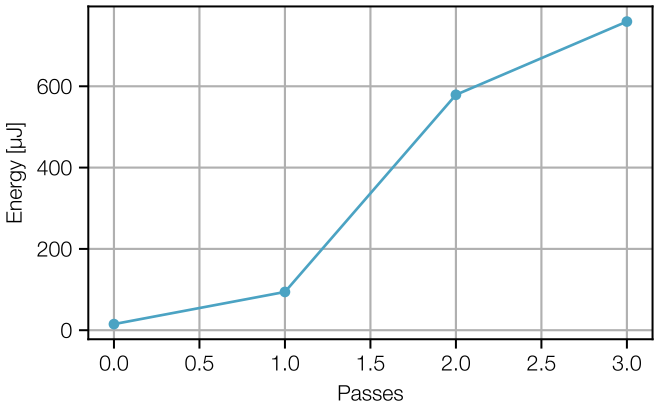

Figure 6.8 – Output energy after every pass in the CommodPro simulation of the Booster. The input energy was 15 µJ, the pump energy was 15 mJ.

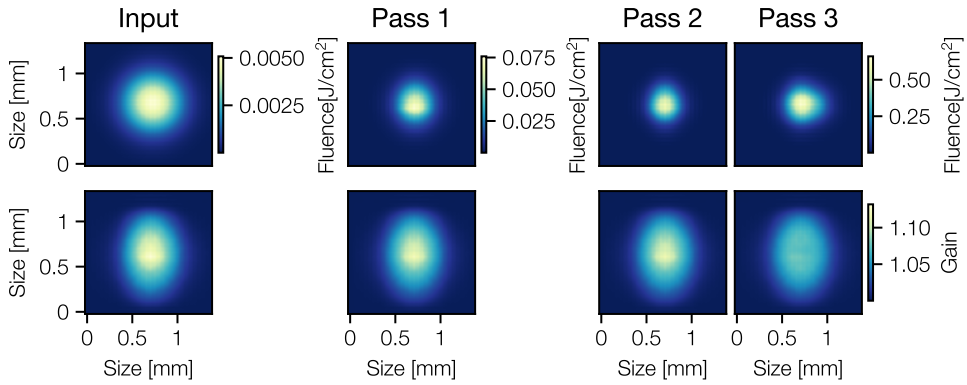

Figure 6.9 – Top: Output beam fluence before amplification (left) and after pass 1-3. The colorscale of the fourth pass is valid for the third as well. Bottom: Gain in the middle layer of the crystal before amplification (left) and after pass 1-3. The colorscale is valid for all four images.

can already be seen in the focus in 6.1.

The beam fluence after every pass, shown in the top row of 6.9, shows, that the beam size is strongly reduced during amplification. The higher fluence in the center of the seed beam, leads to a higher gain, which effectively leads to a narrowing of the spatial intensity distribution. The higher intensity in the center of the pump beam enhances this effect. In the fluence profile after pass 3, a slight asymmetry can be noticed in the horizontal axis. The feature could originate in a slight misalignment between seed and pump, leading to a non-symmetric overlap. This can be avoided in the real amplifier, by checking the amplified beam profile during optimization of the seed alignment.

The simulation results confirm that the planned input beam of 800 µm diameter can be amplified to >500 µJ within three passes in a bow-tie amplifier geometry, using the measured pump beam profile. The amplified beam profile is significantly smaller, than

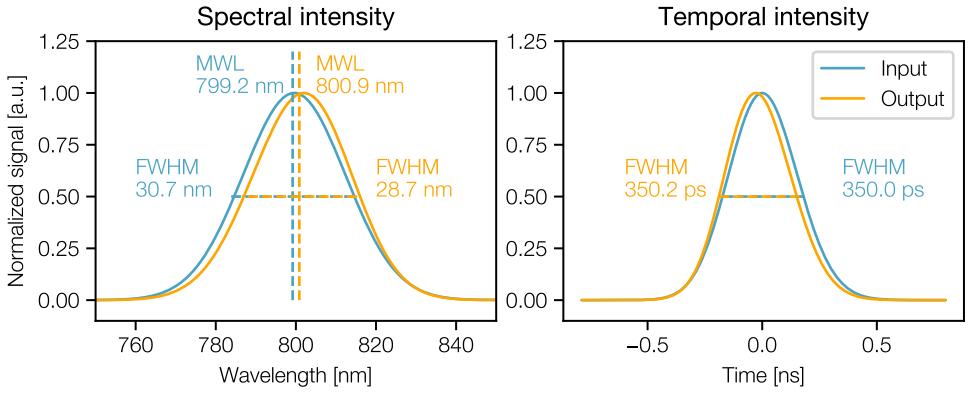

Figure 6.10 – Spectral (left) and temporal (right) intensity before (blue) and after (orange) the amplification. The mean wavelength (MWL) and FWHM of the spectra were calculated. The amplification causes a red-shift and a narrowing of the spectrum. The width of the temporal intensity increases slightly.

the input beam. This effect has to be considered in the mode-matching of the real amplifier. This can be compensated by the same beam shaping that is planned to account for the thermal lens.
The 3D simulation allows for a simulation of the spectral and temporal intensity and its change during amplification. The results of this simulation are shown in figure 6.10. The simulated spectrum was narrowed by 2 nm and red-shifted by 1.7 nm during amplification. If this effects leads to a too narrow output spectrum in the final amplifier, the Dazzler could be used to modulate the input spectrum, to prevent this. In correspondence to the change of the spectral shape, the output temporal shape is slightly asymmetric as well.

6.2 Design and setup

After choosing the principal amplification parameters (beam size, crystal length and doping concentration) and checking that the target output parameters are met in a 3D simulation, the implementation of the amplifier can be discussed.

In the following, the optical and mechanical design of the Booster amplifier setup will be described. The crystal mounting and cooling concept is presented as well as the layout of the multi-pass amplifier and pump beam transport and shaping.

6.2.1 Crystal mount and cooling concept

The thermal lens simulations showed, that the beam propagation through the crystal is sensitive on the temperature. With around 15 W of pumping power, the crystal

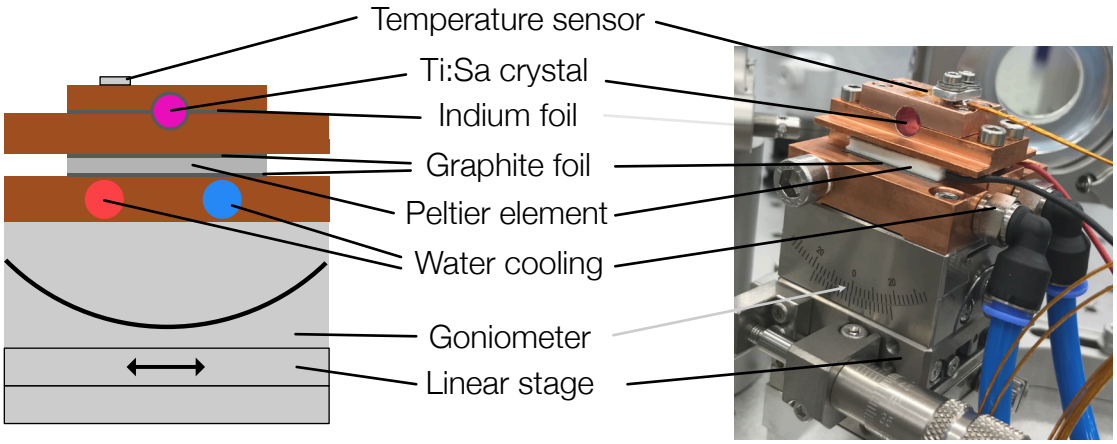

Figure 6.11 – XTAL mount including cooling concept: The crystal is surrounded by indium foil between two copper parts with round cut-outs. A peltier element below controls the temperature and is cooled by water, which runs through another copper part. The crystal rotation, longitudinal and transversal position can be tuned with mechanical stages. A temperature sensor is placed on top of the copper mount. The peltier element and temperature sensor are connected to a temperature control unit.

quickly heats, if it is not actively cooled. This makes a cooling concept for the crystal crucial for a stable long-term operation.
The cooling and mounting concept is sketched in figure 6.11. The crystal is surrounded by Indium foil and placed between two copper plates with round cut-outs. A temperature sensor (PT100) is mounted on the upper copper plate and a peltier element is placed below the lower copper plate. Both are connected to a temperature control unit (TEC-1123-HV, Meerstetter), that stabilizes the temperature by regulating the current and voltage of the Peltier element with a PID regulation. The lower side of the Peltier element is placed on a copper plate, that is water-cooled, to remove the heat from the setup. The water temperature is controlled by a dedicated chiller (ECO RE 420 G, Lauda)
When starting the pumping of the amplifier crystal, the temperature increases by 1.85 °C. After 3.2 minutes, the temperature is thermalized to ±0.1 °C (green dashed line) of the target temperature 18 °C (blue line). During operation of the amplifier, the measured temperature is stabilized to 18 °C ± 0.023 °C. It can be concluded, that the temperature stabilizations performs well.

For full pumping and amplification, the Peltier current and voltage are at 1.66 ± 0.025 A and 4.38 ± 0.069 V. The product of current and voltage gives the cooling power $P_{cooling}$=7.27 W. The expected cooling power is estimated in the following: The quantum defect in Ti:Sa is 34 % . This fraction of the absorbed power is directly converted to heat, that needs to be removed from the crystal. The amplification of the seed extracts around 0.5 W from the crystal. The residual stored pump energy

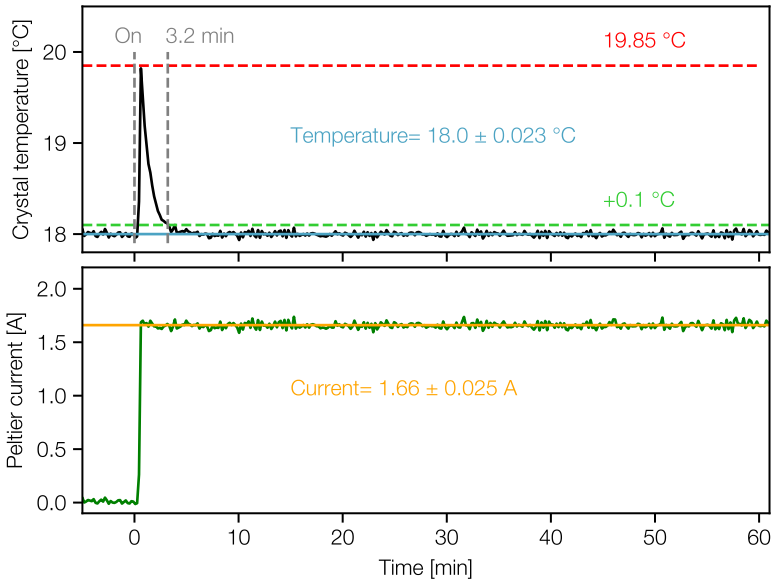

Figure 6.12 – Top: XTAL temperature during switch on (0 min) and for 1 hour of operation. Marked are the maximum temperature (red), the target temperature (18 °, blue) and a temperature increase of 0.1 ° (green). Bottom: The corresponding Peltier element current of the temperature stabilization. The pump power was 12 W.

in the crystal, can be emitted by spontaneous emission. While some of the light can exit the crystal at the end faces, most of the light is absorbed by the crystal mount. Assuming the spontaneously emitted radiation is isotropic, around 20 % of the spontaneous radiation exits the crystal and thus does not contribute to the heat load. For the pump power of 12 W, the estimation results in a final heat power of: P_{heat}=P_{QD}+$P_{spontaneousemission}$=3.79 +5.49 W =9.28 W. This is more than the measured cooling power. Additional cooling likely occurs by convection of the surrounding air. Amplified spontaneous emission would also explain a lower heat load on the crystal. As it would mainly occur along the longitudinal axis of the crystal, where the gain is the largest, it would not contribute to heating, but extract energy from the crystal.

In addition to cooling, the crystal mount allows for mechanical alignment. For the fine alignment of the crystal in x and y, it is placed on top of manual linear stages with micrometer screws. The crystal can be rotated around its longitudinal axis with a goniometer stage, to optimally align the crystal c-axis to the polarization axis of the seed light.

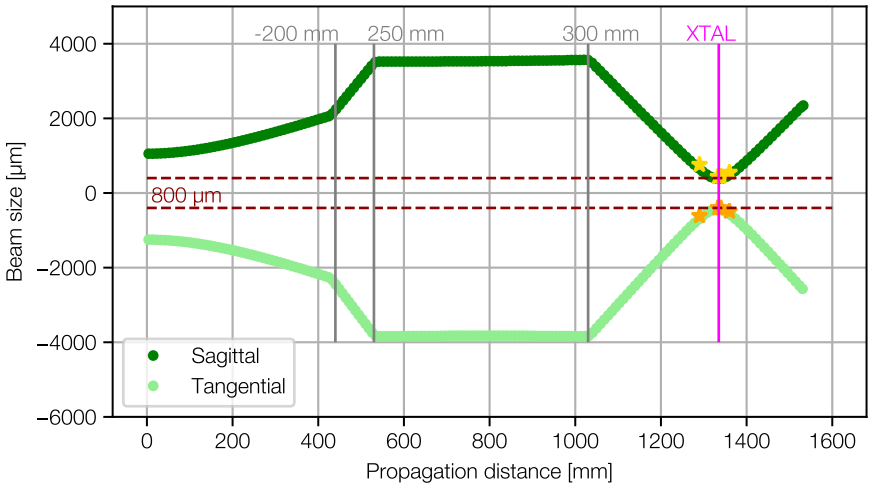

Figure 6.13 – Planned caustic of the pump beam. The final distances vary slightly to the presented ones. The final measured pump beam sizes are represented by the yellow and orange stars. The dashed lines mark the target beam size.

6.2.2 Pump routing and shaping

From the thermal lens and amplification simulations we deduced that the pump should have a diameter of 800 µm and should enter the beam from both sides of the crystal, to distribute the gain and the thermal load more homogeneously along the z-axis, than in a one-sided pumping approach.
With an M^2 of around 30, the Rayleigh-length of the pump laser is around 20 mm. This means that a collimation to an 800 µm diameter inside the crystal would require the collimation lenses to be placed very close to the crystal, which would hinder the incoupling of a seed beam.
Instead, the pump can be focused into the crystal. For the planning of the pump beam shaping the ray-tracing software vWaistWatcher was used. The planned caustic is shown in figure 6.13. The beam is enlargened and collimated by a Galilean telescope (f_1=-200 mm, f_1=250 mm,) to around 7.8 mm beam diameter. It is focused into the crystal by lenses with a focal length of 300 mm. During setup, the distances between the telescope lenses had to be slightly varied, until the beam size at the crystal center was 800 µm. The measured beam sizes around the crystal are represented by the yellow and orange stars in figure 6.13.

The routing of the pump beam layout is depicted in figure 6.14 (green).
The pump energy can be attenuated by a waveplate and two thin-film-polarizers (TFPs). After the expansion telescope, the beam is split in two with a 50:50 beam splitter, to pump the crystal from two sides collinearly. The beams can be aligned to the crystal axis by two 45 ° mirrors. Finally, both beams are focused into the crystal by two 300 mm lenses. The pump beams pass the dichroic mirrors, where they are

overlapped with the seed beam (red).
The crystal (XTAL) has an absorption coefficient of $1.85\,\mathrm{cm}^{-1}$, which corresponds to a doping of 0.1 % [114]. Its end faces were are coated with a low-reflectivity coating for 527 nm and 800 nm.

6.2.3 IR-beam routing and shaping

The IR-beam routing has to fulfill the following requirements: provide a 800 µm sized beam in the crystal for all three passes. In addition, the beam should reach the crystal at the smallest possible angles, to provide the best overlap. The first two passes have an angle of 2 ° The third pass is sent through the amplifier under zero degree, to achieve the best possible overlap and beam profile symmetry. This should increase the geometrical efficiency to >80 %.

The drawing of the amplifier in figure 6.14 shows all optics of the setup. Before and after the amplifier, telescopes adapt the beam size for the first pass of the Booster and for the next laser amplifier. Due to the small angles, the implementation of several passes need special care. The gain simulations showed three passes are sufficient for reaching the target output energy, thus three passes are planned. To ease the overlap between pump and seed and keep the setup compact two dichroic mirrors are placed under 45 ° on both sides of the crystal. The seed beam is reflected, which folds the multipass setup by 45 °. The focused pump beams pass through the dichroics.
To shorten the propagation lengths between the passes, the seed mirrors are d-shaped 1/2" mirrors as they can be placed closer to each other, than larger mirrors. They are mounted in custom designed mounts, that allow to move the mirrors horizontally within their mirror plane, to ease their horizontal placement. All used mirrors, except the dichroics, are high-reflectivity, low-GDD mirrors.

Not only the beam routing has to be planned precisely, but the beam size management as well. As discussed in section 6.1.4, some beam size adaption had to be integrated into the setup, to compensate the effect of the thermal lens. Comparing the COMSOL simulation with the thermal lens measurement, for an 800 µm beam, we expected the thermal lens to be around 250 mm (yellow dot in figure 6.5). From the 3D amplification simulations we learned that the beam size changes as well during amplification (see figure 6.9).

To investigate the beam size evolution through the amplifier, the beam size was measured at different positions after the crystal with the seed and the amplified beam at different pump energies. The measured beam sizes are shown in figure 6.15.

The horizontal and vertical seed beam diameter was measured at several positions around the crystal, which is located at 0 mm. In addition, the beam diameter of the

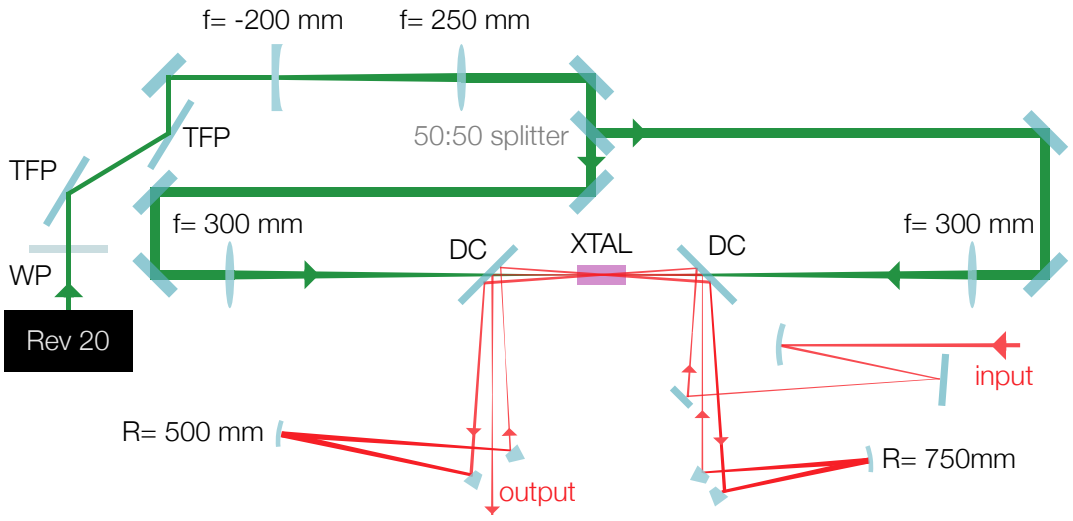

Figure 6.14 – The optical setup of the Booster amplifier. The pump beam can be attenuated by a $\lambda/2$ waveplate (WP) and two thin-film polarizers (TFPs). It is enlargened and split into two beams. Both beams are focused into the crystal (XTAL) through dichroic mirrors (DC). The IR beam is guided through the crystal three times. The maximum angle is 2°. Curved mirrors between the passes adapt the beam size and compensate the thermal lens.

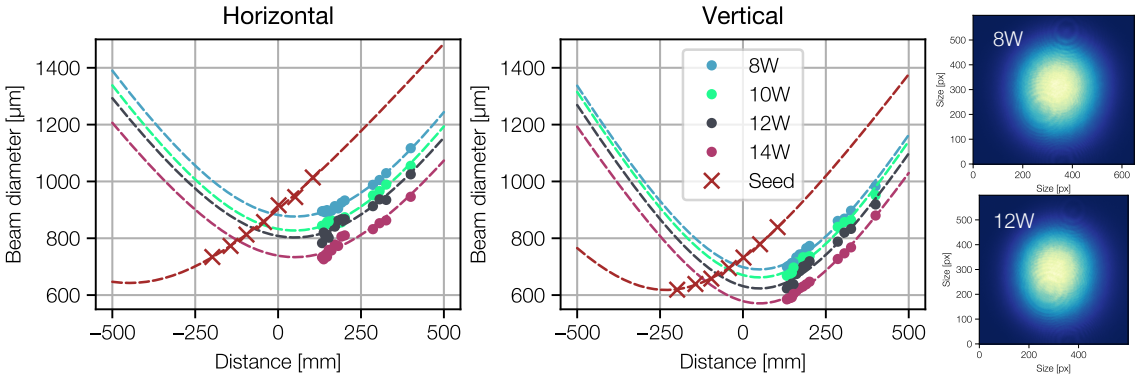

Figure 6.15 – Shown is a beam size diameter measurement of the seed beam through the first amplifier pass and the amplified beam size after the first amplifier pass. The amplified beam size was measured for several pump powers. Gaussian beam caustics are fitted to the measured beam size.

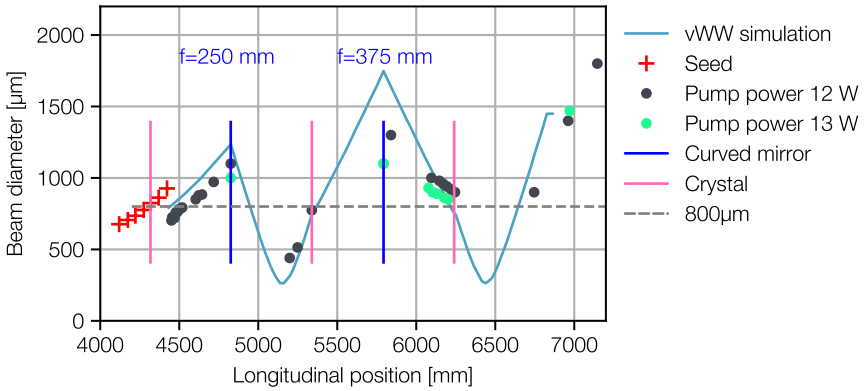

Figure 6.16 – Caustic of the 800 nm beam throughout the three passes of the Booster amplifier. The crystal positions are marked by pink vertical lines, the focusing mirror positions by blue. The beam diameter is close to 800 µm (grey, dashed line) at the crystal positions. The dots mark measured beam sizes at different pump powers at different positions of the amplifiers.

amplified beam was measured at different positions after the crystal for four pump powers. The amplified beam diameter could not be measured closer to the crystal due to space constraints. Afterwards, a Gaussian beam propagation fit was performed. Two beam profiles at the farthest position from the crystal are shown, one with 8 mJ pump energy, one with 12 mJ. Both beam profiles look smooth and symmetric.

The measured beam sizes and the fitted beam caustics confirm, that the beam size is reduced during amplification as could be observed in the simulations (see figure 6.9). The available gain in the middle of the beam profile is larger, than at the sides, which effectively reduces the beam size.
The divergence of the amplified beams, however, does not differ as much as it might be expected. From the thermal lens measurement (see: figure 6.7), one could expect a doubling in the thermal lens strength from 8 W of pump power, compared to 14 W of pump power, which would lead to an equivalent change in divergence. It seems, that the reduction of the beam size has an aperture-like effect on the beam, leading to a beam waist at the crystal output.

Still, the output beam is divergent and needs to be reshaped to reach the 800 µm beam diameter for the second pass. In the ABCD matrix simulation code vWaistWatcher the beam sizes, that were measured after the first pass, could be matched best in a propagation simulation, which assumed a thermal lens of 550 mm. This led to the beam caustic that is shown in figure 6.16. The simulated beam caustic is shown in blue. The optics in the amplifier are represented by colored vertical lines. The pink line represents the crystal and the blue, the focusing mirrors.

The input telescope consisted of a mirror telescope with focal lengths of f_1=1250 and f_2=-250 mm. After the first pass, the beam is divergent and refocused with a

f_3=250 mm mirror. The beam is focused before the XTAL and passes it again divergent. After the second pass, a f_4=375 mm mirror is placed. This mirrors the beam caustic and the target beam size is matched at the crystal position. After the last pass the beam is focused again and exits divergent.

In addition to the simulated caustic, measured beam sizes are added, symbolized by dots. The measured beam sizes deviate from the caustic, but the beam size at the crystal reaches the target 800 µm diameter. Throughout the amplification cavity, the beam that is amplified with a higher pump energy seems to stay smaller than the one with the lower pump energy. The beam size after the third pass, however, enlarges with the pump energy as will be seen later.

6.3 Amplifier performance

To confirm the Booster reaches its target parameters and to explore the available parameter space, the Booster performance was characterized in several measurements. As the front-end of KALDERA was still under construction while the Booster amplifier was built, some of the characterization was performed using a commercially available Ti:Sa laser (Astrella, Coherent). Specifically, a fraction of the stretched output of this laser was used. The input seed energy could be scanned between 5 and 30 µJ. The pulse duration was around 180 ps.
The beam profile at the XTAL and the spectrum of the Astrella are displayed in figure 6.17 as seed. The beam profile is slightly elliptic, but smooth and symmetric. The averaged d4σ-diameter is 779 µm. The modulation of the spectrum originates in the Astrella. [Note: The final input spectrum of OPCPA front-end (MASUBI) does not show these modulations. The integration of the final MASUBI into the stretcher and Booster amplifier will be described in 6.4.] It will be mentioned which characterizations were performed with the final front-end. The seed beam of 15 µJ energy was amplified with a pump energy of 12 mJ. The beam profiles of the amplified beam after all three passes are displayed as well in figure 6.17. The beam after the first pass is slightly elongated in vertical direction. After the second and the third pass the beam is round. [Note:The diffraction pattern in the beam after the second pass originated in the camera.]
The amplified spectrum shows the same spikes as the seed spectrum. It is slightly red-shifted as it was predicted by the simulation. Due to the shape of the input spectrum, the gain in the 'red' part of the spectrum leads to a broadening of the spectrum.

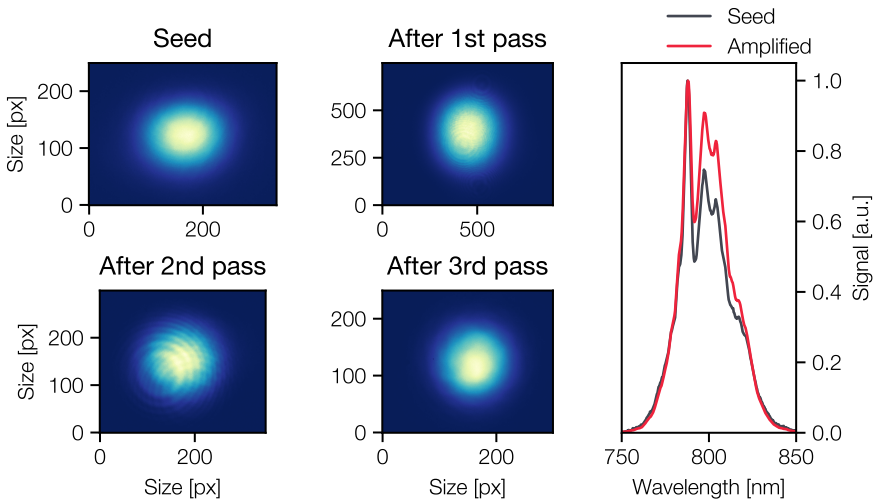

Figure 6.17 – Light: Beam profiles of the seed and the amplified beam after pass 1-3. Right: Input and output spectrum. The input seed energy was 15 µJ, the pump energy was 12 mJ.

6.3.1 Energy and gain

To explore the energy capacities of the Booster and the corresponding parameter space, scans of the seed energy (Astrella) and pump energy were performed. The seed energy was scanned in the range from 5 µJ to 30 µJ in steps of 5 µJ. The pump energy was scanned in the range from 10 mJ to 14 mJ in steps of 1 mJ. For every setting the output energy, beam profile and spectrum were measured. The final amplifier energies during the scan are shown in figure 6.18.

The target output energy of 500 µJ is reached with all seed energies >5 µJ with pump energies up to 13 mJ. Lower seed energies can be recovered by an increase in pump energy. For all pump energies a slight saturation of the output energy can be observed with increasing seed energies. The set point that was chosen for the following characterizations (M_2 measurement and long-term energy) is a seed energy of 15 µJ and a pump energy of 11 mJ.
From the scan results, the gain can be calculated for every set point, too. The results are given in figure 6.18. The maximum gain, that was measured for pumping with 13 mJ, was over 80.

The spectrum and beam size during the scan are shown in figure 6.19. Both spectral features mean wavelength and width hardly change with the seed and pump energy. The mean wavelengths seem to increase slightly with higher pump energies, which would be a sign for a slight red-shift, as it can be expected in Ti:Sa CPA laser systems.

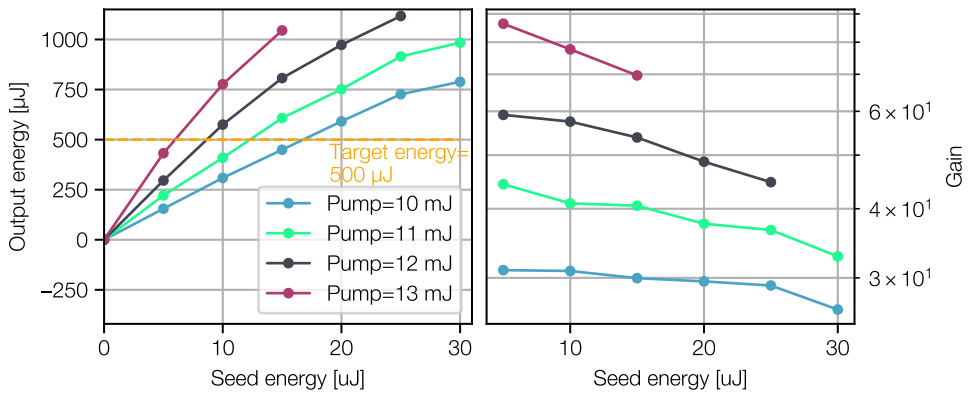

Figure 6.18 – Left: Resulting output energy of the Booster for different pump powers, depending on the seed energy. The output energy starts to saturate for high seed energies. The beginning of the saturation is shifted to lower seed energies for higher pump powers. Right: Resulting gain of the amplifier, maximum is 80.

The increase in mean wavelength and spectral width for 20 and 25 µJ can most likely be explained by daily changes in the Astrella spectrum.

The output beam size increases slightly in both axes with the pump energy. The increase in beam size is around 4 %. An increase of the beam size in dependence of the seed energy cannot be observed.

6.3.2 Beam and pulse properties

In the following, the spatial and temporal characterizations that were performed on the Booster output will be presented. These measurements were performed using the Astrella as input to the Booster. The measurements were performed after three amplification passes.

Like for both stretchers, the M^2 of the output beam was measured with a commercial device called BeamSquared from Ophir. It automatically performs a scan along the caustic, takes pictures of the beam and calculates the beam sizes at all scan positions, from which the M^2 value can be determined, using the Gaussian beam propagation function as fit function. The M^2 values are 1.13±0.004 and 1.15 ±0.005 in horizontal and vertical direction, respectively. The small increase in the beam size measurement at around 680 mm could not quite be explained, as the beam profile at that position looks smooth and not ununsual. The beam is still very close to a Gaussian beam and will provide a good seed beam profile and caustic for the succeeding amplifier.

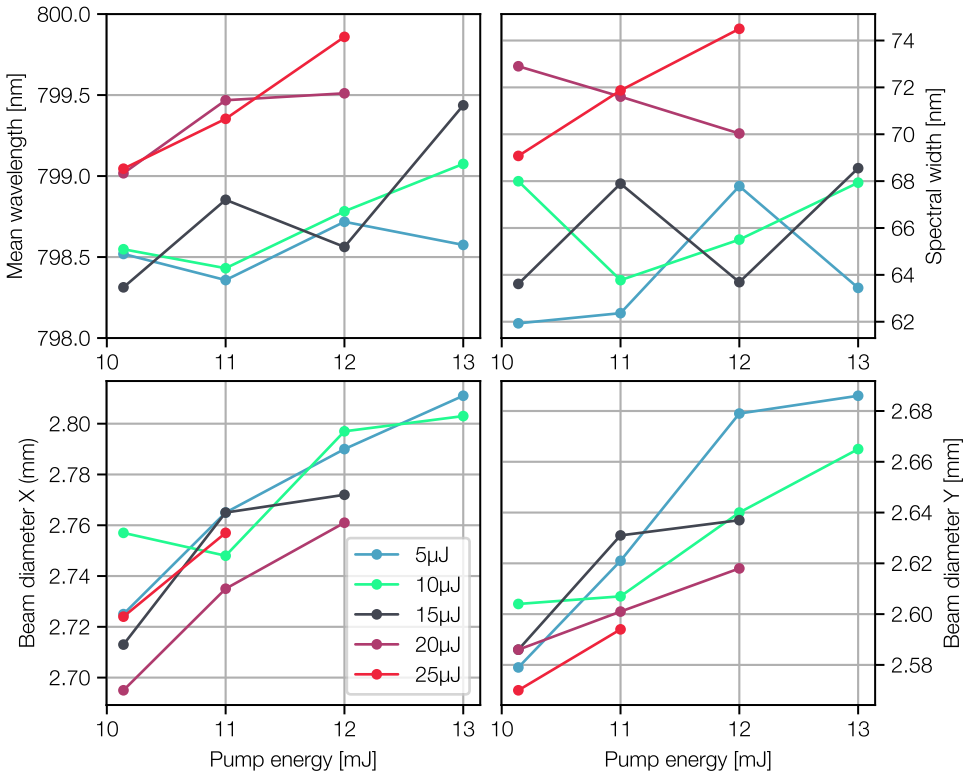

Figure 6.19 – Top: Mean wavelength (left) and spectral width (right) during the seed and pump energy scan. Bottom: Beam diameter in horizontal (left) and vertical direction (right).

6.3.3 Longterm performance

A stable long-term performance is one of the design goals of the KALDERA laser system. To achieve this goal, a stable performance of all subsystems is essential. The output energy of the Booster was measured over 15 h with an Ophir PE50 energy head. The energies were recorded with kHz repetition rate in the Starlab software of Ophir. From the raw data a rolling mean and standard deviation were calculated with a rolling window size of 1000 shots. A linear fit was made from the rolling mean, the gradient of this fit is 0.03 µJ/h, which corresponds to 0.004 %. This drift is negligible for laser operation.

The amplified energy is 580 ±23 µJ. The error originates in the calibration uncertainty of the energy head. The rolling standard deviation (bottom plot) is in the range of around 2.5 % in this measurement. The seed energy stability was 1 %. The used energy head adds noise of around to 1 % to the energy measurement. Taking both influences into account is not sufficient to explain the measured energy jitter. Energy measurements with lower noise were performed with the final front-end as seed and

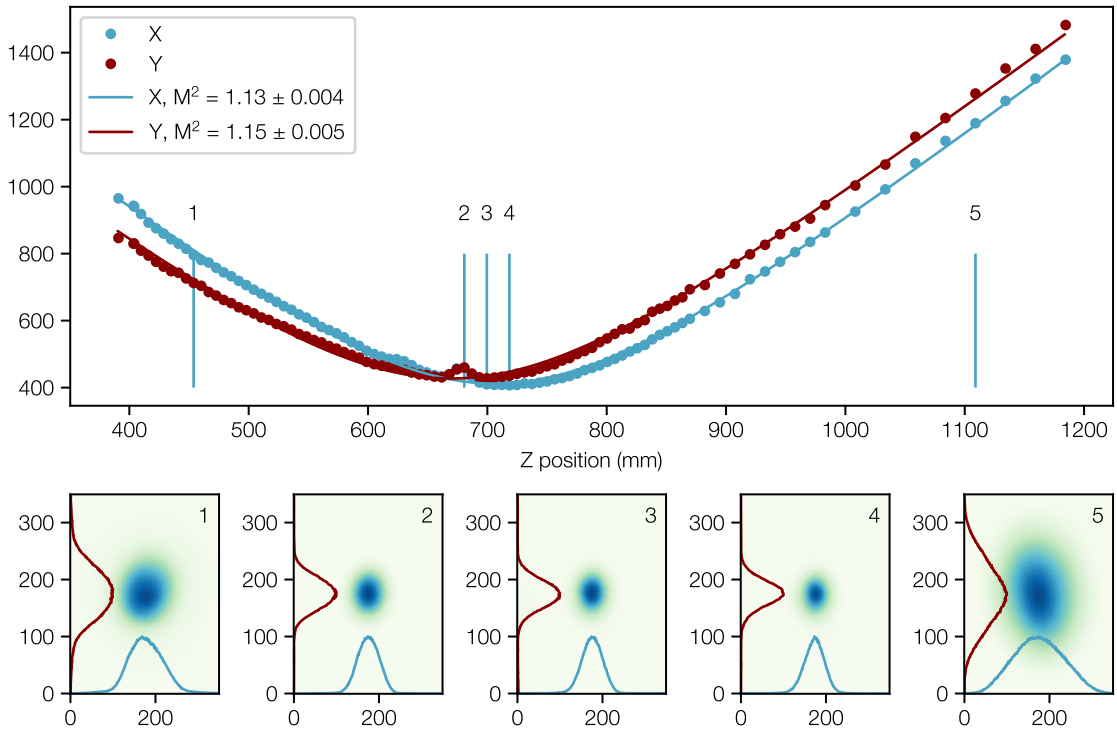

Figure 6.20 – M^2 measurement of the Booster output beam. The beam size in x (blue) and y (dark red) is measured. For five beam positions the beam profile including line-outs are shown in the bottom.

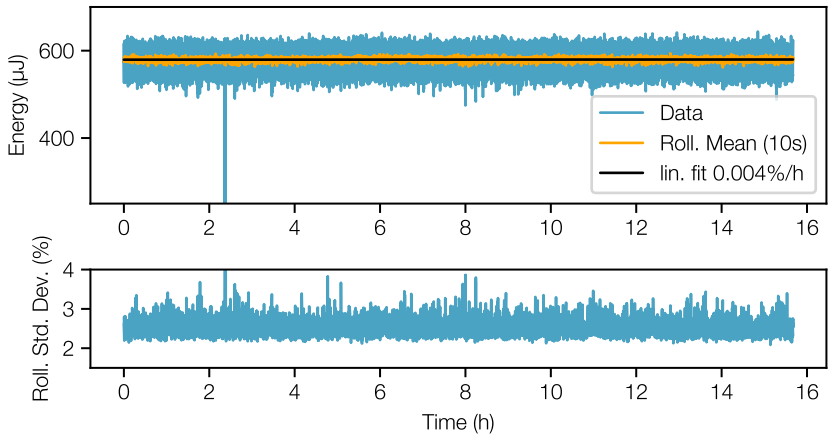

Figure 6.21 – Long-term measurement of the Booster output energy, seeded with Astrella. Plotted are the kHz raw data as well as the rolling mean (orange) and standard deviation (bottom) with a window size of 10000.

are presented in section 6.4.3, to discuss the sources of the energy jitter. However, the long-term stability suggests, that the amplifier itself causes no drifts to the system.

The previously presented results show, that the current setup is suitable to be used in the KALDERA amplification chain. In the following, the integration of the Booster into the full system (from MASUBI to MERAPI) will be described. Afterwards, the output parameters will be checked. Finally, sources of energy instability will be discussed as well as possible improvements.

6.4 Integration into the KALDERA amplifier chain

The Booster amplifier is part of the PICO section of KALDERA. It is situated behind the stretcher and the acusto-optic phase modulation filter (AOPDF, Dazzler, FASTLITE) and before the first cryogenic power amplifier (MERAPI). In the following, the interfaces between the Booster and the surrounding systems will be described: At first, the beam size adaptions and imaging systems will be explained. In the second part, the position and pointing stabilizations are presented and their effect on the system is evaluated. The sources of the jitter of the PICO output energy will be discussed. In the last part, the final performance of PICO when it is seeded with the OPCPA (MASUBI) is presented and the MERAPI performance with PICO seeding is addressed.

6.4.1 Beam size adaption and imaging throughout the front-end

Adaption of the beam size throughout the system is required to avoid reaching damage thresholds of optics and fit the beam to varying clear apertures. Figure 6.22 gives an overview over the beam sizes in and the telescopes between the subsystems. All beam sizes are given as $d4\sigma$ diameter. The beam profiles are all close to Gaussian.

The MASUBI output beam diameter is 1.7 mm. As the transmission gratings in the stretcher can be a source of B-integral, the beam diameter should be as large as possible. However, the clear aperture of the smallest stretcher optic is 12.6 mm, which means the maximum beam diameter should be < 5.4 mm [115].
The telescope between MASUBI and stretcher is a Galilean mirror telescope. The mirror focal lengths are $f_1 = -500$ mm and $f_2 = 1000$ mm.
The stretcher includes an imaging telescope as it was described in the previous chapter. Due to the telescope, the stretcher output beam size is similar to the input beam size. After the stretcher, the propagation length to the Dazzler is >3 m, which means, that the natural divergence will enlargen the beam. To achieve the target beam size of 2 mm, that is required for optimal efficiency in the Dazzler, another telescope was installed.

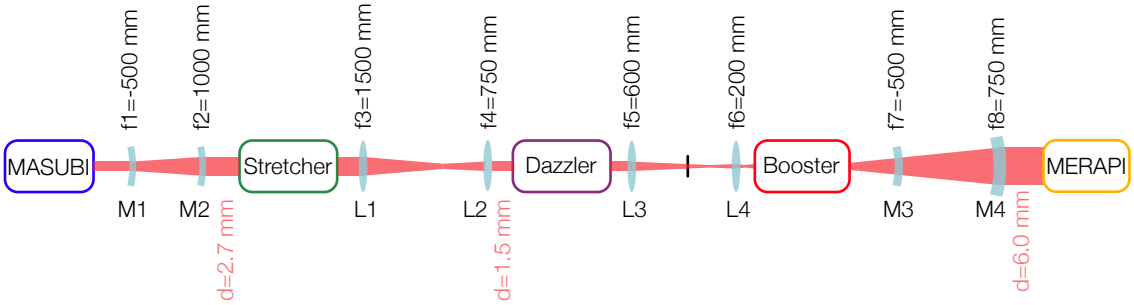

Figure 6.22 – Beam sizes and telescopes from OPCPA front-end (MASUBI) to the first cryo-amplifier (MERAPI). Curved mirror and lens focal lengths and collimated beam sizes are given.

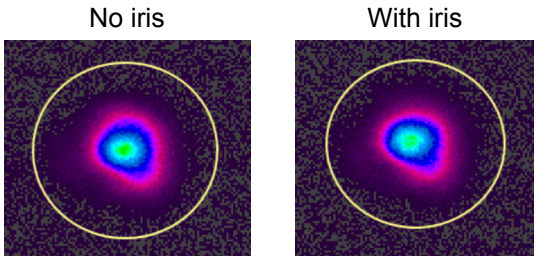

Figure 6.23 – Left: Spatial intensity distribution of the MASUBI seed at the XTAL position without spatial filtering. Right: The same beam with spatial filtering in the previous telescope

To increase passive stability of beam pointing and position, the telescope is an imaging telescope. As the pulses have a low intensity at that position, with µJ-level energy and the stretched pulse length of around 600 ps it can be realized with lenses without adding relevant B-integral. The focal lengths are $f_3 = 1500\,\text{mm}$ and $f_4 = 750\,\text{mm}$. For the same reasons, the telescope between the Dazzler and the Booster is an imaging lens telescope, too. An additional advantage is, that within the imaging telescope an aperture can be used for spatial filtering of the beam mode [116]. As the focus of a beam is the spatial Fourier-transformed of the original beam, any higher order modes, that disturb the beam-profile are radially separated from the main beam and can be blocked by an aperture of appropriate size, while the main beam is mainly transmitted. This aperture is placed, 180 mm after the first lens. The beam profile at the crystal position with and without the aperture are shown in figure 6.23. It can be noted that the beam profile is slightly smaller with the iris closed. However, the profile is still not optimal.

The telescope lenses and distances have to be chosen such, that the beam size inside the crystal is again $\leq 800\,\mu\text{m}$ diameter and causes a beam caustic through the three-passes of the amplifier as it has been described in 6.2.3. A telescope of f_1=600 mm and f_2=200 mm with a distance of fulfilled this requirement to a sufficient precision.

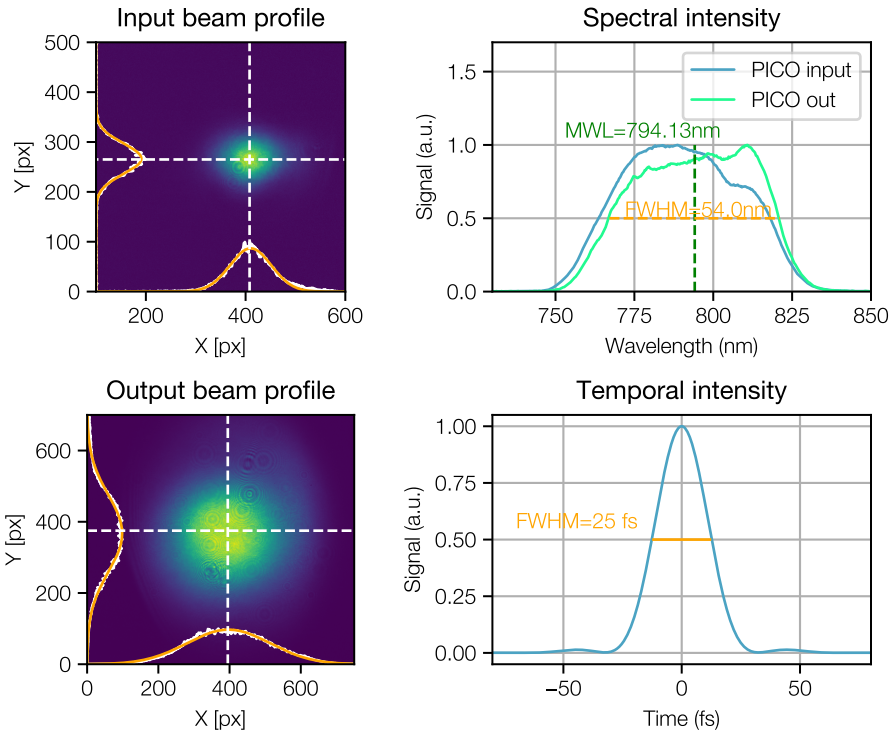

Figure 6.24 – Left: Input and output beam intensity distribution. Right: Top: Spectral intensity distribution before and after PICO, bottom: calculated temporal intensity, assuming a fully compressed pulse with the output spectrum

The final collimated beam profile after the Booster and the enlarging telescope is shown in figure 6.24. It is smooth and round. The lineouts of the beam profile (white) are fitted with Gaussian distributions of order 1 (orange). The target output energy of 500 µJ is achieved. The output spectrum in figure 6.24 supports sub-30 fs pulses.

After the Booster, the beam is enlarged and collimated to 6 mm diameter to provide a good seed for the MERAPI amplifier. Here, a Galilean mirror telescope is chosen, as the energy is at mJ-level and material transmission should be avoided. The telescope mirrors focal lengths are: f_7=-500 mm and f_8=750 mm.

6.4.2 Beam stabilization systems

The following analysis of pointing and energy stability was performed with the support of T. Hülsenbusch.

The propagation lengths between the individual setups in the KALDERA front-end are in the meter range. In such a long propagation, already small angle changes

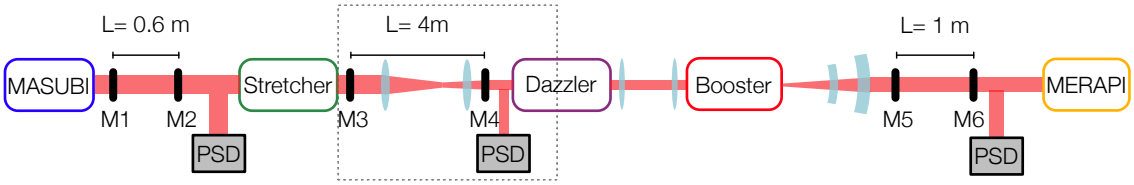

Figure 6.25 – Transport section between stretcher and Booster including TEM system, consisting of two actuated mirrors (M1-M6) each and a position-sensitive-diode (PSD). The telescope lenses and mirrors are identical with the ones from 6.22.

cause relatively large position changes at the next setup. This can cause problems, as e.g. the overlap with the 800 µm diameter pump beam is not optimal or the beam is partially blocked by smaller apertures. Apart from small pointing changes in one position of the system, long propagation lengths on air can add pointing jitter to the beam due to air fluctuations.
Possible measures to stabilize the pointing and position passively are imaging telescopes, mechanical rigidity of setups and housing or shielding from air flow. Active beam stabilizations can improve the stability further. The imaging telescopes, that bridge the propagation between the stretcher and the Dazzler and the Dazzler and the Booster were described in the previous section. The mechanical rigidity of all optics mounts was already part of the discussion in chapter 4. A housing was only installed for the stretcher and the MASUBI at the time, when the studies for this thesis were carried out.
To allow for active stabilization of the remaining pointing and position jitter, several beam stabilizations were installed. The placement of the ones, that will be discussed here is presented in figure 6.25. The beam stabilization is a commercial system from TEM, that consists of a combined module of two photodiode detectors for position and pointing measurement (PSD), two mirror mounts, that are driven with piezo-elements (POLARIS-K1S2P) and a control unit, to run the stabilization.

The position and angle measurement resolution of the PSD is <1 µm and <1 µrad [117]. From the distances between the piezo-mirrors and the piezo angular resolution (0.5 µrad [118]), the achievable positional resolution can be calculated. For all three systems it is <1 µm, which is below the resolution of the PSD. Making the PSD resolution the limit of the position stabilization.
The angular precision is limited by the resolution of the PSD to 1 µrad. To check, if this is sufficient for the laser system, the following consideration can be made: A 'free' propagation over 5 m after a beam stabilization would cause a beam offset of 5 µm. This is <1 % of the beam size at the most position sensitive point in the described system, which is the amplifier crystal. The resolution of the TEM systems should thus be sufficient, to stabilize the beam to the required precision.

The final performance of the beam stabilization is also influenced by other conditions. Especially, the frequencies of the disturbances, that cause the jitter, play a crucial role. As in every regulation system, disturbances can only be compensated for, if they occur with frequencies, that are below the regulation frequency of the regulation system. The exact regulation bandwidth of the used beam stabilization could not be determined yet, but it is >23 Hz.
To see the influence of the TEM in front of PICO (marked by grey box in figure 6.25) on the pointing stability and PICO energy, a camera, that operates at 1 kHz was placed after the Booster amplifier in the focus of a lens with f=300 mm. The beam position in x and y and the counts of the camera were recorded for 1 minute with and without the beam stabilization. The total counts of the camera could be used as relative measure of the PICO output energy.
To find possible sources of energy and pointing jitter, the integrated standard deviation was calculated. This means a low-pass filter was applied to the frequency domain of the data and the standard deviation of the filtered signal was calculated. Scanning the cut-off frequency of the low-pass filter from high to low energies results in the integrated standard deviations as they are shown in figure 6.26. The top plot shows the integrated standard deviation of the camera counts, which is a measure for the output energy. Apart from the large contribution at 50 Hz, that will be discussed later, a small contribution at 23 Hz is visible in the unstabilized signal. In the stabilized signal this contribution is hardly visible. Looking at the pointing standard deviation in the horizontal (middle plot) and vertical (bottom plot) direction, it is noticable, that the jitter at 23 Hz is visible in the vertical direction as well. The beam stabilization again strongly reduces this contribution. This suggests, that the energy jitter originates in a pointing jitter in the vertical direction. Its origin has to be in the section before the PICO beam stabilization.
The suppression of the 23 Hz jitter shows, that the regulation bandwidth of the TEM is > 23 Hz.

It can also be noted, that a significant part of the pointing jitter results from frequencies <10 Hz. In this frequency range the difference between the stabilized and the unstabilized signal is small in both directions. This suggests, that the source of the lower frequency jitter lies after the TEM. It might be caused by the long propagation range after the TEM to the Booster and through the Booster amplifier.
The total integrated pointing standard deviation in the observed frequency range is 0.08 px and 0.12 px in horizontal and vertical direction. These correspond to 0.67 and 1.2 % of the beam size. The previous analysis already showed a connection between the beam pointing and the energy jitter. In the following, the energy jitter will be analyzed further.

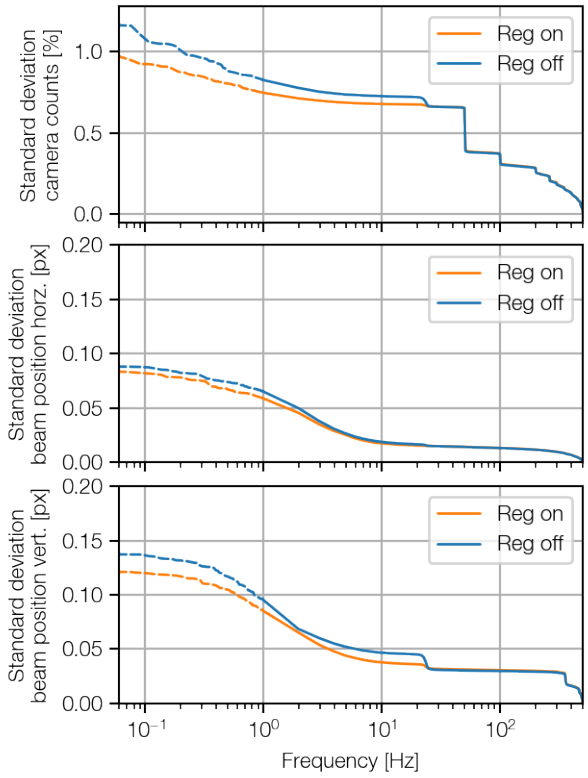

Figure 6.26 – Integrated standard deviation in the frequency domain of the counts on a kHz camera after the Booster (top), the beam position in the horizontal (middle) and vertical (bottom) direction. The integrated jitter is shown for a measurement with beam stabilization on (orange) and off (blue). Courtesy to T. Hülsenbusch

6.4.3 Analysis of output energy jitter

To find sources for the energy jitter, the energy was measured with a high resolution photodiode head and the frequency-resolved amplitude spectrum was calculated again. The integrated jitter was calculated to compare the contributions of the different frequencies to the overall jitter. The results are presented in figure 6.27. Most notable in the PICO output energy are the broad signal at around 23 Hz, which likely originates in a pointing jitter as it was analyzed before and the peak at 50 Hz and its higher harmonics 100, 200 and 300 Hz. The signal at 23 Hz is not visible at the MASUBI output, but at the PICO input energy. We learned earlier, that it is introduced before the PICO TEM beam stabilization, before the Booster. Its visibility in the input seed energy, means that a coupling between pointing and energy is introduced already before the amplifier, likely by an aperture. From the previous analysis it can be concluded, that this contribution can however be strongly reduced by the TEM

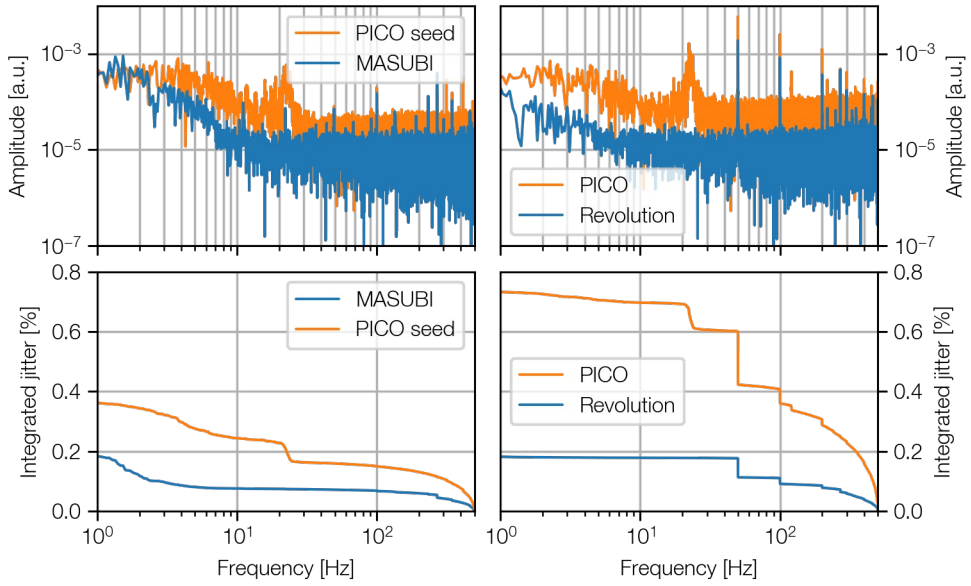

Figure 6.27 – Frequency analysis of MASUBI and direct amplifier input energy measurement (left) and pump and amplifier output energy measurement (right). Courtesy to T. Hülsenbusch

system.
The signal at 50 Hz is not visible in the input seed energy, but it can clearly be seen in the pump energy (right plot, blue) and it is the main contribution to the pump energy jitter. It is also the main contribution to the PICO output energy jitter. A probable source for this fluctuation in the pump power at 50 Hz is the frequency of the mains voltage in Germany, which is 50 Hz. The Revolution laser is directly pumped by laser diodes, thus fluctuations in the voltage can directly affect the output energy.

To judge the improvement, that could be reached, if the 50 Hz modulation could be cancelled, the following precedure was performed. The frequency dependent amplitude spectrum of the PICO output energy was filtered for the 50 Hz and its higher harmonics. The result is shown in figure 6.28 (green). The target 0.5 % standard deviation (green, dashed) is not quite reached, but the standard deviation is largely reduced.

From this measurement the output energy jitter of the Booster could be deduced to be 0.88 % (red, dashed line), as the total standard deviation of the kHz camera counts in 6.28. The gap between the integrated jitter signal (blue) and this values shows the presence of even slower (<0.1 Hz) modulations in the output energy.

The initial goal was to reach an energy stability of 0.5 %. However, the jitter in the pump at 50 Hz and unstabilized pointing drifts have prevented this so far. To judge the influence of this output energy jitter on the performance of the succeeding

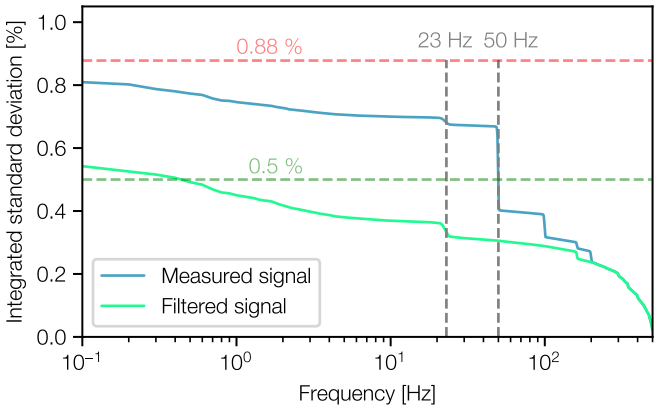

Figure 6.28 – Frequency-dependent integrated standard deviation of the output energy, measured as counts on the kHz camera (blue). The total measured standard deviation is 0.88 % (red, dashed line). The target standard deviation of 0.5 % is marked with a dashed green line. To estimate the improvement without the 50 Hz jitter from the pump, the signal was filtered for that. The resulting integrated standard deviation is shown in green.

amplifier MERAPI, a scan of the seed energy was performed and the output energy was measured. The result of the scan is presented in figure 6.29.

The measured energies are represented by the orange dots. The output energy clearly saturates with increasing input energy. A linear fit was added as interpolation between the two points of the highest energy and is centered at the input energy of the operation point of MERAPI.
In this energy range, a change of the input energy by 0.1 mJ, which corresponds to 20 % leads to a change of 1.06 mJ of the output energy, which corresponds to a relative change of only 2.6 %. This means the relative change in output energy is reduced by a factor of 7.7 in MERAPI due to saturation. The energy jitter in the PICO output energy will thus be strongly reduced in MERAPI and even further in the final amplifier COLIMA.

6.4.4 Outlook

As has been discussed in the last sections, the Booster amplifier delivers the target output energy of >500 µJ and even up to 1 mJ, enabling amplification saturation in the next amplifier. The width of the amplified spectrum is 54 nm (FWHM) and the output beam has a Gaussian shape with an ellipticity of >0.9. It reaches an energy stability of <1 % which is more than sufficient to reach <0.5 % output energy stability in the next amplifier.

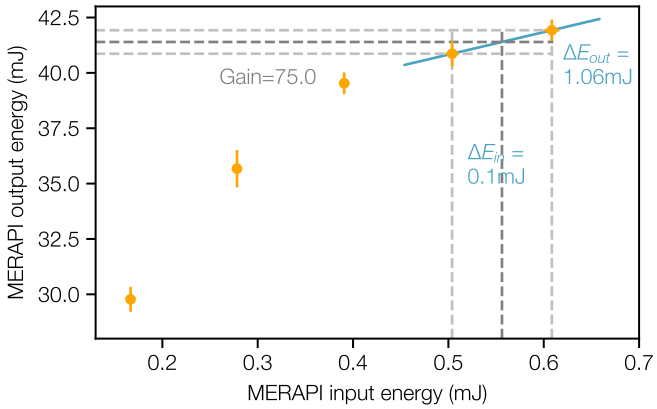

Figure 6.29 – Measured amplified MERAPI output energy in dependence of the PICO energy (orange dots). A linear fit is applied to the highest two energies. A 20 % change of the input seed is marked by vertical grey dashed lines, the corresponding change in output energy is marked by horizontal dashed lines and resembles 2.6 % of the energy.

For a more stable output energy the TEM stabilization system could be placed closer to the amplifier entrance, to reduce slower drifts, that are collected on the transport between TEM and PICO entrance.

To improve the amplifier in terms of efficiency, more passes through the amplifier crystal would be required. This would be hard to implement with the current design, as the angles and optics are already very small. A possible alternative setup is presented in [119]. Instead of going back and forth, as in the previously discussed design, the beam is going in a triangle, every pass having a slightly different angle through the amplifier. The compensation of the thermal lens is achieved by two curved mirrors, that form an imaging telescope, which keeps the beam size in the crystal constant throughout the passes.

After the successful demonstration of the concept of the Booster amplifier, a second iteration of the setup can be planned. To improve passive stability, an engineered version of the setup can be built. Among other improvements this would include a reduced beam height, more monolithic optomechanical components and a housing.

7 Conclusion and Outlook

Among other applications, TW-class fs-lasers are used to drive laser-plasma accelerators (LPAs) [24, 35]. At DESY, a strong push towards the stability and long-term operation of LPAs is made in the LUX LPA, that is driven by the ANGUS laser and with the KALDERA project, that aims for stable electron acceleration at >100 Hz repetition rates.

Long-term drifts in the ANGUS laser have provided the motivation to develop a new, stable front-end for ANGUS. This development included the design and setup of the stretcher, that was presented in chapter 4 of this thesis. The developed stretcher provides good mechanical stability and tunability. Beam position and pointing monitoring and active stabilization were implemented. The stretcher was mechanically tuned to match the dispersion of the already existing ANGUS compressor. With the new front-end, the pulses could be compressed to shorter pulse durations (31 fs), than before (>35 fs) and an improved pulse duration stability of <1 % was achieved. So far, the stretcher has supported around 100 successful beam times at the LUX laser-plasma accelerator.

To minimize the angular chirp in the stretcher output beam, an alignment method with a three-color laser was established. The method provided a precision to 0.1 µrad/nm, which is comparable to other methods. However, the three-color laser method provided the advantage, that simultaneous optimization of the vertical and horizontal chirp was possible. In addition, it could be set up easily at any position of the laser system. The angular chirp of the stretcher output could be reduced to <0.5 µrad/nm, which was estimated to be sufficient for further amplification. This alignment method was successfully applied for the alignment of three more stretcher and compressor setups.

The precision of the angular chirp measurement could be further improved by increasing the pointing and power stability of the 3-color laser. A more detailed analysis of the stretcher alignment state could be reached by adding more colors to the laser.
This alignment method is applicable to many other (angularly-) dispersive setups as long as laser diodes in the desired spectral range are available. The three-color laser could be utilized to provide an online diagnostic of the angular chirp during laser operation, which might enable the surveillance of otherwise hardly accessible laser parameters.

The experience from the build-up and alignment of the ANGUS stretcher was used to design and setup a stretcher for the KALDERA laser. Gold gratings in the final pulse compressor have so far limited the usable average power of TW fs-laser systems [36, 77]. Multi-layer dielectric (MLD) gratings are more durable against high average powers. But only recently, gratings that support a bandwidth for sub-30 fs compression have been developed. The development of a stretcher, that matches an out-of-plane MLD grating compressor is described in chapter 5. It enabled the first demonstration of compression of sub-30 fs pulses in a compressor with MLD gratings. In addition, the compressed pulse properties such as contrast and output polarization state were measured to be comparable to gold-grating compressed pulses. The total transmission efficiency of the MLD compressor was around 80 %, which is higher, than the typical gold grating compressor efficiency of 70 %, as mentioned in 5. This shows the viability and potential of MLD gratings in TW fs-laser systems, such as KALDERA. Their use allows to overcome the limitation in average power, that gold grating compressors started to pose for these systems. The developed transmission-grating stretcher provides a viable concept to match the dispersion of such a compressor.
After demonstrating the compression with µJ energies, the stretcher was integrated into the KALDERA laser system. Together with the compressor, it will allow for compression of 0.5 J pulses to sub-30 fs pulse lengths soon. A scaled version of the stretcher, which is already under development, will be built for the second project phase of KALDERA. It will provide up to 5 J 30 fs pulses.

The energy stability requirements of the KALDERA laser are based on the demands for stable electron acceleration. Sub-percent energy stability in high energy laser amplifiers is often reached by saturating the amplification process. This is enabled by high seed energies. To provide a sufficient seed energy to saturate the final amplifiers of the KALDERA laser was a core goal of the developed Booster amplifier, described in chapter 6. This goal was met with amplification to up to 1 mJ of output energy. The energy was provided with excellent long-term energy stability and sub-percent energy jitter. An analysis of the sources for the energy jitter showed, that a further improvement of the output energy stability could be reached, with a reduction of the pump energy jitter and by stabilizing the seed beam pointing closer to the Booster entrance. The development of an engineered version of the Booster could provide an increased passive stability.
Already with the current output parameters, the Booster enabled the amplification in the final cryogenic laser amplifier to <0.5 % energy stability at 700 mJ output energy [39]. The amplified Booster spectral width supports compression to 25 fs FWHM pulses, meeting the demanding target parameters of the KALDERA laser.
Compared to the Booster amplifier of ANGUS, the presented amplifier provides more energy with a lower energy jitter. Amplifiers at this energy range are often required in Ti:Sa CPA laser systems, to bridge the gap between the low energy seeder and the higher energy amplifiers. The concept of the Booster of using beam size adaption

after every pass to compensate the thermal lens, proved successful and provided a smooth and round beam profile, that was robust against changes in pump energy. This concept could be utilized at other Ti:Sa laser systems.

The presented KALDERA stretcher and the Booster are both integral parts of the KALDERA laser system, which will soon accelerate first electrons at 100 Hz repetition rate. They strongly contribute to the development of highly stable, higher repetition rate TW-class fs-lasers for highly-demanding applications such as laser-plasma acceleration.

Bibliography

[1] T. H. Maiman. Stimulated optical radiation in ruby. *Nature*, 187(4736):493–494, aug 1960. doi:10.1038/187493a0.

[2] A. Javan, W. R. Bennett, and D. R. Herriott. Population inversion and continuous optical maser oscillation in a gas discharge containing a He-Ne mixture. *Phys. Rev. Lett.*, 6:106–110, Feb 1961. doi:10.1103/PhysRevLett.6.106.

[3] D. Zigmantas, T. Polívka, P. Persson, and V. Sundström. Ultrafast laser spectroscopy uncovers mechanisms of light energy conversion in photosynthesis and sustainable energy materials. *Chemical Physics Reviews*, 3(4):041303, nov 2022. doi:10.1063/5.0092864.

[4] B. P. Abbott, R. Abbott, T. D. Abbott, M. R. Abernathy, F. Acernese, K. Ackley, C. Adams, T. Adams, P. Addesso, R. X. Adhikari, V. B. Adya, C. Affeldt, M. Agathos, K. Agatsuma, N. Aggarwal, O. D. Aguiar, L. Aiello, A. Ain, P. Ajith, B. Allen, and other. Observation of Gravitational Waves from a Binary Black Hole Merger. *Phys. Rev. Lett.*, 116:061102, Feb 2016. doi:10.1103/PhysRevLett.116.061102.

[5] O. Guven, M. Gul, E. Ayan, J. A. Johnson, B. Cakilkaya, G. Usta, F. B. Ertem, N. Tokay, B. Yuksel, O. Gocenler, C. Buyukdag, S. Botha, G. Ketawala, Z. Su, B. Hayes, F. Poitevin, A. Batyuk, C. H. Yoon, C. Kupitz, S. Durdagi, R. G. Sierra, and H. DeMirci. Case Study of High-Throughput Drug Screening and Remote Data Collection for SARS-CoV-2 Main Protease by Using Serial Femtosecond X-ray Crystallography. *Crystals*, 11(12), 2021. doi:10.3390/cryst11121579.

[6] J. C. Culp. US patent: Laser cutting. Patent Number US 9,403,238 B2, August 2,2016.

[7] S. G. Bown. LASER ENDOSCOPY. *British Medical Bulletin*, 42(3):307–313, jan 1986. doi:10.1093/oxfordjournals.bmb.a072143.

[8] R. R. Gattass and E. Mazur. Femtosecond laser micromachining in transparent materials. *Nature Photonics*, 2(4):219–225, 2008. doi:10.1038/nphoton.2008.47.

[9] W. Gambling. The rise and rise of optical fibers. *IEEE Journal of Selected Topics in Quantum Electronics*, 6(6):1084–1093, 2000. doi:10.1109/2944.902157.

[10] A. Lees, R. Betti, J. P. Knauer, V. Gopalaswamy, D. Patel, K. M. Woo, K. S. Anderson, E. M. Campbell, D. Cao, J. Carroll-Nellenback, R. Epstein, C. J. Forrest, V. N. Goncharov, D. R. Harding, S. X. Hu, I. V. Igumenshchev, R. T. Janezic, O. M. Mannion, P. B. Radha, S. P. Regan, A. Shvydky, R. C. Shah, W. T. Shmayda, C. Stoeckl, W. Theobald, and C. A. Thomas. Understanding the fusion yield dependencies in OMEGA DT-layered implosion experiments using a physics-based statistical mapping model. *Physics of Plasmas*, 30(1): 012709, Jan. 2023. doi:10.1063/5.0106515.

[11] E. Esarey, C. B. Schroeder, and W. P. Leemans. Physics of laser-driven plasma-based electron accelerators. *Rev. Mod. Phys.*, 81:1229–1285, Aug 2009. doi:10.1103/RevModPhys.81.1229.

[12] I. Pomerantz, E. McCary, A. R. Meadows, A. Arefiev, A. C. Bernstein, C. Chester, J. Cortez, M. E. Donovan, G. Dyer, E. W. Gaul, D. Hamilton, D. Kuk, A. C. Lestrade, C. Wang, T. Ditmire, and B. M. Hegelich. Ultrashort Pulsed Neutron Source. *Phys. Rev. Lett.*, 113:184801, Oct 2014. doi:10.1103/PhysRevLett.113.184801.

[13] J. Badziak. Laser-driven ion acceleration: methods, challenges and prospects. *Journal of Physics: Conference Series*, 959(1):012001, jan 2018. doi:10.1088/1742-6596/959/1/012001.

[14] I. Cohen, T. Meir, K. Tangtartharakul, L. Perelmutter, M. Elkind, Y. Gershuni, A. Levanon, A. V. Arefiev, and I. Pomerantz. Undepleted direct laser acceleration. *Science Advances*, 10(2):eadk1947, 2024. doi:10.1126/sciadv.adk1947.

[15] D. Strickland and G. Mourou. Compression of amplified chirped optical pulses. *Optics Communications*, 55(6):447–449, 1985. doi:https://doi.org/10.1016/0030-4018(85)90151-8.

[16] T. Tajima and J. M. Dawson. Laser Electron Accelerator. *Phys. Rev. Lett.*, 43: 267, 1979. doi:https://doi.org/10.1103/PhysRevLett.43.267.

[17] J. Faure, Y. Glinec, A. Pukhov, S. Kiselev, S. Gordienko, E. Lefebvre, J.-P. Rousseau, F. Burgy, and V. Malka. A laser–plasma accelerator producing monoenergetic electron beams. *Nature*, 431(7008):541–544, Sept. 2004. doi:10.1038/nature02963.

[18] S. P. D. Mangles, C. D. Murphy, Z. Najmudin, A. G. R. Thomas, J. L. Collier, A. E. Dangor, E. J. Divall, P. S. Foster, J. G. Gallacher, C. J. Hooker, D. A. Jaroszynski, A. J. Langley, W. B. Mori, P. A. Norreys, F. S. Tsung, R. Viskup, B. R. Walton, and K. Krushelnick. Monoenergetic beams of relativistic electrons from intense laser–plasma interactions. *Nature*, 431(7008):535–538, Sept. 2004. doi:10.1038/nature02939.

[19] W. P. Leemans, B. Nagler, A. J. Gonsalves, C. Tóth, K. Nakamura, C. G. R. Geddes, E. Esarey, C. B. Schroeder, and S. M. Hooker. GeV electron beams from a centimetre-scale accelerator. *Nature Physics*, 2(10):696–699, oct 2006. doi:10.1038/nphys418.

[20] M. Fuchs, R. Weingartner, A. Popp, Z. Major, S. Becker, J. Osterhoff, I. Cortrie, B. Zeitler, R. Hörlein, G. D. Tsakiris, U. Schramm, T. P. Rowlands-Rees, S. M. Hooker, D. Habs, F. Krausz, S. Karsch, and F. Grüner. Laser-driven soft-X-ray undulator source. *Nature Physics*, 5(11):826–829, Nov. 2009. doi:10.1038/nphys1404.

[21] S. Fourmaux, S. Corde, K. T. Phuoc, P. Lassonde, G. Lebrun, S. Payeur, F. Martin, S. Sebban, V. Malka, A. Rousse, and J. C. Kieffer. Single shot phase contrast imaging using laser-produced Betatron x-ray beams. *Opt. Lett.*, 36(13): 2426–2428, Jul 2011. doi:10.1364/OL.36.002426.

[22] A. R. Maier, A. Meseck, S. Reiche, C. B. Schroeder, T. Seggebrock, and F. Grüner. Demonstration Scheme for a Laser-Plasma-Driven Free-Electron Laser. *Phys. Rev. X*, 2:031019, Sep 2012. doi:10.1103/PhysRevX.2.031019.

[23] W. Wang, K. Feng, L. Ke, C. Yu, Y. Xu, R. Qi, Y. Chen, Z. Qin, Z. Zhang, M. Fang, J. Liu, K. Jiang, H. Wang, C. Wang, X. Yang, F. Wu, Y. Leng, J. Liu, R. Li, and Z. Xu. Free-electron lasing at 27 nanometres based on a laser wakefield accelerator. *Nature*, 595(7868):516–520, jul 2021. doi:10.1038/s41586-021-03678-x.

[24] A. J. Gonsalves, K. Nakamura, J. Daniels, C. Benedetti, C. Pieronek, T. C. H. de Raadt, S. Steinke, J. H. Bin, S. S. Bulanov, J. van Tilborg, C. G. R. Geddes, C. B. Schroeder, C. Tóth, E. Esarey, K. Swanson, L. Fan-Chiang, G. Bagdasarov, N. Bobrova, V. Gasilov, G. Korn, P. Sasorov, and W. P. Leemans. Petawatt Laser Guiding and Electron Beam Acceleration to 8 GeV in a Laser-Heated Capillary Discharge Waveguide. *Phys. Rev. Lett.*, 122:084801, Feb 2019. doi:10.1103/PhysRevLett.122.084801.

[25] J. P. Couperus, R. Pausch, A. Köhler, O. Zarini, J. M. Krämer, M. Garten, A. Huebl, R. Gebhardt, U. Helbig, S. Bock, K. Zeil, A. Debus, M. Bussmann, U. Schramm, and A. Irman. Demonstration of a beam loaded nanocoulomb-class laser wakefield accelerator. *Nature Communications*, 8(1):487, Sept. 2017. doi:10.1038/s41467-017-00592-7.

[26] R. Weingartner, S. Raith, A. Popp, S. Chou, J. Wenz, K. Khrennikov, M. Heigoldt, A. R. Maier, N. Kajumba, M. Fuchs, B. Zeitler, F. Krausz, S. Karsch, and F. Grüner. Ultralow emittance electron beams from a laser-wakefield accelerator. *Phys. Rev. ST Accel. Beams*, 15:111302, Nov 2012. doi:10.1103/PhysRevSTAB.15.111302.

[27] G. R. Plateau, C. G. R. Geddes, D. B. Thorn, M. Chen, C. Benedetti, E. Esarey, A. J. Gonsalves, N. H. Matlis, K. Nakamura, C. B. Schroeder, S. Shiraishi, T. Sokollik, J. van Tilborg, C. Toth, S. Trotsenko, T. S. Kim, M. Battaglia, T. Stöhlker, and W. P. Leemans. Low-Emittance Electron Bunches from a Laser-Plasma Accelerator Measured using Single-Shot X-Ray Spectroscopy. *Phys. Rev. Lett.*, 109:064802, Aug 2012. doi:10.1103/PhysRevLett.109.064802.

[28] J. Zhu, R. W. Assmann, M. Dohlus, U. Dorda, and B. Marchetti. Sub-fs electron bunch generation with sub-10-fs bunch arrival-time jitter via bunch slicing in a magnetic chicane. *Phys. Rev. Accel. Beams*, 19:054401, May 2016. doi:10.1103/PhysRevAccelBeams.19.054401.

[29] European XFEL. `https://www.xfel.eu/facility/comparison/index_eng.html`. Accessed: 2024-11-21.

[30] A. R. Maier, N. M. Delbos, T. Eichner, L. Hübner, S. Jalas, L. Jeppe, S. W. Jolly, M. Kirchen, V. Leroux, P. Messner, M. Schnepp, M. Trunk, P. A. Walker, C. Werle, and P. Winkler. Decoding Sources of Energy Variability in a Laser-Plasma Accelerator. *Phys. Rev. X*, 10:031039, Aug 2020. doi:10.1103/PhysRevX.10.031039.

[31] A. J. Gonsalves, K. Nakamura, C. Lin, D. Panasenko, S. Shiraishi, T. Sokollik, C. Benedetti, C. B. Schroeder, C. G. R. Geddes, J. van Tilborg, J. Osterhoff, E. Esarey, C. Toth, and W. P. Leemans. Tunable laser plasma accelerator based on longitudinal density tailoring. *Nature Physics*, 7(11):862–866, Nov. 2011. doi:10.1038/nphys2071.

[32] S. Jalas, M. Kirchen, C. Braun, T. Eichner, J. B. Gonzalez, L. Hübner, T. Hülsenbusch, P. Messner, G. Palmer, M. Schnepp, C. Werle, P. Winkler, W. P. Leemans, and A. R. Maier. Tuning curves for a laser-plasma accelerator. *Phys. Rev. Accel. Beams*, 26:071302, Jul 2023. doi:10.1103/PhysRevAccelBeams.26.071302.

[33] KALDERA project at DESY. `http://kaldera.desy.de`. Accessed: 2023-06-08.

[34] V. Leroux. *Wavefront degradation due to grating deformation.* PhD thesis, Universität Hamburg, 2018.

[35] N. Delbos, C. Werle, I. Dornmair, T. Eichner, L. Hübner, S. Jalas, S. Jolly, M. Kirchen, V. Leroux, P. Messner, M. Schnepp, M. Trunk, P. Walker, P. Winkler, and A. Maier. Lux – a laser–plasma driven undulator beamline. *Nuclear Instruments and Methods in Physics Research Section A: Accelerators, Spectrometers, Detectors and Associated Equipment*, 909:318–322, 2018. doi:https://doi.org/10.1016/j.nima.2018.01.082. 3rd European Advanced Accelerator Concepts workshop (EAAC2017).

[36] T. Eichner. *Improved Pulse Characteristics and PowerScaling of Drive Lasers for Laser-WakefieldAcceleration*. Phd thesis, 2023.

[37] T. Huelsenbusch. *Optimizing White-light Generation for an Optical Parametric Chirped Pulse Amplifier used as a Titanium-Sapphire Seed Laser*. Phd thesis, 2024.

[38] C. M. Werle, C. Braun, T. Eichner, T. Hülsenbusch, G. Palmer, and A. R. Maier. Out-of-plane multilayer-dielectric-grating compressor for ultrafast Ti:sapphire pulses. *Opt. Express*, 31(23):37437–37451, Nov 2023. doi:10.1364/OE.501093.

[39] T. Eichner and et al. A 700mJ Ti:Sapphire amplifier for laser plasma acceleration at 100Hz repetition rate. *TBD*, 2025. In preparation.

[40] C. Braun, C. M. Werle, G. Palmer, and A. R. Maier. Stretcher design for matching an out-of-plane MLD grating compressor, 2024.

[41] C. Braun, C. M. Werle, T. Eichner, G. Palmer, and A. R. Maier. Concepts for high average power Ti:Sa laser pulse compressors, 2023.

[42] C. Braun, C. M. Werle, T. Eichner, G. Palmer, and A. R. Maier. Concepts for high average power Ti:Sa laser pulse compressors, 2022.

[43] C. Braun, C. M. Werle, T. Eichner, G. Palmer, and A. R. Maier. Concepts for high average power Ti:Sa laser pulse compressors, 2022.

[44] Report of Workshop on Laser Technology for k-BELLA and Beyond. `https://www2.lbl.gov/LBL-Programs/atap/Report_Workshop_k-BELLA_laser_tech_final.pdf`. Accessed: 2024-12-13.

[45] M. Kirchen, S. Jalas, P. Messner, P. Winkler, T. Eichner, L. Hübner, T. Hülsenbusch, L. Jeppe, T. Parikh, M. Schnepp, and A. R. Maier. Optimal Beam Loading in a Laser-Plasma Accelerator. *Phys. Rev. Lett.*, 126:174801, Apr 2021. doi:10.1103/PhysRevLett.126.174801.

[46] M. Kirchen. *Novel Concepts for the Simulation and Experimental Demonstration of High-Quality Laser-Plasma Acceleration*. Phd thesis, 2021.

[47] W. Leemans, J. Daniels, A. Deshmukh, A. Gonsalves, A. Magana, H. Mao, D. Mittelberger, K. Nakamura, J. Riley, D. Syversrud, et al. Bella laser and operations. In *Proceedings of PAC*, pages 1097–1100, 2013.

[48] Y. Chu, Z. Gan, X. Liang, L. Yu, X. Lu, C. Wang, X. Wang, L. Xu, H. Lu, D. Yin, Y. Leng, R. Li, and Z. Xu. High-energy large-aperture Ti:sapphire amplifier for 5 PW laser pulses. *Opt. Lett.*, 40(21):5011–5014, Nov 2015. doi:10.1364/OL.40.005011.

[49] E. Sistrunk, T. Spinka, A. Bayramian, S. Betts, R. Bopp, S. Buck, K. Charron, J. Cupal, R. Deri, M. Drouin, A. Erlandson, E. S. Fulkerson, J. Horner, J. Horacek, J. Jarboe, K. Kasl, D. Kim, E. Koh, L. Koubikova, R. Lanning, W. Maranville, C. Marshall, D. Mason, J. Menapace, P. Miller, P. Mazurek, A. Naylon, J. Novak, D. Peceli, P. Rosso, K. Schaffers, D. Smith, J. Stanley, R. Steele, S. Telford, J. Thoma, D. VanBlarcom, J. Weiss, P. Wegner, B. Rus, and C. Haefner. All Diode-Pumped, High-repetition-rate Advanced Petawatt Laser System (HAPLS). In *Conference on Lasers and Electro-Optics*, page STh1L.2. Optica Publishing Group, 2017. doi:10.1364/CLEO_SI.2017.STh1L.2.

[50] Freie Universität Berlin. `https://refubium.fu-berlin.de/bitstream/handle/fub188/8219/09_Chapter05.pdf`. Accessed: 2024-11-19.

[51] A. E. Siegman. *Lasers*. University Science Books, 1986. ISBN 978-0-935702-11-8.

[52] T. J. Yu, S. K. Lee, J. H. Sung, J. W. Yoon, T. M. Jeong, and J. Lee. Generation of high-contrast, 30 fs, 1.5 PW laser pulses from chirped-pulse amplification Ti:sapphire laser. *Opt. Express*, 20(10):10807–10815, May 2012. doi:10.1364/OE.20.010807.

[53] Z. Cheng, F. Krausz, and C. Spielmann. Compression of 2 mj kilohertz laser pulses to 17.5 fs by pairing double-prism compressor analysis and performance. *Optics Communications*, 201(1):145–155, 2002. doi:https://doi.org/10.1016/S0030-4018(01)01675-3.

[54] P. Dombi, V. S. Yakovlev, K. O'Keeffe, T. Fuji, M. Lezius, and G. Tempea. Pulse compression with time-domain optimized chirped mirrors. *Opt. Express*, 13(26):10888–10894, Dec 2005. doi:10.1364/OPEX.13.010888.

[55] V. Ivanov. Compact optical grating compressor. *Opt. Express*, 30(20):35338–35347, Sep 2022. doi:10.1364/OE.468814.

[56] A. E. Siegman. *Lasers*. University Science Books, 1986. ISBN 978-0-935702-11-8.

[57] E. Treacy. Optical pulse compression with diffraction gratings. *IEEE Journal of Quantum Electronics*, 5(9):454–458, 1969. doi:10.1109/JQE.1969.1076303.

[58] Plymouth grating laboratory. `https://www.plymouthgrating.com/guidance/technical-notes/fundamentals/the-grating-equation/`, . Accessed: 2024-12-20.

[59] LightConversion. `https://toolbox.lightcon.com/tools/gratingpair`. Accessed: 2024-12-20.

[60] A. Öffner. US patent: Unit power imaging catoptric anastigmat. Patent Number 3,748,015, July 24,1973.

[61] L. Ranc, C. L. Blanc, N. Lebas, L. Martin, J.-P. Zou, F. Mathieu, C. Radier, S. Ricaud, F. Druon, and D. Papadopoulos. Improvement in the temporal contrast in the tens of ps range of the multi-pw apollon laser front-end. *Opt. Lett.*, 45(16):4599–4602, Aug 2020. doi:10.1364/OL.401272.

[62] P. Moulton. Ti-doped sapphire: tunable solid-state laser. *Optics News*, 8(6):9–9, Nov 1982. doi:10.1364/ON.8.6.000009.

[63] F. X. K. (Ed.). *Few-Cycle Laser Pulse Generation and Its Applications*. Springer, 1. Auflage 2004. ISBN 3-540-20115-7.

[64] A. Jullien, O. Albert, F. Burgy, G. Hamoniaux, J.-P. Rousseau, J.-P. Chambaret, F. Augé-Rochereau, G. Chériaux, J. Etchepare, N. Minkovski, and S. M. Saltiel. 10^{10} temporal contrast for femtosecond ultraintense lasers by cross-polarized wave generation. *Opt. Lett.*, 30(8):920–922, Apr 2005. doi:10.1364/OL.30.000920.

[65] J. Jiang, Z. Zhang, and T. Hasama. Evaluation of chirped-pulse-amplification systems with Offner triplet telescope stretchers. *J. Opt. Soc. Am. B*, 19(4): 678–683, Apr 2002. doi:10.1364/JOSAB.19.000678.

[66] G. Pretzler, A. Kasper, and K. Witte. Angular chirp and tilted light pulses in CPA lasers. *Applied Physics B: Lasers and Optics*, 70(1):1–9, 2000. doi:10.1007/s003400050001.

[67] M. Thévenet, D. E. Mittelberger, K. Nakamura, R. Lehe, C. B. Schroeder, J.-L. Vay, E. Esarey, and W. P. Leemans. Pulse front tilt steering in laser plasma accelerators. *Phys. Rev. Accel. Beams*, 22:071301, Jul 2019. doi:10.1103/PhysRevAccelBeams.22.071301.

[68] A. Popp, J. Vieira, J. Osterhoff, Z. Major, R. Hörlein, M. Fuchs, R. Weingartner, T. P. Rowlands-Rees, M. Marti, R. A. Fonseca, S. F. Martins, L. O. Silva, S. M. Hooker, F. Krausz, F. Grüner, and S. Karsch. All-Optical Steering of Laser-Wakefield-Accelerated Electron Beams. *Phys. Rev. Lett.*, 105:215001, Nov 2010. doi:10.1103/PhysRevLett.105.215001.

[69] A. Börzsönyi, L. Mangin-Thro, G. Cheriaux, and K. Osvay. Two-dimensional single-shot measurement of angular dispersion for compressor alignment. *Optics Letters*, 38(4):410, 2013. doi:10.1364/OL.38.000410.

[70] R. Bödefeld, M. Hornung, J. Hein, and M. C. Kaluza. High precision elimination of angular chirp in CPA laser systems with large stretching factors or high bandwidth. *Applied Physics B*, 115(3):419–426, 2014. doi:10.1007/s00340-013-5622-z.

[71] Compressor alignment methods, 2018.

[72] A. E. Siegman. Defining, measuring, and optimizing laser beam quality. In A. Bhowmik, editor, *Laser Resonators and Coherent Optics: Modeling, Technology, and Applications*, volume 1868, pages 2 – 12. International Society for Optics and Photonics, SPIE, 1993. doi:10.1117/12.150601.

[73] T. Erdogan. Gratings for High-average-power Ti:Sapphire Laser Systems. Technical report, Plymouth Grating Laboratory, 2018.

[74] O. Loebich. The optical properties of gold. *Gold Bulletin*, 5:2–10, 1972. doi:https://doi.org/10.1007/BF03215148.

[75] FASTLITE. Homepage of fastlite-wizzler. `http://www.fastlite.com/en/ar824651-823532-Wizzler.html?Cookie=set`.

[76] S. Fourmaux, C. Serbanescu, L. Lecherbourg, S. Payeur, F. Martin, and J. C. Kieffer. Investigation of the thermally induced laser beam distortion associated with vacuum compressor gratings in high energy and high average power femtosecond laser systems. *Opt. Express*, 17(1):178–184, Jan 2009. doi:10.1364/OE.17.000178.

[77] V. Leroux, S. W. Jolly, M. Schnepp, T. Eichner, S. Jalas, M. Kirchen, P. Messner, C. Werle, P. Winkler, and A. R. Maier. Wavefront degradation of a 200 TW laser from heat-induced deformation of in-vacuum compressor gratings. *Opt. Express*, 26(10):13061–13071, May 2018. doi:10.1364/OE.26.013061.

[78] J. Qiao, J. Papa, and X. Liu. Spatio-temporal modeling and optimization of a deformable-grating compressor for short high-energy laser pulses. *Opt. Express*, 23(20):25923–25934, Oct 2015. doi:10.1364/OE.23.025923.

[79] V. Leroux, T. Eichner, and A. Maier. Description of spatio-temporal couplings from heat-induced compressor grating deformation. *Opt. Express*, 28:8257–8265, 2020. doi:https://doi.org/10.1364/oe.386112.

[80] E. P. Power, S. Bucht, K. R. P. Kafka, J. Bromage, and J. D. Zuegel. Design and characterization of “flow-cell” integrated-flow active cooling for high-average-power ceramic optics. *Opt. Express*, 30:42525, 2022. doi:https://doi.org/10.1364/OE.473479.

[81] D. A. Alessi, P. A. Rosso, H. T. Nguyen, M. D. Aasen, J. A. Britten, and C. Haefner. Active cooling of pulse compression diffraction gratings for high energy, high average power ultrafast lasers. *Opt. Express*, 24(26):30015–30023, Dec 2016. doi:10.1364/OE.24.030015.

[82] Plymouth grating laboratory. `https://www.plymouthgrating.com/product/gold-diffraction-gratings/`, . Accessed: 2024-11-24.

[83] Plymouth grating laboratory. `https://www.plymouthgrating.com/product/multilayer-dielectric-mld-diffraction-gratings/`, . Accessed: 2024-11-24.

[84] M. D. Perry, R. D. Boyd, J. A. Britten, D. Decker, B. W. Shore, C. Shannon, and E. Shults. High-efficiency multilayer dielectric diffraction gratings. *Opt. Lett.*, 20(8):940–942, Apr 1995. doi:10.1364/OL.20.000940.

[85] T. Erdogan. PGL Technical Note – Gratings for High-average-power Ti:Sapphire Laser Systems. Technical report, Plymouth Grating Laboratory, .

[86] D. Alessi, H. Nguyen, J. Britten, P. Rosso, and C. Haefner. Low-dispersion low-loss dielectric gratings for efficient ultrafast laser pulse compression at high average powers. *Optics & Laser Technology*, 117:239–243, 2019. doi:https://doi.org/10.1016/j.optlastec.2019.04.005.

[87] T. Erdogan. PGL Technical Note – The Grating Equation. Technical report, Plymouth Grating Laboratory, .

[88] T. Erdogan. Advantages of Out-of-plane Pulse Compression Gratings and How to Choose the Right Polarization. Technical report, Plymouth Grating Laboratory, 2022.

[89] T. Erdogan. PGL Technical Note – Dispersion and Pulses. Technical report, Plymouth Grating Laboratory, .

[90] M. N. Polyanskiy. Refractive index database of optical constants. `https://refractiveindex.info`. Accessed on 2024-04-17.

[91] P. Tournois. Acousto-optic programmable dispersive filter for adaptive compensation of group delay time dispersion in laser systems. *Optics Communications*, 140(4-6):245–249, 1997. doi:10.1016/S0030-4018(97)00153-3.

[92] D. L. Smith, S. L. Erdogan, and T. Erdogan. Advantages of out-of-plane pulse compression gratings. *Appl. Opt.*, 62(13):3357–3369, May 2023. doi:10.1364/AO.485637.

[93] J. Bromage, C. Dorrer, and R. K. Jungquist. Temporal contrast degradation at the focus of ultrafast pulses from high-frequency spectral phase modulation. *J. Opt. Soc. Am. B*, 29(5):1125–1135, May 2012. doi:10.1364/JOSAB.29.001125.

[94] A. Giulietti, P. Tomassini, M. Galimberti, D. Giulietti, L. A. Gizzi, P. Koester, L. Labate, T. Ceccotti, P. D'Oliveira, T. Auguste, P. Monot, and P. Martin. Prepulse effect on intense femtosecond laser pulse propagation in gas. *Physics of Plasmas*, 13(9):093103, sep 2006. doi:10.1063/1.2351961.

[95] K. Nakamura, H.-S. Mao, A. J. Gonsalves, H. Vincenti, D. E. Mittelberger, J. Daniels, A. Magana, C. Toth, and W. P. Leemans. Diagnostics, Control and Performance Parameters for the BELLA High Repetition Rate Petawatt Class Laser. *IEEE Journal of Quantum Electronics*, 53(4):1–21, 2017. doi:10.1109/JQE.2017.2708601.

[96] B. Webb, C. Dorrer, S.-W. Bahk, C. Jeon, R. G. Roides, and J. Bromage. Temporal contrast degradation from mid-spatial-frequency surface error on stretcher mirrors. *Appl. Opt.*, 63(17):4615–4621, Jun 2024. doi:10.1364/AO.522892.

[97] P. F. Moulton. Spectroscopic and laser characteristics of Ti:Al2O3. *J. Opt. Soc. Am. B*, 3(1):125–133, Jan 1986. doi:10.1364/JOSAB.3.000125.

[98] Coherent. Coherent homepage. `https://www.coherent.com/de/lasers/amplifiers/revolution`. Accessed on 2024-07-31.

[99] F. Estable, F. Salin, M. Allain, P. Georges, and A. Brun. Direct measurement of saturation fluence in Ti:Al2O3. *Optics Communications*, 72(3):235–238, 1989. doi:https://doi.org/10.1016/0030-4018(89)90402-1.

[100] S. Tokita, M. Hashida, S. Masuno, S. Namba, and S. Sakabe. 0.3% energy stability, 100-millijoule-class, ti:sapphire chirped-pulse eight-pass amplification system. *Opt. Express*, 16(19):14875–14881, Sep 2008. doi:10.1364/OE.16.014875.

[101] V. V. Ivanov, A. Maksimchuk, and G. Mourou. Amplified spontaneous emission in a Ti:sapphire regenerative amplifier. *Appl. Opt.*, 42(36):7231–7234, Dec 2003. doi:10.1364/AO.42.007231.

[102] V. Miller and K. Žídek. High-precision FoM measurement setup for Ti:sapphire crystals. *Appl. Opt.*, 62(5):1345–1350, Feb 2023. doi:10.1364/AO.479254.

[103] H. G. Pfeiffer and H. A. Liebhafsky. The origins of beer's law. *Journal of Chemical Education*, 28(3):123, 1951. doi:10.1021/ed028p123.

[104] K. Ertel, C. Hooker, S. Hawkes, B. Parry, and J. Collier. ASE suppression in a high energy titanium sapphire amplifier. *Optics express*, 16:8039–49, 06 2008. doi:10.1364/OE.16.008039.

[105] R. Paschotta. Thermal lensing. `https://www.rp-photonics.com/thermal_lensing.html`. Accessed on 2024-11-29.

[106] S. Cho, J. Jeong, S. Hwang, and T. J. Yu. Thermal lens effect model of Ti:sapphire for use in high-power laser amplifiers. *Applied Physics Express*, 11 (9):092701, aug 2018. doi:10.7567/APEX.11.092701.

[107] H. Eilers, E. Strauss, and W. M. Yen. Photoelastic effect in ti^{3+}-doped sapphire. *Phys. Rev. B*, 45:9604–9610, May 1992. doi:10.1103/PhysRevB.45.9604.

[108] T. A. Planchon, W. Amir, C. Childress, J. A. Squier, and C. G. Durfee. Measurement of pump-induced transient lensing in a cryogenically-cooled high average power ti:sapphire amplifier. *Opt. Express*, 16(23):18557–18564, Nov 2008. doi:10.1364/OE.16.018557.

[109] P. Popov, V. Solomennik, P. Belyaev, L. Lytvynov, and V. Puzikov. Thermal conductivity of pure and Cr^{3+} and Ti^{3+} doped Al_2O_3 crystals in 50-300 k temperature range. *Functional materials*, 2011.

[110] A. Defranzo and B. G. Pazol. Index of refraction measurement on sapphire at low temperatures and visible wavelengths. *Applied optics*, 32 13:2224–34, 1993.

[111] S. Ito, H. Nagaoka, T. Miura, K. Kobayashi, A. Endo, and K. Torizuka. Measurement of thermal lensing in a power amplifier of a terawatt Ti:sapphire laser. *Applied Physics B*, 74(4):343–347, Apr. 2002. doi:10.1007/s003400200812.

[112] S. Chenais, F. Balembois, F. Druon, G. Lucas-Leclin, and P. Georges. Thermal lensing in diode-pumped ytterbium lasers-part i: theoretical analysis and wavefront measurements. *IEEE Journal of Quantum Electronics*, 40(9):1217–1234, 2004. doi:10.1109/JQE.2004.833198.

[113] OXALIS. Homepage of oxalis. `https://www.oxalis-laser.com/commodpro.php`. Accessed on 2024-11-27.

[114] Eksma Optics. `https://eksmaoptics.com/out/media/EKSMA_Optics_TiSapphire_Crystal.pdf`. Accessed: 2024-12-11.

[115] A. E. Siegman. *Lasers*. University Science Books, 1986. ISBN 978-0-935702-11-8.

[116] T. Eichner, T. Hülsenbusch, J. Dirkwinkel, T. Lang, L. Winkelmann, G. Palmer, and A. R. Maier. Spatio-spectral couplings in saturated collinear opcpa. *Opt. Express*, 30(3):3404–3415, Jan 2022. doi:10.1364/OE.448551.

[117] T. Messtechnik. Homepage of tem messtechnik. `'https://tem-messtechnik.de/produkte/strahlstabilisierung-mit-aligna/#1654698555235-4a487cd5-5de9'`. Accessed on 2024-12-03.

[118] Thorlabs. Homepage of thorlabs. `https://www.thorlabs.com/newgrouppage9.cfm?objectgroup_id=5035`. Accessed on 2024-12-03.

[119] S. Backus, J. Peatross, C. P. Huang, M. M. Murnane, and H. C. Kapteyn. Ti:sapphire amplifier producing millijoule-level, 21-fs pulses at 1 khz. *Opt. Lett.*, 20(19):2000–2002, Oct 1995. doi:10.1364/OL.20.002000.

8 Acknowledgements

The completion of this thesis has challenged me in many ways and I had the luxury of receiving support from various people, who I would like to acknowledge here and express my gratitude.

First of all Andi — thank you for welcoming me in your group. Thank you for being my supervisor and for providing a great vision to follow. You gave me the opportunity to work on an exciting project as part of an amazing team. I feel honored, that I could contribute to the exciting development of plasma acceleration at DESY.

A big thank you goes to Guido for supporting me throughout my entire thesis. You always had time for me and the patience to discuss all matters, big and small. Thank you for encouraging me to make my own plans and to develop my own judgment.

I would like to thank Professor Kärtner for supervising my thesis, and Professors Pfannkuche, Professor Potthoff, and Professor Leemans for joining my disputation committee.

I have the great pleasure of working in an amazing team. The LUX team is full of bright and kind people, who are always happy to help, explain, and show new things — and have fun along the way. You all greatly supported me and believed in me, sometimes more than I believed in myself. A few people I would like to thank especially as I had the pleasure to work particularly close with them: Chris, thank you for your patience, for teaching me the importance of the detail and for always being willing to take a closer look. Thank you for letting me profit from your experience, knowledge and remarkable memory.
Juan, thank you for your energy and enthusiasm. You have a willingness to do everything that is necessary and you supported me at all times. Thank you for letting me to "be your boss" sometimes.
Kaja, thank you for your friendship. Talking to you always makes me feel understood. I am incredibly glad you joined the team — having you around made me braver in many situations.
Thomas, Timo, Matthias, Caterina, JJ and Lutz — thank you for teaching me how to get things done in a laser lab. Thank you for your care, patience and the willingness to share your knowledge with me.
Paul and Max — thank you for being great colleagues from day one. And to Frida, Leonie, Sam, Anneli, Anna, Tatiana, Abdullah, Luisa, Fabian, Lisa, Parsa and Nadia — thank you for joining our team and enriching the work atmosphere with your new

perspectives, kindness and, of course, delicious tea and snacks.
I would also like to thank everyone from the MPL team. I found the merging of the plasma groups to be very enriching, both, socially and intellectually.

I would also like to thank the lovely people of the Optica Student Chapter, among others Agata, Benoit, Rene, Josina, Nayla, Tobi and Supriya. With you I learned that it is possible to organize great events when you are determined and have the right people around. The chapter added an extra portion off responsibility but also an extra portion of fun, and made me feel capable beyond academic work.

Last but not least, I want to thank my family and my friends Katharina, Ivonne and Cedric: For believing in me, supporting me all the way and being my fan club, whenever I needed to be cheered on. And Robin — thank you for your kindness and love. You comforted me whenever I needed it and celebrated every small and big success with me. You listened to me everyday and always had my back, and constantly motivated me to give my best.